Functional Impairment Following Axonal Injury

by

Ehsan Daneshi

M.Sc., University of Sheffield, 2010
B.Sc., Amirkabir University of Technology, 2009

Thesis Submitted in Partial Fulfillment of the
Requirements for the Degree of
Doctor of Philosophy

in the
School of Mechatronic Systems Engineering
Faculty of Applied Sciences

SIMON FRASER UNIVERSITY
Spring 2021

Declaration of Committee

Name: **Ehsan Daneshi**

Degree: **Doctor of Philosophy**

Thesis title: **Functional Impairment Following Axonal Injury**

Committee:

Chair: Helen Bailey
Lecturer, Mechatronic Systems Engineering

Carolyn Sparrey
Supervisor
Associate Professor, Mechatronic Systems Engineering

G R Wayne Moore
Committee Member
Professor, Pathology and Laboratory Medicine
The University of British Columbia

Edward Park
Committee Member
Professor, Mechatronic Systems Engineering

Teresa Cheung
Examiner
Assistant Professor, Engineering Science

Roger Tam
External Examiner
Associate Professor, Biomedical Engineering
The University of British Columbia

Ethics Statement

The author, whose name appears on the title page of this work, has obtained, for the research described in this work, either:

a. human research ethics approval from the Simon Fraser University Office of Research Ethics

or

b. advance approval of the animal care protocol from the University Animal Care Committee of Simon Fraser University

or has conducted the research

c. as a co-investigator, collaborator, or research assistant in a research project approved in advance.

A copy of the approval letter has been filed with the Theses Office of the University Library at the time of submission of this thesis or project.

The original application for approval and letter of approval are filed with the relevant offices. Inquiries may be directed to those authorities.

Simon Fraser University Library
Burnaby, British Columbia, Canada

Update Spring 2016

Abstract

Following trauma or other neurological disorders, a series of events happen that cause axonal dysfunction or ultimately lead to axonal death. Computational modeling of the nervous system facilitates systematic study of the effects of each injury parameter on the output. The overall goal of this research was to develop a new method of simulating axon damage in a biophysical model and quantify the effects of structural damage on signal conduction. To achieve this, three objectives were addressed 1) quantify the effects of normal morphological variation and demyelination on axonal conduction characteristics, 2) develop a new computationally efficient method for modeling damage in axons, and 3) characterize the structure changes observed in human axons and quantify the relationship between these observed changes and axonal function. Biophysical computational models developed in NEURON were employed to characterize morphological changes in damaged axons and study the effects of some of the most common axonal injuries such as myelin damage and spheroid formation on signal propagation in axons with different calibers. To facilitate efficient computational simulation, a new approach for increasing geometrical resolution in NEURON was developed and assessed. To investigate the effects of axonal swelling on action potential conduction in myelinated axons, the morphological properties of axonal spheroids were characterized by analyzing a series of confocal images captured from post-mortem human brain samples of patients with MS and infarction. Our results indicate that subtle abnormalities in nodal, paranodal and juxtaparanodal regions may have sizable effects on action potential amplitude and velocity and more targeted treatments need to be developed that focus on these regions. In addition, the results of our histopathological and computational studies suggest that axons with different diameters may respond differently to injuries and diseases. Therefore, it is important to perform experimental injury models across a wide range of axons to get a more comprehensive understanding of the relationship between axonal morphological features, injury parameters and functional responses. We expect this research to lay the quantitative foundation for finding new potential functional markers of white matter tissue damage and provide further insights into how myelin damage and axonal spheroids may affect function.

Keywords: Computational Model; Axon; Traumatic Brain Injury; Spinal Cord Injury; Multiple Sclerosis

Dedication

To my dearest mom and dad, who inspired me by their great passion for science.
To my mother- and father-in-law for their continued support and encouragement.
To my best friend and dear wife, Ghazal, for her great love and patience.
To Eli, the most wonderful little sister in the world.
To my grandparents.

Acknowledgements

I would like to thank my supervisor, Dr. Carolyn Sparrey for giving me the opportunity to join her lab and improve my research skills. Her support and guidance was invaluable to me. Thank you for teaching me how to think critically, Carolyn! It changed my life for ever.

I also would like to thank my co-supervisors, Dr. G R Wayne Moore and Dr. Edward Park, for supporting me through my PhD journey and providing me with great insight.

Going through PhD is an exciting intellectual practice. However, as Isaac Newton said: "If I have seen further it is by standing on the shoulders of Giants". I would like to thank all researcher and people who paved the way for the new generation of students and researchers to have the opportunity to work on new interesting research questions and have the pleasure of finding things out.

Table of Contents

List of Tables

List of Figures

Chapter 1

Background and Motivation

1.1 Motivation

Neurological disorders, such as traumatic brain injury (TBI), spinal cord injury (SCI), multiple sclerosis (MS), and stroke, are considered the main causes of disability and the second leading cause of death worldwide [4]. Compared to 1990, due to population increase and aging, there has been a 39% increase in neurologically related death incidents [4]. Although extensive research has been conducted to study neurological diseases, still no effective treatment or cure has been found for most.

The methods currently used for studying neurological injuries are limited. Performing human studies to develop and test new treatments is challenging and even not possible in some cases. Hence, animal studies and in vitro experiments are currently the main instruments used by researchers to discover new treatments and assess the safety of tested drugs before conducting human studies. Although various similarities exist between humans and animals, their anatomy and electrophysiology are different. Neurons are the main cells in the nervous system responsible for driving the generation and propagation of electrical signals necessary for proper motor and sensory function. Not only are the neurons of animals different from those of humans, but also a normal range of variations exist in the morphological and electrophysiological properties of neurons in animal and human nervous systems. Hence, it is important to study the mechanisms underlying injury to find effective treatments for neurological disorders. Usually following trauma or other neurological disorders, a series of events cause neurological dysfunction or ultimately lead to neuronal death. Although these events are related, the scale of their functional effects may be very different. Therefore, it is essential to assess each injury independently to study its underlying mechanisms and investigate its effects on signal propagation. However, it is extremely challenging, if not impossible, to study different injuries independently in animal models and, to some extent, in in vitro studies. Besides, some diseases, such as MS, have only been observed in humans, making studying such diseases in animals challenging. As a result, many treatments that showed promise in the laboratory have not worked in humans.

Performing animal studies is costly, time-consuming, and ethically challenging. Recently, there has been an increasing focus on reducing the number of animals used in research studies and using animal models only when no other suitable alternatives are available. Therefore, it is essential to improve the study methods and use less invasive techniques to reduce pain and the overall number of animals used in experiments. Although complementary data analysis techniques help use collected data more effectively and answer research questions, translating animal studies into humans has been very challenging.

Computational modeling of the nervous system is an attractive alternative to overcome these limitations. In recent years, there has been an increasing interest among the neuroscience community in employing biophysical models because they allow changing and studying the effects of each injury parameter on the output individually. In addition, such models are much cheaper and faster than animal studies. Computational models help us narrow down the parameter space and only test parameters with the best promise and minimize the number of animals used in those studies. In this thesis, we employed a series of computational models to investigate the relationship between different neuropathologies and dysfunction reported in human patients and animal models of TBI, SCI, and MS.

1.2 Anatomy and Electrophysiology of the Nervous System

Generally, the nervous system is responsible for coordinating voluntary and involuntary actions and transmitting signals between the brain and other parts of the body. This system consists of two main sections: the central nervous system (CNS) and the peripheral nervous system (PNS) [5] (see Figure 1.1). The CNS includes two main components: the brain and the spinal cord. On the other hand, the PNS comprises all the other nerves in the human body, such as the nerves that innervate upper and lower extremity muscles. Generally, the human brain and spinal cord are protected by the skull, vertebral column, and back muscles.

1.2.1 The Brain

Intelligence, creativity, emotions, speech, and memory are some of the functions and abilities created and controlled by the human brain. The brain often receives information through five senses: vision, smell, hearing, touch, and taste. An adult human brain consists of about 86 billion neurons and may weigh up to 1.5 kg [6]. The human brain is made up of the cerebrum, cerebellum, and brainstem, which are protected by the skull bone (Figure 1.2). Generally, the CNS is divided into two constituent materials: white matter and gray matter (Figure 1.3). The gray matter is made up of neuronal bodies, whereas the white matter mostly consists of myelinated axons. Both the brain and the spinal cord are surrounded by cerebrospinal fluid (CSF) that helps protect them from damage. This CSF also plays an important role in clearing the waste resulting from neuronal activities [7, 8] and proteins linked to neurodegenerative diseases, such as β-amyloid ($A\beta$) [8–10].

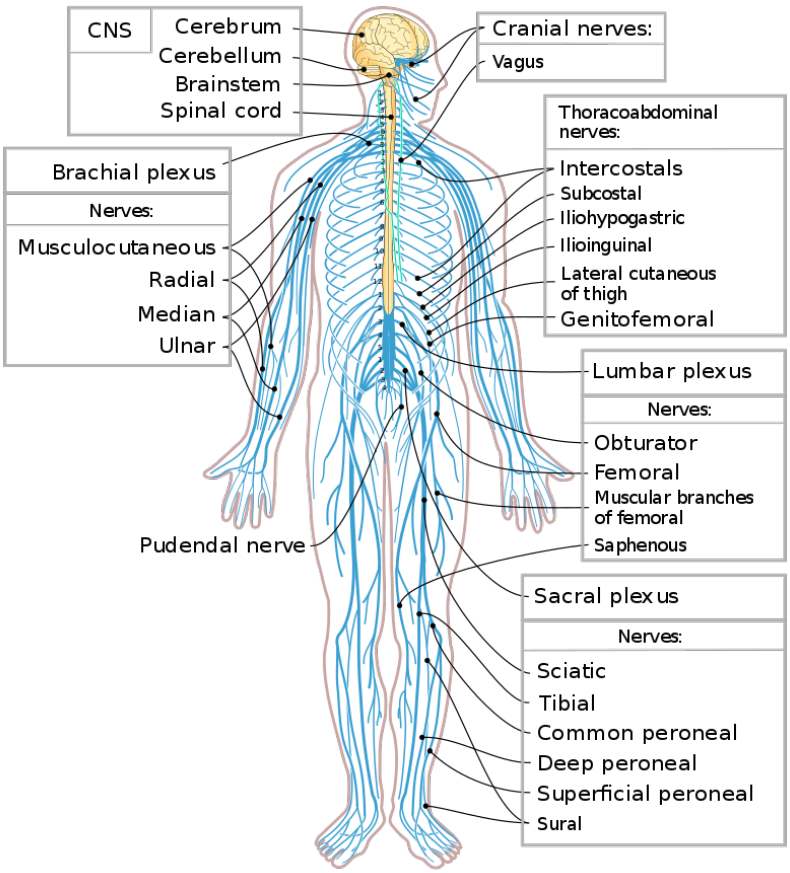

Figure 1.1: Together, the central nervous system (CNS) and peripheral nervous system (PNS) form the nervous system. The CNS comprises the brain and spinal cord. The PNS sends electrical impulses to and from the spinal cord to other organs in the body. Adapted from Wikipedia, User:Medium69, User:Jmarchn, (https://commons.wikimedia.org/wiki/File:nervous_system_diagram-en.svg). This figure is licensed under CC BY-SA 4.0 (https://creativecommons.org/licenses/by-sa/4.0/legalcode).

The cerebrum is the largest part of the brain, consisting of left and right hemispheres [11]. These two hemispheres are connected and communicate with each other through the corpus callosum. The corpus callosum contains about 200 million axons [12], which are known as commissural fibers or transverse fibers. The left hemisphere primarily controls the right side of the body, whereas the right hemisphere primarily controls the left side. The outer surface of the cerebrum is called the cerebral cortex, which contains about 16 billion neurons [6]. This cerebral cortex is responsible for tactile processing, vision, hearing, speech, reasoning, emotions, learning, and movement control, among others. The somatosensory cortex is part of the cortex located in the middle of the brain and is responsible for receiving input from different parts of the body.

The cerebellum, which stands for "little brain", is located at the back of the brain below the cerebrum (See Figure 1.2). Similar to the cerebrum, the cerebellum consists

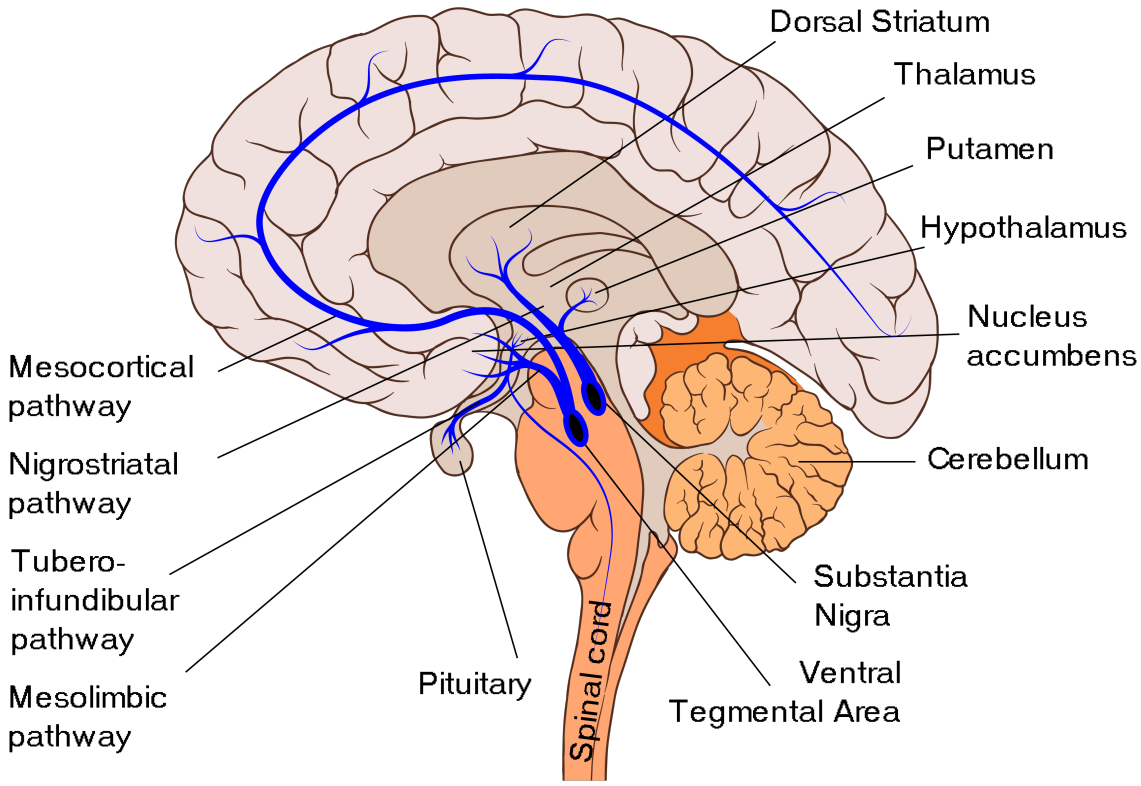

Figure 1.2: Anatomical position of different parts of the brain. Adapted from Wikimedia, User:Slashme; Patrick J. Lynch; User:Fvasconcellos (https://commons.wikimedia.org/wiki/File:Dopaminergic_pathways.svg). This figure is licensed under CC BY-SA 4.0 (https://creativecommons.org/licenses/by-sa/4.0/legalcode).

of gray matter and white matter, which form the two hemispheres. The gray matter on the surface forms the cerebellar cortex, with the white matter directly underneath. The cerebellum mainly serves to coordinate muscle movements, maintain body balance [13], receive proprioceptive information, and control ocular reflexes, including fixation on a target [14, 15]. Damage to the cerebellum may result in a broad range of abnormalities, such as loss of balance, abnormal gait, and nystagmus, as well as movement planning and motor learning problems [15, 16].

The human brainstem consists of three sections: midbrain, pons, and medulla oblongata. This structure is located in the brain's most rostral part at the juncture of the cerebrum and spinal column. Many of the vital functions, such as breathing [17], swallowing [18], and arousal [19], as well as vasomotor functions (controlling the constriction or dilatation of blood vessels), are monitored and controlled by the brainstem. Efferent and afferent axons travel through the brainstem and decussate (cross) to connect the spinal cord to the cerebrum [20]. The medulla oblongata is seated above the spinal cord and has many connections with it. This structure is involved in many unconscious functions, such as breathing, heart rate and body temperature regulation, waking and sleeping, digestion, sneezing, coughing,

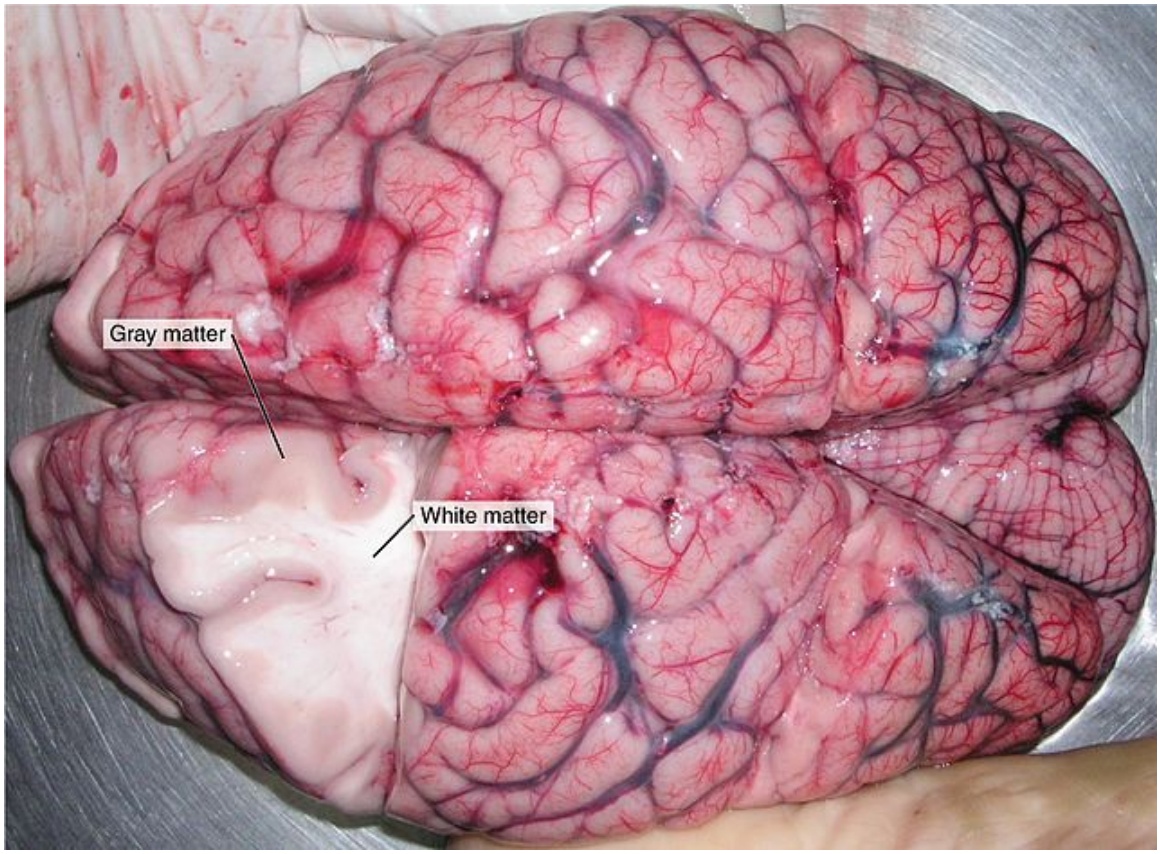

Figure 1.3: The gray matter in the brain's cortex area consists of cell bodies and surrounds the white matter tissue that is mostly myelinated axons propagating electric impulses to and from different neurons. Adapted from Wikimedia, OpenStax (https://commons.wikimedia.org/wiki/File:1202_White_and_Gray_Matter.jpg). This figure is licensed under CC BY-SA 4.0 (https://creativecommons.org/licenses/by/4.0/legalcode).

vomiting, and swallowing. In addition, the brainstem connects the cerebellum's axons to the motor sections of the cerebral cortex, which allows for fine control of the motor movements needed for daily activities.

1.2.2 Spinal Cord

The spinal cord, which has the diameter of a human finger (10 mm), is composed of millions of tightly packed neural cells running through a spinal canal. Neurons, glia, and blood vessels are the three key elements forming the spinal cord's cylindrical structure. The spinal cord is the main communication pathway that transmits sensory (including touch, pain, and heat) and motor information between the human brain and limbs, trunk, and other internal organs [5, 21] (Fig. 1.1). Neuronal cell bodies (soma) are located in an H-shaped region at the center of the spinal cord's column, in the gray matter (Fig. 1.4). The gray matter contains lower motor neurons projecting long axons to the muscles, internal organs, and skin over the whole body. These neurons act as an intermediate circuitry between the brain

and body organs, allowing the brain to move or control muscles by sending electrochemical signals. The spinal cord's outer cylindrical area is white in color, which is mostly the result of myelinated axons. These axons are bundled into specialized tracts and conduct modulated messages from ganglion cells. Axons conduct both ascending and descending signals to facilitate movement and provide sensation. Different levels of injury to the spinal cord may affect different functions.

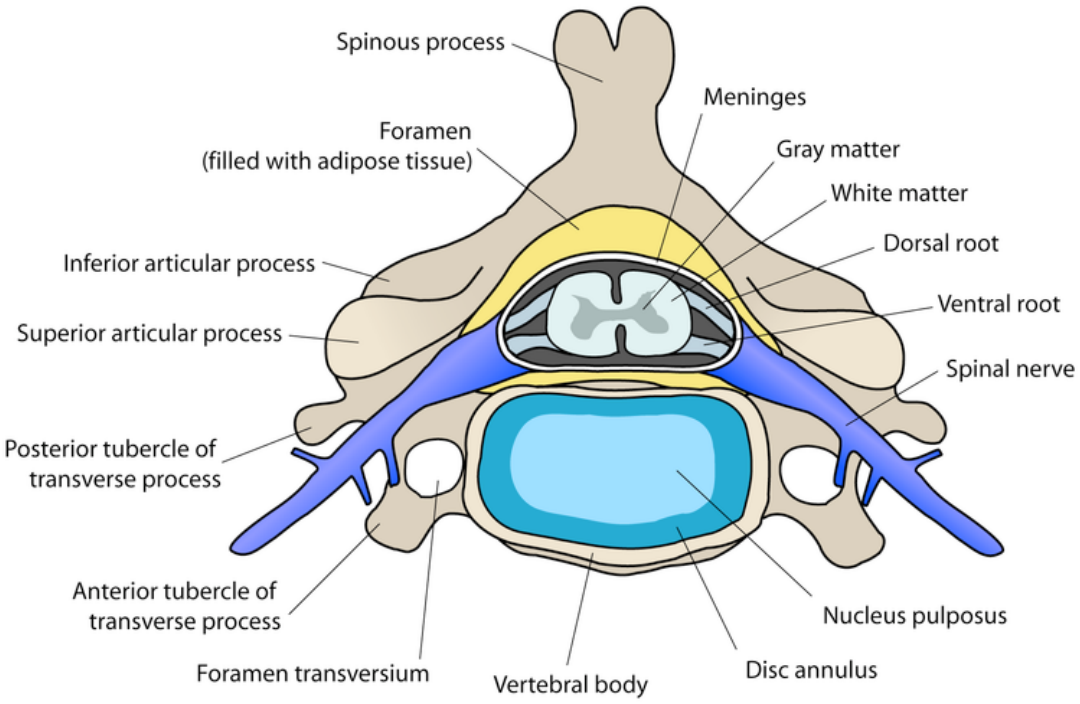

Figure 1.4: Cross section of the spinal cord. The spinal cord is composed of white matter and gray matter tissue. The delicate structure of the spinal cord is covered by three layers of meninges and protected by bones, discs, and ligaments along the vertebrae. Adapted from Wikipedia, user:debivort (https://commons.wikimedia.org/wiki/File:Cervical_vertebra_english.png). This figure is licensed under CC BY-SA 3.0 (https://creativecommons.org/licenses/by-sa/3.0/legalcode).

Similar to the human brain, the spinal cord is covered by three nested protective layers, which are called meninges [22].The outer layer, which plays a key role in protecting the spine's soft tissue, is the dura mater; the middle layer is called the arachnoid; and the innermost soft layer is called the pia mater. Thirty-three bone rings, called vertebrae, make a cylindrical structure that covers and protects the spinal cord's very soft and delicate tissue. These circular-shaped bones are located on top of each other and attached by ligaments on both sides of the spine. The spinal column bones are named as follows:

- Seven cervical vertebrae (C1-C7) in the neck
- Twelve thoracic vertebrae (T1-T12) attach to the ribs
- Five lumbar vertebrae (L1-L5) are in the lower back;
- Five sacral vertebrae (S1-S5) that connect to the pelvis

These bones are separated from each other by a spongy material called an intervertebral disc. Although the presence of these discs between the vertebral bones is necessary, they make the spinal cord very vulnerable to injury. Notably, the spinal cord and muscles are linked together by 31 pairs of spinal nerves that exit from the spinal cord through small openings in the vertebral column. These nerves are, in fact, bundles of axons originating from lower motor neurons and sensory and autonomic axons. Spinal nerves come out through holes called the foramen. The location of these nerves along the spinal cord determines their function. These nerves are numbered in a similar way to the vertebrae.

- Cervical spinal nerves (C1-C8) emerge from the spinal cord in the neck region and control signals to the back of the head, neck, and shoulders; arms and hands; and the diaphragm.
- Thoracic spinal nerves (T1-T12) emerge from the spinal cord in the upper mid-back region and control signals to the chest muscles, some back muscles, and many organ systems, including parts of the abdomen.
- Lumbar spinal nerves (L1-L5) emerge from the spinal cord in the low back region and control signals to the lower parts of the abdomen and the back, the buttocks, some parts of the external genital organs, and parts of the leg.
- Sacral spinal nerves (S1-S5) emerge from the spinal cord in the low back region and control signals to the thighs and lower parts of the legs, the feet, most of the external genital organs, and the area around the anus.

Spinal nerves usually exit from vertebrae of the same number, with the exception of the spinal nerves in the cervical segment, which exit above the corresponding vertebrae.

1.2.3 Neurons

The CNS mainly consists of neurons and glial cells [5]. Neurons send electrical impulses rapidly to other cells by releasing chemicals known as neurotransmitters [23, 24]. On the other hand, the glial cells provide critical support to the nervous system, including creating myelin for neurons. In general, neurons consist of four main parts: a soma, an axon, dendrites, and synapses (see figure 1.5). Most of the neurons' metabolic activity occurs in the cell body, which is called the soma or neuronal perikaryon. This soma supports the neuron's

proper functioning and contains many organelles as well as the cell nucleus. Messenger RNA (mRNA), a single-stranded RNA molecule necessary for producing proteins in neurons, is produced by the cell nucleus. Another important organelle present inside the soma is the mitochondria, which are the site of energy production for neurons.

Dendrites are the projections of neurons, which act as the contact site for other neurons. They receive electrochemical signals from other cells and send them to the soma for further processing. The axon hillock, located at the end of the soma, controls various membrane mechanisms necessary for generating electrical signals. If the total amplitude of signals received by the dendrites exceeds the axon hillock's threshold, the neuron generates a new electrical impulse called an action potential. Axons are extended parts of neurons that conduct action potentials. They originate from the soma and usually extend over a long distance; however, they generally have a constant diameter. The axon's primary role is to transmit information to and from other neurons within the brain and spinal cord as well as other neurons in the PNS [5, 25]. Notably, the length of an axon varies according to its location and function. For instance, axons in the sciatic nerve can reach up to 1.5 m [26], whereas axons in the brain or certain parts of the spinal cord are very short (in the range of millimeters).

Axon terminals are separated from the dendrites of other neurons by a small gap called a synapse. Generally, it is unlikely for an axon to branch or form a synaptic contact before its termination [27]. The synaptic junctions allow information to pass from one cell to another electrochemically through the discharge of neurotransmitters, which are present in vesicles in the axons' terminal boutons [25].

1.2.4 Glia Cells

The other common type of cells present in the nervous system is called glial cells. These cells, which are categorized into four groups (ependymal cells, astrocytes, microglia, and oligodendrocytes [28]), provide support and nutrition for other neuronal cells. In addition, they play an essential role in recycling excess neurotransmitters released between cells [29]. Oligodendrocytes improve the propagation speed of the action potential by forming a fatty insulating material, called myelin, around the axons (Fig 1.5) [28].

1.2.5 Myelin sheath

Almost all axons in the CNS, with a diameter of 0.2 μm or larger, are covered with a myelin sheath [30]. The thickness of this myelin sheath is proportional to the diameter of the axons [31, 32]. Myelinated axons have a higher conduction velocity than that of unmyelinated axons. In mammals, unmyelinated axons transmit signals at velocities ranging from 0.5 to 10 m/s whereas myelinated axons transmit signals at velocities reaching up to 150 m/s [33] depending on their function, diameter, and electrophysiological properties [34]. Thanks to this high conduction velocity of myelinated axons, they help drive fast actions,

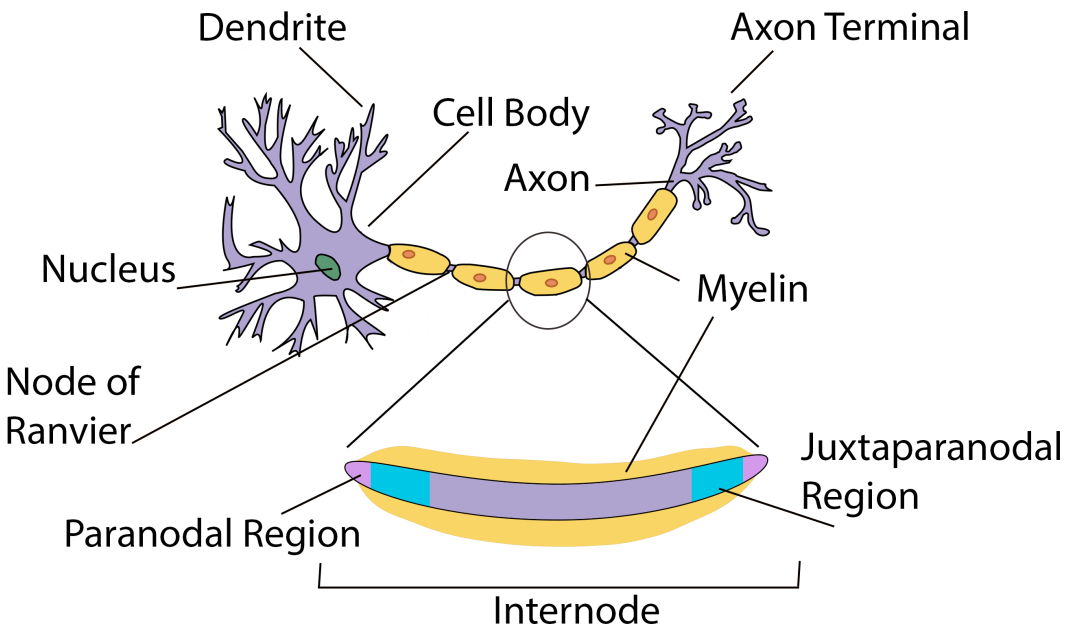

Figure 1.5: an illustration of a neuron cell. Adapted from Wikipedia, User:Dhp1080 (https://commons.wikimedia.org/wiki/File:Neuron.svg). The original image was modified by adding a zoomed view of the axonal section at the bottom by Ehsan Daneshi. The original and modified figures are licensed under CC BY-SA 3.0 (https://creativecommons.org/licenses/by-sa/3.0/legalcode).

such as the fast movement of muscles or signaling of temporally rapid events. On the other hand, unmyelinated axons help drive fine and smooth muscle movement or propagate sensory signals such as pain and temperature. Notably, along the axons, the myelin sheath is segmented with small gaps, which are called the nodes of Ranvier. The size of these gaps is generally proportional to the axon's diameter [35]. These nodes of Ranvier are covered with a large number of different voltage-gated ion channels, such as sodium and potassium channels, which generate action potential signals. The region between every two consecutive nodes of Ranvier is called the internodal region. This region is covered by a spirally wound multilamellar myelin sheath and has a nearly circular cross section. However, the internodal region in myelinated axons is connected to the nodes of Ranvier through paranodal and juxtaparanodal regions (Fig 1.5) at its both terminal ends. The myelin sheath is attached to the axon at paranodal regions located next to the nodes of Ranvier and forms septate-like junctions with the axolemma, the axon's cell membrane. These junctions act as a barrier that limits the movement of active axonal channels and ions between the nodal and internodal regions [36]. On the other hand, the juxtaparanodal regions (Fig 1.5) are located between the paranodal regions and the middle part of the internodes. They are covered with potassium channels that are separated from the nodes of Ranvier with paranodal junctions

(see section 1.2.6). Unlike paranodal regions with tight myelin-axolemma junctions, a gap exists between the innermost myelin layer and the axolemma in juxtaparanodal regions called the periaxonal space. Previous research has shown that the integrity of the myelin sheath in paranodal and juxtaparanodal regions may have an important effect on axonal function [37].

1.2.6 Electrophysiology of Neurons and Action Potential Generation

Neurons are packed with a huge number of molecules and charge-carrying ions, such as sodium and potassium. Every cubic micron of cytoplasm (intracellular solution) contains about 10^8 ions, 10^{10} water molecules, 10^7 smaller molecules (e.g., amino acids), and 10^5 proteins. Sodium (Na^+), Potassium (K^+), Calcium (Ca^+) and Magnesium (Mg^+) ions are some of the common cations and chloride (Cl^-) ion is an example of the anions present in nerve cells [38]. Generally, only sodium, potassium, and chlorine play an essential role in the cell activity of neurons, such as action potential generation [1].

Neurons have specific biophysical properties that allow them to communicate with each other using electrochemical signals. The neural membrane is a lipid bilayer with a thickness of about 3-5 nm, is impermeable to most charged molecules, and has both hydrophobic (extracellular) and hydrophilic (intracellular) sides [1]. The membrane's insulative nature causes it to act as a capacitor and does not easily allow ions to pass through. By recording the cell's inner and outer voltages, it has been shown a voltage difference exists at all times, which is called the membrane potential. Usually, the negative charge inside the neuron is higher than in the extracellular space, making the inner part more negative than the outer part. Notably, because of the high concentration of these negative charges, they repel each other, spread near the neuron membrane's inner surface, and produce an electrical field that attracts the same quantity of positive ions from the extracellular area [38]. However, several embedded channels in the membrane lower the resistance for ions to flow (the new resistance level is about 10,000 times lower than that of the pure lipid bilayer). Generally, the density and type of ion channels vary from one cell to another depending on the cell function, species, and location [39], which directly affects the neurons' electrical activity [40]. The density of ion channels varies from a few to hundreds of channels per square micron, with hundreds of thousands to even millions of channels in total. Ion channels are usually selective and allow specific ions to pass through. These channels are identified by their most permeable ion, sodium channels. The conductance of ion channels changes as a result of several factors, such as membrane voltage (e.g., sodium voltage-dependent channels), internal concentration of ions (Ca^{2+} dependent channels), and extracellular concentration of neurotransmitters or neuromodulators (synaptic receptor channels) [1]. These types of ion channels that do not have fixed conductance are called active ion channels. On the other hand, some other ion channels have constant permeability, which are called passive channels.

Generally, the outer cell potential is assumed to be zero. Moreover, because of the excess concentration of negative ions inside the cell, the cell's inner potential is negative. During the resting state, the difference between the outer and the inner concentrations of specific ions, such as sodium and potassium, is almost constant. This is achieved through ion pumps called electrogenic pumps. These pumps consume energy and pump ions in and out, maintaining the resting potential and regulating cell volume. Energy is derived from the hydrolysis of adenosine triphosphate (ATP) molecules. Under normal conditions, the flow of inward and the flow of outward ions are equal, yielding a corresponding membrane potential called the resting potential. In many cells, the resting potential is around -65 mV. However, under normal conditions, the membrane potential can range from -90 to +50 mV [38].

Myelinated axons conduct action potentials faster than unmyelinated axons through a process called saltatory conduction. When the membrane potential exceeds a certain threshold, the sodium voltage-gated channels at the nodes of Ranvier open, and the neuron generates an action potential signal at that site. The influx of positive sodium ions repels other positive ions inside the myelinated axons. However, because of the myelin layer's insulative properties, the total membrane resistance and capacitance are increased. Therefore, the amount of ionic leakage from the cell membrane is much lower than in unmyelinated axons. Because of the electromagnetic nature of the force due to excessive positive ions inside the axon, the membrane potential at the next node of Ranvier increases very rapidly. This event causes the next node's sodium channels to open up and helps refresh and strengthen the action potential signal. Notably, this process repeats along the axon until the electrical impulse reaches the axonal terminal. This means myelinated axons require less surface charge on the membrane to create the same membrane potential than that required by unmyelinated axons and also require less energy to transfer one electrical impulse from the soma to the axonal terminals.

1.3 Injury and Diseases of the Central Nervous System

Acquired brain injury (ABI) refers to brain injuries that are not hereditary, degenerative, or induced by birth trauma. These injuries include TBI and non-TBI (nTBI). Generally, TBI occurs when an external force is applied to the brain, causing damage. Penetrating head injury (PHI) and closed head injury (CHI) are among the different types of TBI. Generally, it is estimated that 69 million people sustain a TBI each year worldwide [41]. Sports injuries, motor vehicle crashes, falls, blast injuries, and violence injuries are among the top events causing TBIs [42–45]. On the other hand, diseases such as stroke, meningitis, infections, brain tumors, and oxygen deprivation may result in nTBI. Around 80% of patients admitted to hospitals with TBIs have mild TBIs (mTBIs) [46] and their symptoms eventually resolve. Although studies are somewhat contradictory [47], previous research has suggested that

some types of brain injuries can increase the risk of Alzheimer's disease [48] or other types of mental or functional problems years after the injury itself [49, 50]. In the USA, at least 125,000 people have brain injuries so severe that they require extensive hospital care, a service that is difficult to find and even more difficult to access [51].

Similarly, traumatic SCI occurs when an external trauma damages the spinal cord. Generally, it is estimated that 40,000 people with SCIs live in Canada, with an additional 1,500 cases every year, costing the healthcare system approximately $3 billion annually [52]. The largest proportion of SCIs (48.3%) occurs as a result of car accidents [53] with falls being the leading cause of SCIs in patients aged 60 or above [54, 55].Acts of violence (primarily gunshot wounds) and sports accidents are also considered leading causes of SCIs [53]. Generally, SCIs are more common in men (80%) than in women, with the average age at which injury occurs being 42.6 years [56]. After an SCI, the person's sensory and motor reflexes are usually affected. However, according to the severity and level of injury, the effects and clinical symptoms of SCI differ. The functional deficits associated with such an injury may be limited to pain or partial loss of some sensory functions, such as touch or heat. In more severe cases, the effects of injury might lead to paraplegia or quadriplegia. After an SCI, because of the pain and other related problems, such as the inability to work, the quality of life of many patients significantly changes. In addition, the diagnosis and long-term treatment and care for these individuals incur large costs for both the patients and the government.

Multiple sclerosis (MS) is a chronic degenerative and disabling disease that affects the white matter tissue in the CNS. Canada has one of the highest rates of MS in the world. There are about 290 MS cases per 100,000 population in Canada [57]. Generally, MS is more common in women than in men [58]. However, the cause of MS is still unknown. Patients with MS may experience partial or complete paralysis, visual problems and partial blindness, motor function deficits, and speech problems [59]. On average, 50% of patients with MS require assistance during walking 15 years after the first onset of MS [60]. The hallmark of MS is the demyelination of axons, which appears as lesion plaques or scars on magnetic resonance imaging (MRI) of the brain and spinal cord tissue. The diagnosis of MS is based on the timing of the disease course and symptoms and the collection of evidence that indicates demyelination and chronic inflammation of the CNS.

One of the most common pathological features of TBI and SCI is the diffuse axonal injury (DAI), which damages the white matter tissue. Generally, DAI is often associated with a widespread disruption of the neuronal and axonal integrity [61–66]. Although DAI has also been reported in patients with MS, it is mostly associated with the inertial forces applied to different parts of the brain or spinal cord following injury [67] and is prevalent in moderate and severe CHI as well as in PHI. Notably, it is currently impossible to use conventional noninvasive imaging techniques, such as MRI and computed tomography (CT), to diagnose and study axonal injuries in vivo over time. Although these technologies are useful

in identifying focal brain injuries, they are not sensitive enough to spot DAIs [68]. This limitation makes correlating the pathology with clinical outcomes challenging. Notably, recent advances in imaging technologies, such as diffusion tensor imaging (DTI), have allowed researchers and clinicians to monitor the axonal tracts and quantify axonal degeneration over time. However, to study the post injury changes and underlying mechanisms in the brain and spinal cord in detail, traditional staining methods, such as APP immunohistochemistry of necropsies, should be used.

Generally, DAIs start at the time of trauma. However, neurons, particularly the axons, may experience some structural and electrochemical changes following these DAIs that may ultimately result in cell death [69, 70] within hours to days [71–73]. Disconnection of the axons after a mechanical injury is very rare (primary axotomy) [74, 75]. However, in the majority of cases, the swellings and electrochemical reactions that follow cytoskeletal disruption can induce "secondary axotomy" [76,77] and affect function over time. Changes in the axonal function can be quantified through reduced action potential amplitude, increased latency, or strange spiking activities.

Following injury, the axonal membrane may get damaged, and small transient pores usually appear in some parts of the axon, resulting in an ionic imbalance. Generally, microtubules are responsible for axonal transport. Some microtubules break after mechanical damage, causing axonal swellings that appear along the axon. Axonal blebs or swellings appear on the axonal membrane following mechanical damage as early as 5 min after injury [78]. The formation of these blebs may contribute to further cytoskeletal disruption and increase the axonal ionic imbalance.

Generally, it is believed that axonal blebbing affects the axonal function by inducing sodium channel malfunction. Many treatments are designed to target ion channels, such as sodium and potassium channels; however, the isolated effect of this morphological change on axonal conduction is still not well understood [79]. Research has suggested that calcium may enter the cytoplasm as a result of the steep concentration gradient across the membrane through the extra membrane pores that formed as a result of the mechanical injury [67]. Although no direct evidence exists, it is believed that the exceeded intracellular calcium activates calpain, which may degrade some microtubules and ultimately result in further swelling [67, 80] and even cell death.

However, it is essential to consider the morphological and electrophysiological differences between neurons when studying the relationship between injury parameters and post injury function. Previous studies have indicated that a 100-fold difference exists in the diameter of axons in the CNS, ranging from $0.1\mu m$ to $> 100\mu m$ [34]. Some previous studies have also suggested that axons with different calibers respond differently to injury. It has been shown that smaller axons in the brain are more vulnerable to trauma than larger ones [81, 82], whereas in SCI models, larger axons have been found to be more susceptible to injury than smaller ones [83–86]. Observations in previous studies have shown an inverse relationship

between the number of axonal spheroids and axonal caliber following strain injury [87]. Because of the differences in the mechanical properties of different axonal structures, their susceptibility to injury may vary. Notably, the nodes of Ranvier are the initial site of injury following mechanical stretches and may show nodal blebs [76,77]. Paranodal and juxtaparanodal regions experience high stress during mechanical injuries, which may result in myelin damage in these regions [37, 88–90].

Injury causes changes in different neuronal structures, such as ion channels [91], myelin sheaths [92,93] and microtubules, in individual neural cells and results in functional deficits [94–96]. Although the ultimate goal of all treatments is to minimize the post injury effects of CNS damage and recover the overall function, drugs target specific structures at the cellular level. Therefore, it is important to understand the underlying mechanisms of injury at the cellular level to find new potential drug targets. Computational models provide a mechanism for studying an array of structural and electrophysiological changes simultaneously and quantifying their relative effects on action potential propagation. They also help augment the results of animal studies by isolating different injury parameters and simulating their effects on axon models developed on the basis of human data. In this thesis, we study and characterize some of the most common axonal abnormalities, such as myelin damage and spheroid formation, in patients with DAI and MS and develop a series of single cell biophysical models to study the effects of these abnormalities on axonal function.

1.4 Thesis scope and objectives

Although different treatment options currently exist for patients with brain injury or SCI aimed at reducing their pain and improving their daily function, still no cure is available. Although extensive research has been performed to investigate these issues, the underlying mechanisms of injury are still not fully understood. The aim of this research is to investigate the relationship between different injury-related pathological abnormalities and the functional response of axons using computational modeling to expand the capacity of computational modeling to understand and quantify the mechanisms of axonal injury.

This thesis is organized as follows. Chapter 2 presents the necessary background information and theoretical basis for the models used in this thesis. Chapter 3 investigates the effects of paranodal myelin damage on the action potential in axons with different sizes. Following mechanical injury, the myelin sheath in paranodal and juxtaparanodal regions becomes damaged. Therefore, a biophysical model of axons with different scales was developed in NEURON [97] to investigate the effects of myelin retraction and detachment in paranodal and juxtaparanodal regions. This axonal model is based on the widely used motor neuron model developed by McIntyre et al. [98] which is described in Chapter 2. The goal in Chapter 4 was to develop a method for increasing the geometrical resolution without increasing the computational cost in computational models of axons in NEURON. Neu-

ronal abnormalities resulting from injury or disease, such as the loss of the myelin sheath, spheroid formation, and microtubule breakage, may extend over small or large regions of specific axonal structures. The models' geometrical resolution should be increased to study the functional effects of these abnormalities in fine axonal structures on signal propagation. However, the conventional methods used in NEURON to increase the geometrical resolution require a high computational power and make simulations slow, especially when studying the effect of injury in large neural networks. In Chapter 4, we introduced a novel approach to increase the geometrical resolution in models of myelinated and unmyelinated axons, which reduces the computational power required in comparison to the conventional methods. Both computational errors and the amount of reduction in the simulations' runtimes were quantified. Chapter 5 investigates the effects of spheroid formation in myelinated axons with different calibers on action potential propagation. Spheroid formation has been observed in postmortem immunohistological tissue investigations in patients with TBI, SCI, and MS. Although some studies have investigated the effects of axonal spheroids on signal propagation in unmyelinated axons, the functional effects of these spheroids in myelinated axons are still not fully understood. In addition, the amount of published data on the geometrical features of spheroids in the human brain and their differences among axons with different diameters is minimal. Therefore, we performed a comprehensive study to analyze a series of confocal images captured from postmortem brain samples of patients with MS and infarction. Different morphological features were characterized, and the results were analyzed to detect significant differences among axons with different diameters. Then, a detailed biophysical model of axonal spheroids was developed using the method introduced in Chapter 4. Moreover, a series of simulations were performed to quantify the effects of spheroid diameter, tapering, length, location, and frequency on action potential propagation in myelinated axons with different diameters.

Chapter 2

Introduction to Computational Modeling

2.1 Introduction

Due to the high level of complexity of the nervous system, it is not easy to theorize how its components interact with each other and how it works. Moreover, it is not always possible to measure all parameters directly and simultaneously because of technological and physical restrictions. Computational models are valuable tools for systematically studying complex biological systems. These mathematical models provide us with the proper tools for studying and analyzing normal and abnormal brain and spinal cord functions. The value of computational models is that we control specific parameters of interest that we cannot control in biological models. It is also possible to perform repeated experiments on the same base model to determine the effects of different tissue injuries or treatments. Computer models are effective tools for investigating the interactions of various nervous system components. However, making an accurate model that represents the important characteristics of neuronal behaviour is exceedingly complex.

2.2 Biophysical modeling of neurons

In building computational models of the nervous system, various parameters must be considered. It is important to determine the main questions that the model is trying to answer and then specify the model's level of detail and complexity. A wide diversity of mathematical models have been developed to study the excitability of neurons and analyze the dynamics of action potential propagation in the past few decades [1, 99–101]. Biological plausibility and computational cost are among the most important parameters for selecting a suitable model for a particular application. Mathematical models such as the Hodgkin and Huxley (HH) model [102] that are based on detailed analogies of biological neurons can be used to systematically and mechanistically test different hypotheses as many model parameters can be measured experimentally. These models make conceptualization easier and make the

translation of experimental observations to computational models easier. However, they are often computationally expensive and simulation of neural networks or a single cell activity for long duration can be very slow using these models. On the other side of the spectrum, there are mathematical models like leaky integrate-and-fire based models [103, 104] that are computationally efficient however a neuron is regarded as black-box model that makes representation of different biophysical components and assigning injury parameters challenging(see Figure 2.1). For example, while it takes about 1200 floating-point operations (FLOP) to compute the state dynamics of a one millisecond HH model simulation, it takes only 5 FLOPs to do the calculations for the same simulation time with the integrate-and-fire model [105]. Although integrate-and-fire based models can be tuned to generate a wide range of spiking behaviour, it is difficult to isolate the specific contributions of biological structures and physiology (e.g. membrane permeability) in these integrate-and-fire models.

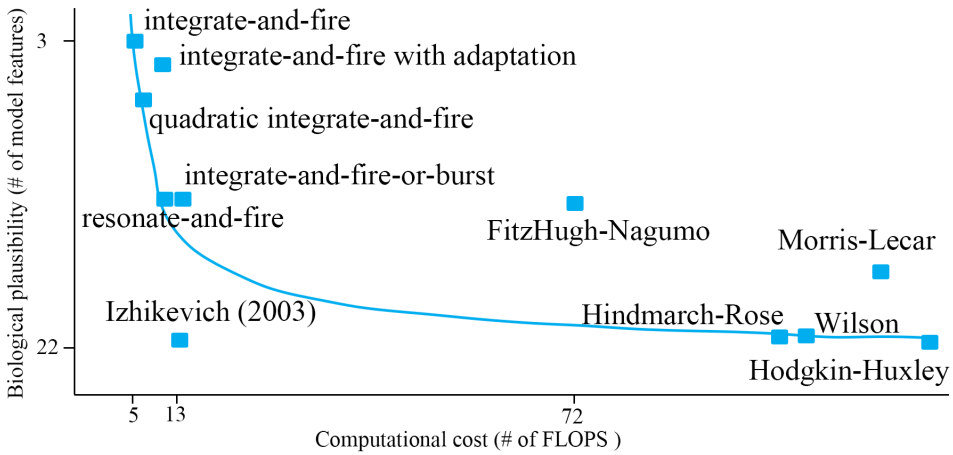

Figure 2.1: Comparison of different computational modeling techniques for neural system. Adapted from [105].

The work done by Hodgkin and Huxley in 1952 [102] is considered as one of the most successful examples of computational modelling. They developed a series of mathematical formulas [102] to describe the dynamics of membrane voltage and ionic currents of the squid giant axon, which has a large diameter, usually from $100\mu m$ to $800\mu m$ [106]. They used the patch-clamp technique, which makes the measurement of ionic influx at a constant voltage possible [107], to record intracellularly and produce experimental data required for sodium, potassium and leak current modelling. Simulations show that the proposed equations can generate action potentials similar to experimentally recorded data. Although the original Hodgkin-Huxley equations were developed for the unmyelinated squid giant axon, they have been modified and used as the base model for developing more complex and accurate models which are commonly used these days [1].

Although Hodgkin-Huxley based models are computationally expensive, the constituent components of this model represent real structures of neurons. Therefore, it is much easier

to change specific characteristics of axonal structures and relate post-injury experimental observations to function in the HH model than in other spiking and simple electrical models. However, when computational power is limited and simulation time is a concern, using HH models is not always possible. Therefore, HH models are best to use when simulating a small network of neurons or when the simulation time is not an issue. Moreover, new computational tools (NEURON, GENESIS, NEST, etc.) and online databases (Modeldb, etc.) of HH based models have been created that let researchers share their models and build on established models. Therefore, we developed our injury models based on the Hodgkin and Huxley equations and use other validated HH based models such as McIntyre's model of motor nerve fibres [2] implemented in the open-source NEURON code. Below we have a very brief review of the basic Hodgkin-Huxley equations.

2.2.1 Hodgkin-Huxley Models

Figure 2.2 shows the Hodgkin-Huxley equivalent electrical circuit which includes two time-varying and voltage-dependent resistors in series with constant batteries representing active sodium and potassium membrane channels, one constant resistor and a battery for leakage current (mostly made up chloride ions), and one capacitor that represents the membrane capacitance (C_m). The transmembrane current (I) consists of the capacitive current (I_c) and the ionic current (I_i):

$$I = I_c + I_i = C_m(\frac{dV}{dt}) + I_i \tag{2.1}$$

However, the ionic current is made up of three different components, sodium, potassium and leakage currents:

$$I_i = I_{Na} + I_K + I_L \tag{2.2}$$

Using Ohm's law, the magnitude of each ionic current is proportional to its driving force (the difference between the membrane potential, V, and the equilibrium potential of each ion, E_{Na}, E_K, E_L):

$$I_{Na} = g_{Na}(V - E_{Na}) \tag{2.3}$$

$$I_K = g_K(V - E_K) \tag{2.4}$$

$$I_L = \overline{g_L}(V - E_L) \tag{2.5}$$

Where g_{Na}, g_K, $\overline{g_L}$ are sodium, potassium, and leakage conductances (variable with time and voltage), respectively. To find the conductance values for different channels, Hodgkin and Huxley assumed that the membrane contains some gates that can block the flow of all ions or be open to the passage of the specific ion. Furthermore, individual gates are

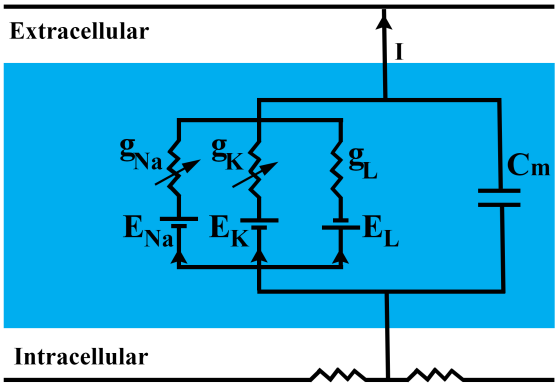

Figure 2.2: Electrical Representation of HH Model

controlled by gating particles that can also be in an open or close state at each moment [1]. For a channel to be open, all the gating particles should be in the open state. Each gating particle is assumed to be controlled by the membrane voltage and acts independently from other gating particles. Assuming the probability of a gating particle to be in the open state is n, and if a channel has x gating particles, the probability of the channel to be open will be n^x [1]. After trying to fit the best model to the experimentally collected data, Hodgkin and Huxley suggested the following formula to estimate the potassium channel's conductance in each moment:

$$g_K = \overline{g_K} n^4 \tag{2.6}$$

Where $\overline{g_K}$ is the maximum conductance of the potassium channel. To find the best fit, Hodgkin and Huxley tried different values for the power of n. As it can be seen in Figure 2.3 when n is raised to power of 4, the model matches with inflected experimental data.

The electrochemical reaction that governs the movement of gating particles from the opened (O) to closed (C) state and vice versa is explained as follows:

$$C \underset{\beta_n}{\overset{\alpha_n}{\rightleftharpoons}} O$$

Which α_n and β_n are the voltage dependent rate coefficients that determine the portion of gating particles in the open or close state. The following equations show the value of n at each moment after a step voltage change [1]:

$$\frac{dn}{dt} = \alpha_n(1-n) - \beta_n n \tag{2.7}$$

$$n(t) = n_\infty(V_1) - (n_\infty(V_1) - n_0)e^{-\frac{t}{\tau_n(V_1)}} \tag{2.8}$$

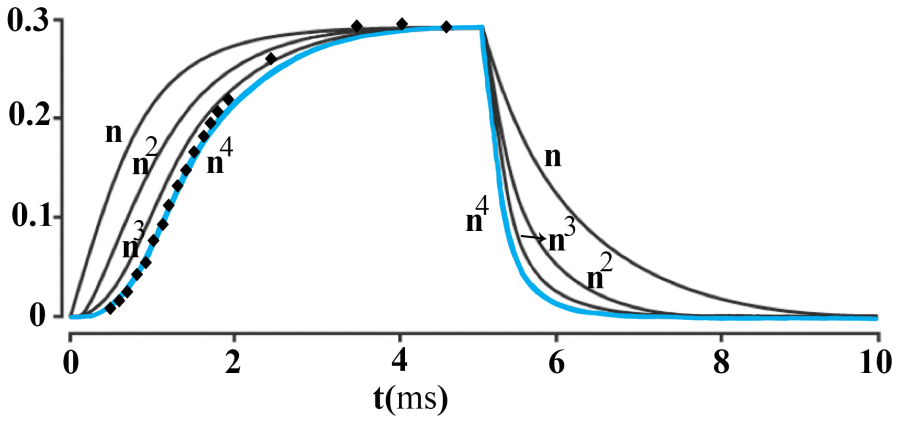

Figure 2.3: Time course of n raised to various powers. Experimental data are shown with small squares. Adapted from [102] and [1].

Where n_0 is the value of n at the start of a step ($t = 0$). Th rate coefficients, α_n and β_n, are related to $n_\infty(V)$ and $\tau_n(V)$ as follows [1]:

$$n_\infty = \frac{\alpha_n}{\alpha_n + \beta_n} \text{ and } \tau_n = \frac{1}{\alpha_n + \beta_n} \tag{2.9}$$

In the equation above, the probability of a gating particle being open at a steady membrane potential (when $t = \infty$) and time constant are shown with n_∞ and τ_n, respectively [1]. If we rewrite the equation 2.7 based on $n_\infty(V)$ and $\tau_n(V)$, then we have [1]:

$$\frac{dn}{dt} = \frac{n_\infty - n}{\tau_n} \tag{2.10}$$

By measuring the maximum conductance ($g_{k\infty}(V)$) of the channel at the voltage step experimentally, the value of of $n_\infty(V)$ at a particular voltage is [1]:

$$n_\infty(V) = \left(\frac{g_{k\infty}(V)}{\overline{g_K}}\right)^{\frac{1}{4}} \tag{2.11}$$

At each membrane potential, the time constant can be calculated by adjusting its value such that it gives the best match predicted time course of n given in equation 2.8 and experimental data [1]. By using these values, α_n and β_n can be rewritten as:

$$\alpha_n = \frac{n_\infty}{\tau_n} \text{ and } \beta_n = \frac{1 - n_\infty}{\tau_n} \tag{2.12}$$

Table 2.1 shows the equations which determine the potassium channel current. With just a few modifications, the same approach can be used to describe the kinetics of other channels. Hodgkin and Huxley used the same method to model sodium channel current and conductivity. However, in their experiments, they observed that opposite to the potassium channel, sodium conductance decreased even when the membrane voltage was clamped at a certain level. Also, they noticed that the rate of inactivation was different from the activation rate. Therefore, they proposed that the sodium channel has two different gating particles called activation, m, and inactivation, h, particles. The governing equations are as follows [1]:

$$\frac{dh}{dt} = \alpha_h(1-h) - \beta_h h \tag{2.13}$$

$$\frac{dm}{dt} = \alpha_m(1-m) - \beta_m m \tag{2.14}$$

Based on the experimental data, Hodgkin and Huxley showed that the activation curve of sodium conductance was inflected as well. However, in contrast to potassium channels, they used three activation particles to estimate sodium channel conductance:

$$g_{Na} = \overline{g_{Na}} m^3 h \tag{2.15}$$

After finding a good fit to experimental data by changing m_∞, τ_m, h_∞ and τ_h at different voltages and then $\overline{g_{Na}} m^3 h$ for all holding potentials, they converted them to coefficient rates (α_m, β_m, α_h and β_h) [1]. They tried to fit a function to the plot of each coefficient rate at different membrane voltages. The final equations are shown in Table 2.1.

So, the total ionic current in Hodgkin-Huxley model is:

$$C_m \frac{dV}{dt} = -\overline{g_L}(V - E_L) - \overline{g_{Na}} m^3 h (V - E_{Na}) - \overline{g_K} n^4 (V - E_K) + I \tag{2.16}$$

Where I represents the axial current contribution from nearby regions. However, the amount of this current is proportional to the second derivative of membrane potential with respect to space.

$$I = \frac{d}{4R_a} \frac{\partial^2 V}{\partial x^2} \tag{2.17}$$

Where R_a is axonal diameter. Also, it has been known that temperature has a significant effect on ion channels' conductance [108, 109]. Hodgkin and Huxley introduced a new term in their model and named it the temperature coefficient:

Table 2.1: Hodgkin-Huxley equations of sodium and potassium currents when V_{rest} = -65 mv [1]

	Potassium	**Sodium**
Current	$I_K = \overline{g_K} n^4 (V - E_K)$	$I_{Na} = \overline{g_{Na}} m^3 h (V - E_{Na})$
First gating particle (activation)	$\frac{dn}{dt} = \alpha_n(1-n) - \beta_n n$ $\alpha_n = 0.001 \frac{V+55}{1-e^{-(\frac{V+55}{10})}}$ $\beta_n = 0.125 e^{(-(\frac{V+65}{80}))}$	$\frac{dm}{dt} = \alpha_m(1-m) - \beta_m m$ $\alpha_m = 0.001 \frac{V+40}{1-e^{-(\frac{V+40}{10})}}$ $\beta_m = 4 e^{(-(\frac{V+65}{18}))}$
Second gating particle (Inactivation)	-	$\frac{dh}{dt} = \alpha_h(1-h) - \beta_h h$ $\alpha_h = 0.07 e^{(-\frac{V+65}{20})}$ $\beta_h = \frac{1}{1+e^{(-(\frac{V+35}{10}))}}$

$$Q_{10} = \frac{\text{rate at } T + 10^{0C}}{\text{rate at } T} \tag{2.18}$$

So by having the values of α and β at temperature T_1, the modified values at temperature T_2 would be [1]:

$$\alpha(V, T_2) = \alpha(V, T_1) Q_{10}^{\frac{T_2 - T_1}{10}} \quad and \quad \beta(V, T_2) = \beta(V, T_1) Q_{10}^{\frac{T_2 - T_1}{10}} \tag{2.19}$$

Following injury different axonal structures may get damaged and studying the isolated and combined effects of these abnormalities on function is important for understanding the underlying mechanisms of injury and potential treatments. The detailed representation of biological structures in Hodgkin-Huxley models allows for changing different model parameters systematically and augments the results of experimental studies. For example, previous research has shown that following mechanically induced injury, axonal cytoskeleton may get perturbed and axolemma permeability changes [110, 111]. The effects of these changes in axolemmal permeability on axonal function can be studied by changing the leakage conductance and membrane capacitance in the HH model. However, the effects of trauma is not limited to structural changes, but, it also initiates some functional variations in ion channels including sodium and potassium channels that leads to change of ionic concentrations [112, 113]. For example, in contrast to sodium channels in intact axons which have low conductivity at neuron resting potential, after the injury sodium channels become leaky

which means they become activated and deactivate at lower membrane potentials (leaky channels). By changing the sodium channel conductance level and the values of activating and inactivating gating particles, the functional effects of injury and potential treatments such as in CNS disorders can be studied.

2.3 NEURON Simulation Platform

NEURON is an open-source simulation platform for modelling single nerve cells or large neural networks [97]. NEURON has built-in customized functions for calculating state variables and other parameters defined and used by many mathematical models of neurons, including the Hodgkin-Huxley model. This gives the computational neuroscience researchers an advantage to focus more on their research questions, translation of experimental observations, and study design rather than the details of implementing their computational models. Moreover, one of the key features of NEURON is its ability to separate the structural and electrophysiological properties of each neural structure. In other words, one can seamlessly conceptualize neurons' geometrical and morphological properties based on experimental measurements and set the electrophysiological properties separately regardless of the anatomical features.

In NEURON, the complex structures of neural cell bodies, axons and dendrites can be described by using unbranched cylindrical sections [97, 114]. Long structures like axons are formed by connecting a series of small cylinders (sections). NEURON has a unique method of spatial discretization. Following defining anatomical and biophysical properties, each section can be divided into several segments (compartments) of equal length using the discretization parameter, "Nseg". By default, each section consists of one segment, and NEURON calculates membrane voltage and currents at the start, middle and endpoints of the section. Local spatial accuracy can be increased by increasing the Nseg parameter that is associated with the sections in the regions of interest. Increasing the number of segments results in the calculation of voltage in shorter intervals along the section; however, it increases computational cost exponentially. NEURON uses the implicit Euler method, which provides first-order accuracy (which means that the local error is proportional to integration step size, Δt.) in time and ensures the stability of simulations [114]. However, depending on the application and type of model, other integration methods can be used that affect the stability, accuracy and efficiency of simulations. For example, the Crank-Nicholson method is more computationally expensive; however, it provides second-order accuracy in time (that means that the local error is proportional to the square of Δt, thus providing significant higher accuracy) and formally stable for all time steps [115]. In this thesis, the cnexp method [2, 114] was used to solve the linear ordinary differential equations (which includes Hodgkin-Huxley ion channels models) used in the base axonal model [2] (described in the next section) and modified models (described in chapters 3, 4 and 5) of

injury. This method is an implicit integration method that ensures stability even for models that a wide range of time constants (because of membrane properties, current source, etc.) coexist in the system. The results of the simulations solved by cnexp method have second order accuracy in time [114].

NEURON has advanced tools for defining and assigning different anatomical features and biophysical membrane mechanisms to each section in the model. A neuron cell model can be constructed using two general file types: 1 - model description language (NMODL) files that describe ion channel dynamics and 2 - HOC files that let the user define the cell's geometrical and electrophysiological properties. Many biophysical mechanisms and other electrochemical sources are distributed over the cell's membrane. These *density mechanisms* can be defined in terms of current per unit area and conductance per unit area. The biophysical properties of each segment are unique along its length. Therefore, by increasing the number of segments and assigning different values for each segment's biophysical parameters, one can alter the distribution of density mechanisms along each section in NEURON. Although NEURON has built-in Hodgkin-Huxley (hh) and passive channels, there are many ionic currents and neural dynamics that cannot solely be explained by using these two channels. Therefore, NEURON allows advanced users to develop models of new and more complex mechanisms by using model description language (NMODL). NEURON is also able to separate the mechanisms which are the same across a section (ex. HH and passive channels) and the processes that belong to just one specific point along a section. One of the most important examples of point processes is the intercellular stimulation, which should be defined and applied to a specific point along a section. Conversely to density mechanisms, these parameters are usually expressed with absolute terms such as nA instead of nA/cm^2.

NEURON is an expandable software that lets the user write custom scripts in Python or HOC programming language to develop new mechanisms and simulate complex scenarios. However, developing a model of a new or custom neural mechanism can be challenging as access to experimental data to validate the model is limited. NEURON has been used widely by computational neuroscientists around the world. ModelDB [116] is an online database of user-defined and published mechanisms such as voltage-gated ion channels for NEURON, which are written in NMODL language. These models can be downloaded and integrated with custom models in NEURON. Employing ModelDB files facilitates developing and validating new models against published literature and experimental data.

2.4 McIntyre Model

Different types of neuronal models have been developed to study the behaviour of neurons under different conditions. However, to study post-injury structural and physiological changes in axonal function, biophysical models with accurate geometrical properties are needed. The axonal model developed by McIntyre and colleagues [98] is based on detailed

morphological measurements from motor neuron fibres in humans, cats, and rats. The model is validated with experimental data for fibres with the diameters of $5.7\mu m$ to $16\mu m$. Unlike most of the models before the McIntyre model, this model incorporates a double cable structure that allows accurate modelling of myelin layers in non-nodal sections. This structure separates the electrical representation of the myelin layer from the axolemma. Moreover, since this model was implemented in NEURON, it is possible to change the geometrical and electrophysiological properties of each section individually and simulate axonal abnormalities more accurately. In addition, paranodal, juxtaparanodal and internodal sections are modelled separately in the McIntyre model, which makes it a plausible choice for studying myelin injury in this study. The McIntyre model has been used extensively for studying axonal conduction in different applications [117–121] including deep brain stimulation [122], multi-scale simulation of peripheral nerves [123] and studying the effects of re-myelination in rat CNS [124].

To understand how the McIntyre model generates and propagates action potentials along the axon, the equivalent equations that govern the membrane voltage and ionic currents are derived [3, 98] and described below.

2.4.1 Non-nodal sections

Since the McIntyre model has a double-layer structure, in each internodal section, two potentials should be measured: 1- The potential difference between inner cell (V) and periaxonal space, and 2- the potential difference between the periaxonal space and extracellular space. Following the derivation of McIntyre model's ionic dynamics and membrane potentials in [3], at each point along the axon, the inner axonal and periaxonal potentials for the K^{th} compartment are defined as follow:

$$V_K^i = E_K^i - E_K^p \tag{2.20}$$

$$V_K^p = E_K^p - E_K^e \tag{2.21}$$

Note that the potentials denoted with superscript i, p and e represent inner axonal, periaxonal and extracellular potentials, respectively. Also, the letter E means that the potentials are measured against ground potential. Using Kirchhoff's current law, the total inner axonal current at each point in the non-nodal segments is equal to:

$$I_K^{axial-left} + I_K^{axial-right} + I_K^{membrane} = 0 \tag{2.22}$$

$I_K^{axial-left}$ and $I_K^{axial-right}$ are the axial currents which come from the adjacent points and are defined as follows:

$$I_K^{axial-left} = \frac{E_K^i - E_{K-1}^i}{\frac{R_K^i + R_{K-1}^i}{2}} \tag{2.23}$$

$$I_K^{axial-right} = \frac{E_K^i - E_{K+1}^i}{\frac{R_K^i + R_{K+1}^i}{2}} \tag{2.24}$$

In the McIntyre model, there is no active ion channel in non-nodal areas, so the total current that goes through the membrane is just because of passive channels and leakage current. These currents can be categorized into ionic and capacitive currents:

$$I_K^{membrane} = I_K^{mem.ionic} + I_K^{mem.capacitive} \tag{2.25}$$

$$I_K^{mem.ionic} = G_K^{mem}.(E_K^i - E_K^p - E_K^{passive}) \tag{2.26}$$

$$I_K^{mem.capacitive} = C_K^{mem}.\frac{d(E_K^i - E_K^p)}{dt} \tag{2.27}$$

Therefore, by rewriting equation 2.1, we have:

$$\frac{E_K^i - E_{K+1}^i}{\frac{R_K^i + R_{K+1}^i}{2}} + \frac{E_K^i - E_{K-1}^i}{\frac{R_K^i + R_{K-1}^i}{2}} + G_K^{mem}.(E_K^i - E_K^p - E_K^{passive}) + C_K^{mem}.\frac{d(E_K^i - E_K^p)}{dt} = 0 \tag{2.28}$$

Where

$$\frac{dV_k^i}{dt} = \frac{\frac{E_K^i - E_{K+1}^i}{\frac{R_K^i + R_{K+1}^i}{2}} + \frac{E_K^i - E_{K-1}^i}{\frac{R_K^i + R_{K-1}^i}{2}} + G_K^{mem}.(E_K^i - E_K^p - E_K^{passive})}{C_K^{mem}} \tag{2.29}$$

The same form of equations can describe the periaxonal currents:

$$I_K^{periaxonal-left} + I_K^{periaxonal-right} + I_K^{myelin} - I_K^{mem} = 0 \tag{2.30}$$

$$I_K^{periaxonal-left} = \frac{E_K^p - E_{K-1}^p}{\frac{R_K^p + R_{K-1}^p}{2}} \tag{2.31}$$

$$I_K^{periaxonal-right} = \frac{E_K^p - E_{K+1}^p}{\frac{R_K^p + R_{K+1}^p}{2}} \tag{2.32}$$

$$I_K^{myelin} = I_K^{myelin.ionic} + I_K^{myelin.capacitive} \tag{2.33}$$

$$I_K^{myelin.ionic} = G_K^{myelin}.(E_K^p - E_K^e) \tag{2.34}$$

$$I_K^{myelin.capacitive} = C_K^{myelin}.\frac{d(E_K^p - E_K^e)}{dt} \tag{2.35}$$

$$I_K^{periaxonal-left} + I_K^{periaxonal-right} + I_K^{myelin} + I_K^{axial-left} + I_K^{axial-right} = 0 \tag{2.36}$$

$$\frac{dV_K^p}{dt} = \frac{-\left(C_K^{myelin}.V_K^p + \frac{E_K^i - E_{K-1}^i}{\frac{R_K^i + R_{K-1}^i}{2}} + \frac{E_K^i - E_{K+1}^i}{\frac{R_K^i + R_{K+1}^i}{2}} + \frac{E_K^p - E_{K-1}^p}{\frac{R_K^p + R_{K-1}^p}{2}} + \frac{E_K^p - E_{K+1}^p}{\frac{R_K^p + R_{K+1}^p}{2}}\right)}{C_K^{myelin}} \tag{2.37}$$

2.4.2 Nodes of Ranvier

McIntyre included three active ion channels and one passive channel in the nodal areas of his model. These channels are all modelled based on the Hodgkin-Huxley equations. However, the HH parameters were changed and tuned to match experimental results. The general form of current for each ion channel is:

$$I_{ionic} = g_{ionic}(V - E_{ionic}) \tag{2.38}$$

Table 2.2: Equations describing active channels current dynamic at 36 degrees of Celsius [2,3]

	Slow Potassium	**Fast Sodium**	**Persistent Sodium**
Current	$I_{K-slow} = \overline{g_{K-slow}} S(V^i - E_K)$	$I_{Na-fast} = \overline{g_{Na-fast}} m^3 h(V - E_{Na})$	$I_{Na-per} = \overline{g_{Na-persistent}} P^3 h(V^i - E_{Na})$
First gating particle (activation)	$\alpha_s = \frac{0.3}{1-e^{\frac{(V^i+53)}{-5}}}$ $\beta_s = \frac{0.3}{1-e^{\frac{V^i+90}{-1}}}$	$\alpha_m = \frac{6.57(V^i+21.4)}{1-e^{\frac{-(V^i+21.4)}{10.3}}}$ $\beta_m = \frac{0.304.(-V^i-25.7)}{1-e^{\frac{V^i+25.7}{9.16}}}$	$\alpha_p = \frac{0.0353(V^i+27)}{1-e^{\frac{-(V^i+27)}{10.2}}}$ $\beta_p = \frac{0.000883.(-V^i-34)}{1-e^{\frac{V^i+34}{10}}}$
First gating particle (activation)		$\alpha_h = \frac{-0.34(V^i+114)}{1-e^{\frac{(V^i+114)}{11}}}$ $\beta_h = \frac{12.6}{1-e^{-\frac{V^i+31.8}{13.4}}}$	

The total nodal current is:

$$I^{membrane} = I^{Na_{fast}} + I^{Na_{persistent}} + I^{K_{slow}} + I^{leakage} + I^{membrane_{capacitive}} \tag{2.39}$$

$$I^{leakage} = G^{membrane}.(V^i - E^{leakage}) \tag{2.40}$$

So nodal voltage at each time would be [2, 3]:

$$\frac{dV_K^i}{dt} = -\frac{I^{Na_{fast}} + I^{Na_{persistent}} + I^{K_{slow}} + I^{leakage} + I^{axial-left} + I^{axial-right}}{C_K^{membrane}} \tag{2.41}$$

Chapter 3

The Effects of Paranodal Myelin Damage on Action potential Depend on Axonal Structure

3.1 Abstract

Biophysical computational models of axons provide an important tool for quantifying the effects of injury and disease on signal conduction characteristics. Several studies have used generic models to study the average behavior of healthy and injured axons; however, few studies have included the effects of normal structural variation on the simulated axon's response to injury. The effects of variations in physiological characteristics on axonal function were mapped by altering the structure of the nodal, paranodal and juxtaparanodal regions across reported values in three different caliber axons (1μm , 2μm, and 5.7μm). Myelin detachment and retraction were simulated to quantify the effects of each injury mechanism on signal conduction. Conduction velocity was most affected by axonal fiber diameter (89%) while membrane potential amplitude was most affected by nodal length (86%) in healthy axons. Post-injury axonal functionality was most affected by myelin detachment in the paranodal and juxtaparanodal regions when retraction and detachment were modeled simultaneously. The efficacy of simulated potassium channel blockers on restoring membrane potential and velocity varied with axonal caliber and injury type. The structural characteristics of axons affect their functional response to myelin retraction and detachment and their subsequent response to potassium channel blocker treatment.

3.2 Introduction

During the last two decades great advancements have been made in understanding the cascade of complex events following spinal cord injury (SCI). Many compounds and strategies have been demonstrated to be neuroprotective in experimental models of SCI; however, few have translated to clinical treatment [125]. Although overall function is the primary outcome

of interest for spinal cord injured patients, experimental drug treatments mostly target the subcellular structural changes that occur after an injury and their mechanisms of action differ. There is now a significant focus on combined therapies for improving outcomes in spinal cord injured patients [126, 127]. However, it is critical to understand the mechanism and specific effect of each structural change that results from SCI on axonal conduction to optimize treatment protocols.

Computational models can increase our understanding of experiments and subsequent mental models [128]. Computational models of single axons have been developed to link mechanical impacts, pathophysiological changes and functional outcomes [37, 94, 95, 112, 129]. Results from these models show that axonal damage, induced by mechanical impact, disrupts action potential propagation and slows conduction velocity in axons. However, computational studies of myelin damage used single generic axon models but each model assumed very different structural parameter values [37, 79, 95]. In reality, axon caliber varies 100-fold (0.1 μm - 10 μm) and the corresponding volume varies 10000-fold within a single tract [34]. Variations in structural characteristics affect signal conduction in healthy axons [130, 131] and in vivo studies suggest axon caliber may affect its response to mechanical loading and resulting damage [81–84, 86]. The combined effects of normal axonal structural variations and demyelinating damage have not been addressed by computational models.

Biophysical models provide computational representations of individual structures within the neuron which provides the opportunity to systematically control and quantify the role of structural variations in normal axons on their neurophysiological responses to injury and treatment at the cellular level. There have been numerous biophysical models developed to simulate axonal conduction [94, 132]. The MRG model is one of the most widely studied biophysical models, has been originally validated for several calibers of healthy axon from 5.7 μm to 16 μm [98] and was used for studying healthy and damaged axons [3, 133–141] in central nervous system (CNS) and peripheral nervous system (PNS). The open-source structure of the MRG model makes it efficient to advance existing work in the field and create a new linked method to iteratively run large batch simulations.

The overall goal of this study was to quantify the varied effects of axonal structural damage on axonal conduction by integrating the approach which was developed by Babbs and colleagues [37] for simulating myelin damage and the MRG model [98] of myelinated axons. Our hypotheses were 1) that axonal caliber would affect functional responses to demyelinating injury and 2) that axonal caliber would affect the functional response to simulated potassium channel blocker treatment. The specific objectives were 1) to map the effects of variations in normal axonal structure on predicted signal conduction characteristics using a biophysical computational model; 2) to quantify the effects of myelin retraction and detachment in paranodal and/or juxtaparanodal regions on axonal conduction characteristics for three different axon calibers; and 3) to quantify the variation in axon response to potassium channel blockers for three different axon calibers and to compare against

observed laboratory outcomes. This is the first study to integrate normal structural variation into computational models of paranodal myelin damage, expands the applicability and robustness of injury modelling, and highlights the interactive effects of normal structural variations, damage and treatment mechanisms on axonal function.

3.3 Methods and Materials

3.3.1 Biophysical Model of an Axon

To study the effect of damaged axonal structures on signal conduction characteristics, a biophysical computational model of a single axon based on the McIntyre model [98] of a mammalian motor nerve fibre, commonly known as MRG model, was implemented in NEURON [114]. Base model [98] files have been obtained from ModelDB [132]. This single axon model [98] has been used for various applications such as deep brain stimulation and transcutaneous spinal cord stimulation [135, 136, 142] and provides the ability to independently control structural characteristics that affect axonal function. This geometrically accurate model incorporates a double-cable structure in non-nodal sections with a finite impedance myelin sheath and a leakage pathway to the axolemma (Fig.3.1a and Fig.3.1b). Using this base model, we modified the NEURON implementation in order to control each model parameter independently through a Matlab (V8.6, The MathWorks, Inc) script. The Matlab script was developed to allow for change of geometrical and electrophysiological properties of each axon systematically. The behavior of our implementation of the model was confirmed using parameters assigned to the 5.7μm axonal fiber and comparing with published results [98].

3.3.2 The effects of structural variations on function in an intact axon

Axonal characteristics vary between species and within individuals [34]. Recent computational studies of myelin damage have developed single generic intact axon models assuming very different structural parameter values [37, 79, 95]. However, the effect of these variations in normal axonal structural characteristics on modeled membrane potential response is unclear. Previous studies have shown that following SCI, nodes of Ranvier, paranodal and juxtaparanodal regions tolerate high amount of stress [143, 144]. To further investigate the sensitivity of the base model to parameters involved in injury, six structural parameters that may be affected by mild SCI and subsequent myelin damage [37, 143, 145] in the nodal, paranodal and juxtaparanodal areas were identified (Table 3.1). To account for axonal caliber variability, nodal diameter was also added to the list of study parameters and its value was changed over a range (0.7μm - 5.5μm) of reported values [98, 138]. In total, 7 parameters were studied and their values were changed independently over physiologically occurring values to first determine their effect on normal axonal signal conduction (Table 3.1). Six additional structural parameters of the model that are dependent on the seven independent

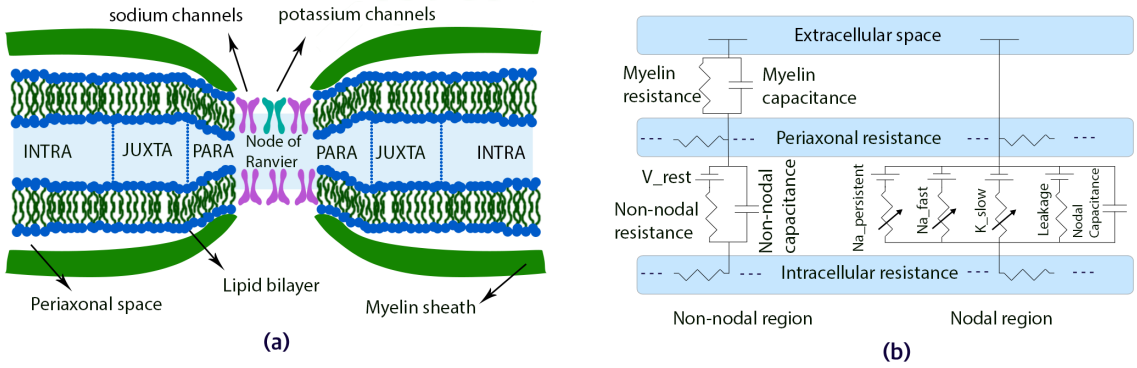

Figure 3.1: (a) Schematic of an intact myelinated axon adapted from McIntyre et al. [98]. Nodes of Ranvier are covered with sodium channels and slow potassium channels. Myelin sheaths are tightly connected to the axonal membrane in the paranodal areas and help accelerate propagation of action potentials along axons. PARA: Paranodal areas - JUXTA: Juxtaparanodal areas - INTRA: Internodal areas (b) Electrical representation of an intact axon. Each ion channel is modeled separately based on experimental data. Membrane leak resistance and capacitance are modeled and considered in both the nodal and non-nodal regions.

parameters were proportionally varied using defined relationships [32, 98, 146–149] (Table 3.2). The density of sodium and potassium channel were kept constant in the nodes of Ranvier. An intracellular current stimulus of 2nA for 0.1ms [98] was applied to the node 1 of the axon to depolarize the node and initiate the action potential while avoiding end effects [1]. Membrane voltage and nodal current were recorded for the nodes 6 and 15 of the 21-node axon model [37, 98] with fixed times steps (0.005 ms) for 10 ms. To quantify the effects of each parameter and the interaction of these parameters on the membrane potential, conduction velocity and nodal current, 2187 simulations were run to sequentially alter the value of all seven selected axonal parameters to minimum, mean and maximum values in a full factorial design (37 simulations) (Table 3.1). Membrane potential is specified as the intracellular minus extracellular electrical potential at each node. Conduction velocity was calculated for each simulation by dividing the distance between recorded nodes by the difference in time between the peak membrane potentials that occurred at each node.

3.3.3 Modeling of subtle myelin damage in axons of different calibers

In vitro and computational models show that the myelin sheath is one of the first structures damaged in an mechanical injury [143, 145]. Demyelination may occur because of primary physical impact and the subsequent secondary biochemical reactions [145]. In the acute phase (about 2 hours post injury) of mild stretch injury (50% strain in the isolated spinal cord white matter tissue with strain rate of 1.5 m/s) [157], myelin may be retracted from

Table 3.1: Parameter values used to quantify the effects of normal structural variation in the axon on signal conduction characteristics.

Parameter	Modeled values	Formula	Reference
Axoplasmic resistivity(α)	70, 135, 200(Ω-cm)	-	[37, 95, 98]
Juxtaparanodal length(β)	10, 35, 60(μm)	-	[146, 147, 150]
Juxtaparanodal periaxonal space(γ)	0.002, 0.003, 0.004(μm)	-	[146, 147]
Nodal diameter(δ)	0.7, 3.1, 5.5(μm)	-	[151–156]
Nodal length(ϵ)	0.455, 2.01, 3.57(μm)	$\epsilon = 0.65\delta^*$	[148, 154, 155]
Paranodal length(ζ)	1, 2.5, 4(μm)	-	[146, 147]
Paranodal periaxonal space(η)	0.002, 0.003, 0.004(μm)	-	[146, 147]

Table 3.2: Axonal structures that have been shown to vary proportionally with the main axonal structures of interest were defined as dependent variables and were altered based on quantified relationships.

Parameter	Modeled values	Formula	Reference
Internodal diameter(θ)	0.8, 6.75, 12.7(μm)	$\theta = \xi$	[146, 147]
Internodal Periaxonal space(ρ)	0.002, 0.003, 0.004(μm)	$\rho = \gamma$	[146, 147]
Juxtaparanodal diameter(ξ)	0.8, 6.75, 12.7(μm)	$\xi \propto \delta$	[140, 146, 147]
Node-to-Node Length(σ)	200, 850,1500(μm)	$\sigma \propto \xi$	[32, 140, 149]
Number of Myelin lamellae(ϕ)	20, 85, 150(μm)	$\phi \propto \xi$	[32, 140, 146, 147]
Paranodal diameter (ψ)	0.7, 3.1, 5.5(μm)	$\psi = \delta$	[146, 147]

the nodes of Ranvier [89, 158]. In more severe cases, the axonal-glial junctions may be damaged and the periaxonal axonal spaces in the paranodal and juxtaparanodal areas increased [86, 145, 159, 160]. This results in a reduction in the periaxonal resistance [137, 145, 160] and could result in the exposure of fast potassium channels (Fig.3.2). It has been speculated that these changes will affect the activation of fast potassium channels [160], ionic movement, and ionic balance across the axonal membrane [161, 162], making axons generate abnormal action potentials leading to an excitotoxic response or suppressed action potentials [162, 163]. Although axonal injury is a multifaceted process and several factors play a role in determining the ultimate functional response to injury, the focus of the current study was on systematically studying the functional effects of local subtle paranodal myelin injury on axons of different calibers. Three axons (diameters of 1 μm, 2 μm and 5.7 μm) were developed using values from published studies [98, 138, 140]. The axonal models were modified such that the morphological and electrophysiological properties of each section were defined individually allowing for specific definitions of damage in each section and eliminating the co-dependence of these sections which was defined in the original base model [98] of the intact axon. This allowed for the precise definition of the extent and location of injury along the axons. The juxtaparanodal regions of axons are covered by fast potassium channels [164, 165]. The Hodgkin-Huxley based formulas [1] which describe fast

potassium channel current dynamics were previously reported [98,166] but were not included in the open source biophysical model. Therefore, models (.MOD file) of the fast potassium channels were developed and implemented in NEURON based on the equations [98] and integrated in juxtaparanodal areas of all three axons (Equation 3.1).

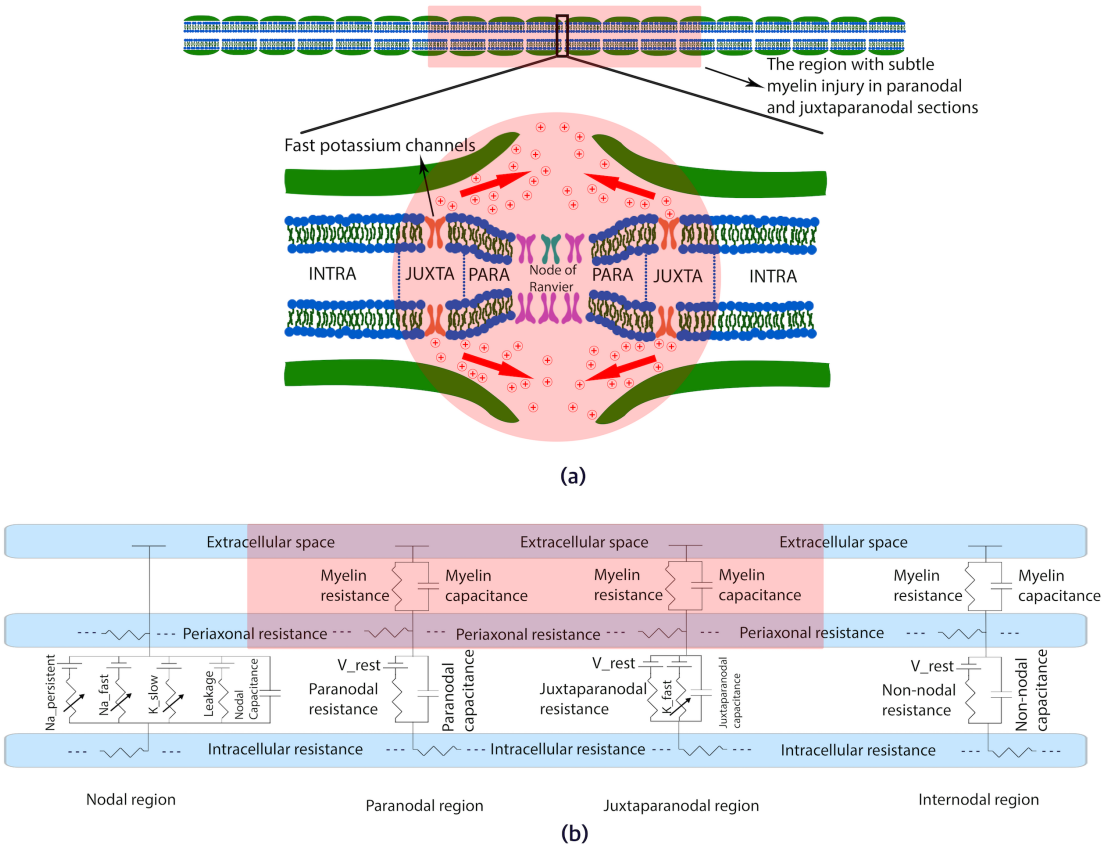

Figure 3.2: Myelin Damage and exposure of potassium channels. (a) Schematic of a damaged myelinated axon. There is a high concentration of fast potassium channels in the juxtaparanodal areas. Following subtle myelin injury (Paranodal myelin retraction and paranodal and juxtaparanodal myelin detachment), the length of the nodal area increases, the periaxonal resistance decreases and fast potassium channels become exposed. The increased outflow of potassium ions may reduce the ability of axons to conduct action potentials. PARA: Paranodal areas - JUXTA: Juxtaparanodal areas - INTRA: Internodal areas. (b) Electrical representation of a damaged axon. Fast potassium channels are modeled in juxtaparanodal regions. Myelin retraction was modeled by a reduction in myelin resistance and an increase in myelin capacitance in paranodal regions. Myelin detachment was also modelled by a decrease in periaxonal resistance in paranodal and juxtaparanodal regions.

$$
\begin{aligned}
I_{K_{fast}} &= \overline{g_{K_{fast}}} n^4 (V - E_K) \\
\frac{dn}{dt} &= \alpha_n (1 - n) - \beta_n (n) \\
\alpha_n &= 0.0462 \frac{V + 83.2}{1 - e^{\frac{-V - 83.2}{1.1}}} \\
\beta_n &= 0.0824 \frac{-V - 66}{1 - e^{\frac{V + 66}{10.5}}}
\end{aligned}
\tag{3.1}
$$

where $\overline{g_{K_{fast}}}(0.02\ S/cm^2)$ is the maximum specific conductance of the fast potassium channels.

Myelin retraction and detachment were simultaneously simulated with varying degrees of severity to evaluate the relative significance of each damage mechanism on axonal conduction. The MRG model [98] has a double cable structure to model the axon and the myelin sheath around it. Myelination is included in the paranodal, juxtaparanodal and internodal regions, while the nodes of Ranvier are unmyelinated. There is an inverse relationship between the number of myelin wraps and myelin conductance and capacitance [98]. The numbers of myelin wraps for healthy axons with diameters of 1 μm, 2 μm and 5.7 μm were 20, 30 and 80 respectively [98, 138, 140]. Myelin retraction was simulated by modeling both a reduction in the number of myelin wraps on the axon and shortening the myelin to expose damaged paranodal regions around the nodes of Ranvier. Depending on the severity of the myelin retraction, the number of myelin wraps in the damaged paranodal region was reduced (n=5) from 100 percent of the normal value for each axon to unmyelinated. In this study, we modeled the reduction in number of myelin wraps by decreasing the myelin resistance and increasing the myelin capacitance in the regions of interest. The length of the damaged paranodal area was changed incrementally (n=5) from 0 μm to 1 μm [145].

Myelin detachment leads to an increase in the size of the gap between the inner surface of the myelin and the outer surface of the axon [145]. Changing the size of this gap will result in a change in the periaxonal resistance. Although the McIntyre model defined a relationship between the size of the periaxonal gap and the periaxonal resistance, there is no experimental data that quantifies the size of periaxonal gap after injury. Following the approach introduced by Babbs and colleagues [37], periaxonal resistance values were varied (n=5) from 100 to 1 percent of their normal values. Unlike the previous study, here the periaxonal resistance values were changed for paranodal and juxtaparanodal regions separately, to have a more comprehensive picture of the effects of myelin damage on axonal function. A reduction in the periaxonal resistance to 1 percent of normal value in an axon with diameter of 2 μm is equivalent to 89 or 82 fold increases in the size of periaxonal gap in the paranodal or juxtaparanodal areas respectively. The focus of this study was to investigate the immediate effects of localized mild myelin injury in the paranodal and

the juxtaparanodal regions on axonal function. Therefore, in all simulations a maximum of one third (7 nodes of Ranvier) of the axonal length was damaged and the ion channels densities were kept constant. However, the effect of new ion channels expression or ion channel distribution along axons in later stages of injury should be investigated in future studies. In total, 2501 simulations for each axon (D=1 μm , 2 μm , 5.7 μm), were run to map the relative effects of each structural change on membrane potential and signal propagation.

To further detail the effects of myelin retraction on axonal function, three sets of simulations were done such that in each experiment, two parameters were fixed and one independent parameter was changed. In the first experiment, the internal length of the damaged paranodal regions measured from each node of Ranvier was changed incrementally (n=12) from 0 μm to 1 μm across the 7 damaged nodes, while these regions were fully demyelinated. In the second experiment, the number of myelin wraps and therefore myelin thickness in these regions was reduced (n=33) from 100 percent of normal value to 0 across 7 damaged nodes and the lengths of the damaged paranodal sections were fixed at 1 μm on either side of the nodes of Ranvier. Finally, the number of damaged nodes was varied (n=5) from 0 to 7 while the length of damaged paranodal regions was fixed at 1 µm on either side of the nodes of Ranvier and these sections were demyelinated.

To quantify the specific effects of myelin detachment on axonal function, detachment was simulated in the paranodal and juxtaparanodal regions separately and combined. First, the periaxonal resistance of the region(s) of interest was incrementally (n=33) changed from 100 to 1 percent of normal value while the number of damaged nodes remained constant (n=7). In the second set of experiments, the number of injured nodes was changed incrementally (n=5) from 0 to 7 while the periaxonal resistance value was simultaneously reduced to 1 percent of its normal value in the region(s) of interest.

Potassium channel blockers are known to reduce the effect of myelin retraction and detachment in damaged axons [158, 167]. To quantify the relative effectiveness of potassium channel blockers on myelin retraction and detachment and to verify the biofidelity of this model, the damaged axon model response to simulated potassium channel blockers was evaluated. A series of simulations were constructed that incrementally reduced the fast potassium channels' conductance from their normal value to zero (channel blocked) when axons were damaged by 1) myelin retraction, 2) myelin detachment, or 3) both myelin retraction and myelin detachment. These experiments were repeated for small (D=1 μm), medium (D= 2 μm) and large (D=5.7 μm) axons for 99% myelin detachment in the paranodal and juxtaparanodal regions, 1 μm myelin retraction on both sides of nodes of Ranvier, and 7 damaged nodes.

3.3.4 Validation

External electrical stimulation of in vitro neural tissue primarily activates axons [168, 169]. Therefore, in experimental studies that stimulated isolated strips of white matter or other nerve fibers, overall tissue characteristics like the compound action potential can be assumed to reflect the overall behavior of axonal bundles. Currently, there are no experimental results that mechanically injure individual axons, observe specific structural changes and directly measure changes in axonal conduction. Therefore, to validate the models, the electrophysiological response of the intact and damaged axons were compared to previously reported values of action potential amplitude and velocity for healthy and stretched axons [37, 92, 95, 137, 143, 145, 158, 166, 170, 171].

3.3.5 Statistical analysis

Forward linear stepwise regression (Matlab, Mathworks Inc. Natick, MA) identified the individual and combined (up to the third degree) effects of each component on the modeled membrane potential and conduction velocity. P values of <0.05 and >0.1 were used as the entrance and exit level for the stepwise regression respectively. The proportional significance of each parameter in the stepwise regression was determined by taking the difference between the fit value with the parameter included in the regression and the fit value before the parameter was added.

3.4 Results

3.4.1 Axonal structures with the greatest effect on membrane potential

Through changing axonal parameters over physiologically occurring values the variability in the membrane potential and conduction velocities for normal, healthy axons ranged from -79.95 to 46.77 mV and 2.24 to 103.5 m/s, respectively. Stepwise regression analysis demonstrated that the effects of the seven axonal structure parameters and interactions (up to the third degree) explained 75% and 94% of the variation observed in the membrane potential and conduction velocity, respectively. The rest of variation in the outcome measures is due to the higher order nonlinear terms (Fig. 3.3). Conduction velocity was most sensitive to variations in nodal diameter, nodal length and axoplasmic resistivity in the intact axon (Fig. 3.3). Nodal diameter had the greatest effect on conduction velocity (81%) while it had little effect on membrane potential (<2%). Membrane potential was most affected by nodal length (53%), axoplasmic resistivity (4%) and interaction of juxtaparanodal length (<4%). Nodal length and nodal diameter had an interaction effect on conduction velocity (5%). Variations in all other structural parameters had limited effect on membrane potential and conduction velocity in healthy axons.

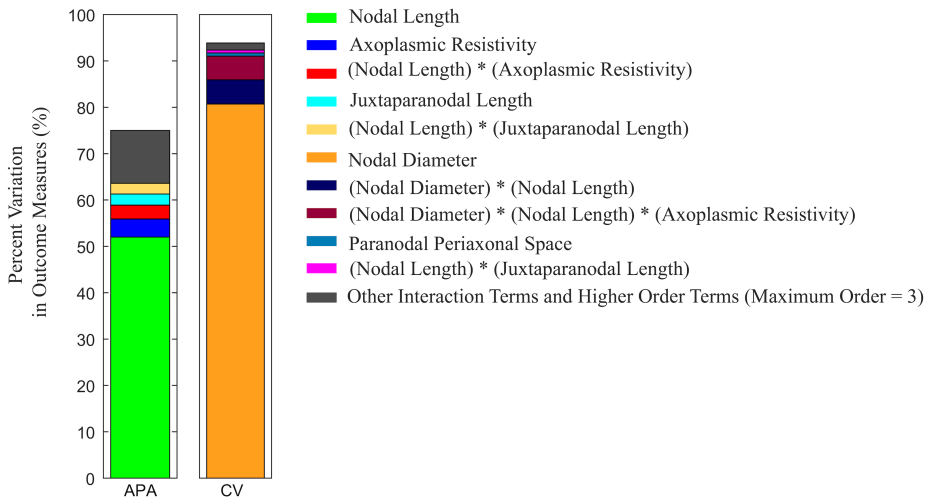

Figure 3.3: The key axonal parameters for signal propagation identified by stepwise regression analysis. The overall effects of changing the axonal parameters (See Table 3.1 and Table 3.2) on membrane potential (TP) and conduction velocity (CV). Each outcome was predominately affected by a single structural parameter. Variations in all of the other structural parameters combined accounted for less than 15% of the overall observed variation.

Healthy Axon Model Validation

The behavior of our biophysical models incorporating normal physiological and structural variations compared well with trends in behavior reported in experimental studies. Conduction velocities in the models of healthy axons varied from 2.24 to 103.5 m/s for axonal diameters of 1-5.7 μm. These values are comparable to experimentally observed values for conduction velocity of 0.1-117 m/s in cat axons [172, 173]. In our study, axonal diameter had the greatest effect (81%) on conduction velocity of all the tested parameters (Fig. 3.3). Previous experiments have shown that axonal diameter directly correlates with conduction velocity [130, 131]. The range of observed variation in membrane potential observed in this study (-79.95 to 46.77 mV) agree with published reported values for in vitro and in vivo function (-95.3 to 92.9 mV) [98, 166, 170, 174–176].

3.4.2 Myelin injury

Myelin retraction results

Although all axons showed similar overall behavior in the presence of paranodal myelin retraction, the magnitudes of the variation in membrane potential and conduction velocity were affected by axonal diameter. In general, the large axon (D= 5.7 μm) was less sensitive to structural changes due to myelin retraction compared to smaller axons (D= 1 μm and 2 μm). Across all simulations, the greatest reduction in membrane potential for the

axons with diameter of 1 μm, 2 μm, 5.7 μm was 7%, 6%, 4% respectively, while the conduction velocity was reduced a maximum of 32%, 25%, 24% respectively (Fig. 3.4). Similar maximal reductions in membrane potential and conduction velocity were seen for each of the simulated damage effects (length of paranodal area with myelin retraction, number of myelin layers, or number of damaged nodes). In all simulations, myelin retraction reduced membrane potential at the injury epicenters; however, all axons recovered signals at nodes distal to the injury epicenter.

Myelin detachment results

A series of simulations were done to quantify the effects of myelin detachment on membrane potential and signal propagation. At the epicenter of injury, membrane potential and conduction velocity were more affected by myelin detachment in the paranodal regions than myelin detachment in the juxtaparanodal regions, regardless of the caliber of the axons (Fig. 3.5, 3.6). However, the greatest reductions in membrane potential at the injury epicenter were due to myelin detachment in both the paranodal and juxtaparanodal regions. Conduction velocity was reduced by up to 66% and 65% for the axons with diameter of 1 μm, 2 μm respectively while the 5.7 μm axon was unable to propagate an action potential in the most severe cases (Fig. 5f). Membrane potential was reduced by 98% in the distal nodes in the large axon (D= 5.7 μm) when 7 nodes were damaged with 99% reductions in juxtaparanodal and paranodal resistivities; however, simulating the same conditions in axons with diameters of 1 μm and 2 μm reduced membrane potential by less than 2% (Fig. 3.5e). Reducing the periaxonal resistance in either the paranodal or juxtaparanodal spaces had a limit effect on membrane potential (<15%) (Fig. 3.6). However, injury in the paranodal region did have an effect on conduction velocity (Fig. 3.6b). The large diameter axon (D= 5.7 μm) was most affected by changes in both the paranodal and juxtaparanodal regions with a 96% reduction in resistance being sufficient to completely suppress action potential generation.

Combined myelin retraction and detachment

A series of simulations determined the relative effects of structural damage simulating myelin retraction and detachment (the length of the damaged paranodal regions, the number of myelin layers in the damaged paranodal regions, the amount of myelin detachment in the paranodal regions, the amount of myelin detachment in the juxtaparanodal regions, and number of damaged nodes) on membrane potential and signal propagation. Stepwise regression analysis showed that membrane potential at the epicenter of injury (node 10) in the 1 μm and 2 μm axons were most affected by paranodal (61%, 55%) and juxtaparanodal (18%, 17%) periaxonal resistances (Fig. 3.7 and 3.8). In contrast, in the large axon (D=5.7 μm), membrane potential at the injury epicenter was more sensitive to juxtaparanodal periaxonal resistance (24%) than paranodal periaxonal resistance (20%) (Fig. 3.9). The

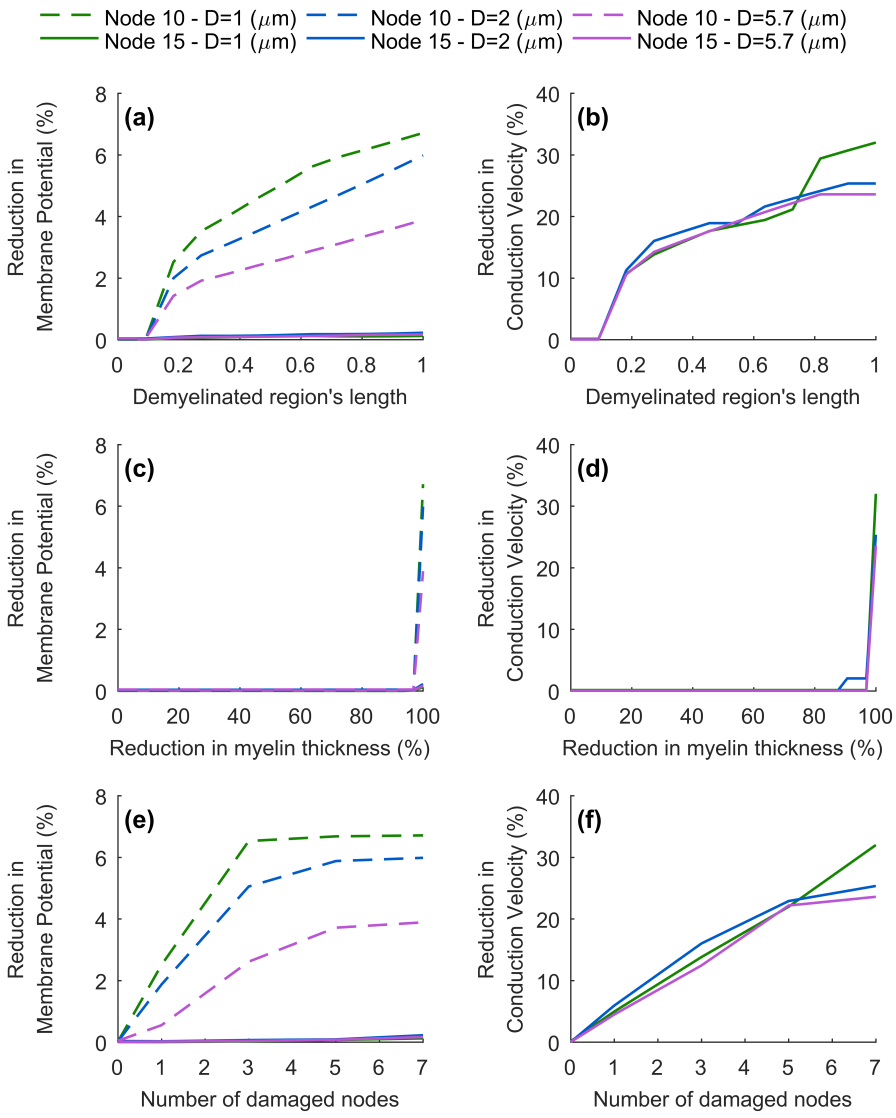

Figure 3.4: membrane potential and conduction velocity were reduced following local myelin retraction injury. In each simulation, 2 parameters were fixed and 1 independent parameter was changed. One micrometer of demyelination on each side of the nodes of Ranvier reduced the membrane potential (a) by less than 7% and conduction velocity (b) by less than 32% of their peak normal values in axons with diameter of 1 μm (green), 2 μm (blue) and 5.7 μm (purple) with demyelinated paranodal regions. In contrast, a 97% reduction in the number of myelin layers in the demyelinated regions (L=1 μm) was needed to reduce the membrane potential (c) and conduction velocities (d) by more than 3% of their peak damaged values. Increasing the number of damaged nodes reduced the conduction velocity (f); while the reduction in membrane potential (e) plateaued after 3 (D= 1 μm) or 4 (D= 2 μm, 5.7 μm) nodes were damaged. Node 10 is at the epicenter of injury and node 15 is outside the damaged region.

extent of injury (number of damaged nodes) had the greatest effect on membrane potential downstream of the injury (node 15) in smaller axons (D=1 μm and 2 μm) (Fig. 3.7 and 3.8) but showed less effect in the larger axon (D=5.7 μm) due to the suppression of signal conduction once three or more nodes were damaged. The combined effect of paranodal and Juxtaparanodal periaxonal resistances explained 52% of variation in membrane potential in node 15 of the larger axon (D=5.7 μm). The rest of variation in membrane potential is due to interaction terms and higher order terms (Fig. 9). Conduction velocities in the 1 μm and 2 μm axons were most sensitive to variations in the paranodal periaxonal resistance (43%, 44%) and the number of damaged nodes (20%, 18%) (Fig. 3.7 and 3.8). In the large axon (D= 5.7 μm), the paranodal periaxonal resistance (28%), juxtaparanodal periaxonal resistance (15%) and number of damaged nodes (14%) were the three parameters most affecting conduction velocity.

Potassium channel blockers

The effect of potassium channel blockers on the recovery of membrane potentials was different between the small (D=1 μm and 2 μm) and large (D=5.7 μm) axon models. Blocking fast potassium channels did not have a significant effect on the recovery of membrane potential when myelin retraction was the source of functional disruption (Fig. 10a). However, applying potassium channel blockers was more effective when axons were damaged by myelin detachment (Fig. 10b). Interestingly, when axons were damaged by both myelin retraction and myelin detachment, potassium channel blockers were more effective (54% and 34% increase in membrane potential compared to pre-treatment values in axons with diameter of 1 μm and 2 μm respectively (Fig. 10c). However, blocking fast potassium channels in the large axon (D=5.7 μm) could not increase membrane potential by more than 2% at the epicenter of injury and action potential propagation was not recovered in distal nodes. Although potassium channel blockers increased the membrane potential in axons with diameter of 1 μm and 2 μm, they did not affect conduction velocity (<5% increase from pre-treatment values).

Injury model validation

The results of our injury model showed similar trends with reported experimental values following mechanical stretch of white matter segments [92,143,145,158,171]. Chronic models of rat spinal cord injury combined with mathematical simulations have indicated that shortened internodes and thinned myelin in the lesion epicenter may reduce membrane potential by 25% in axons with average diameter of 2.3 μm [85]. The results of the current study are similar; 93% myelin detachment in paranodal and juxtaparanodal regions reduced the membrane potential and conduction velocity by 22% and 59%, respectively, in 1 μm axons when damage was localized (7 damaged nodes). The 2 μm axon showed similar behavior with a 25% reduction in membrane potential and a 53% reduction in conduction velocity for

the same amount of myelin detachment. Action potential propagation was never blocked in axons with diameter of 1 μm and 2 μm for the range of myelin retraction studied. In vitro experiments using guinea pig spinal cords showed that applying potassium channel blockers (100 μm 4-AP) increased the membrane potential by 50% over pre-treatment values [92]. Blocking fast potassium channels in our biophysical model increased membrane potential by 54% and 35% in axons with diameters of 1 μm and 2 μm with myelin detachment and myelin retraction respectively (Fig. 3.5a).

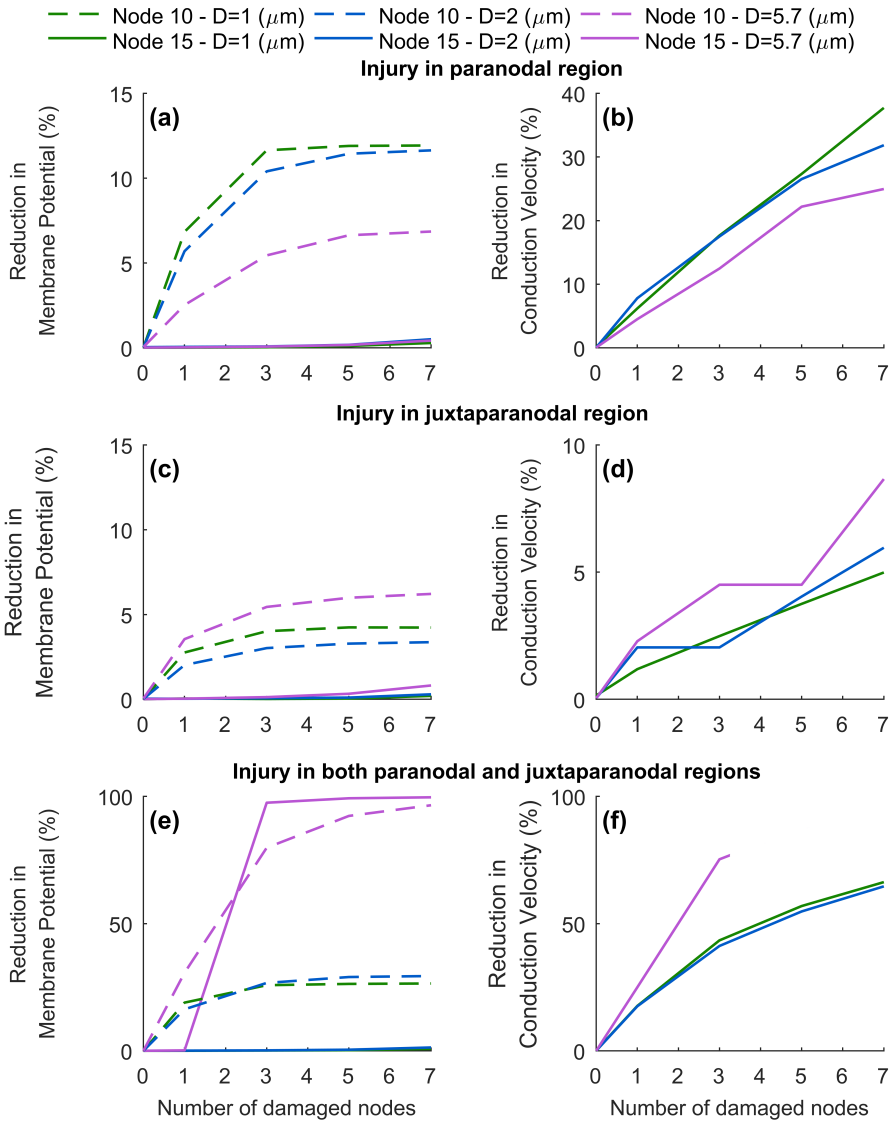

Figure 3.5: Membrane potential and conduction velocity were reduced following an increase in the number of damaged nodes with myelin injury. Reducing the paranodal periaxonal resistance by 99% in 7 nodes reduced the membrane potential (a) and caused reductions in conduction velocity (b) in axons with diameter of 1 μm (green), 2 μm (blue) and 5.7 μm (purple). Reducing the juxtaparanodal resistance by 99% of its normal value in 7 nodes resulted in small reductions (<10%) in the membrane potential (c) and in the conduction velocity (d). Three damaged nodes were enough to block action potential generation in the large axon (D= 5.7 μm) when both paranodal and juxtaparanodal periaxonal resistances were reduced by 99% of their normal values (e). Conduction velocities (f) were reduced or suppressed in all axons when both paranodal and juxtaparanodal periaxonal resistances were reduced by 99% of their normal values.

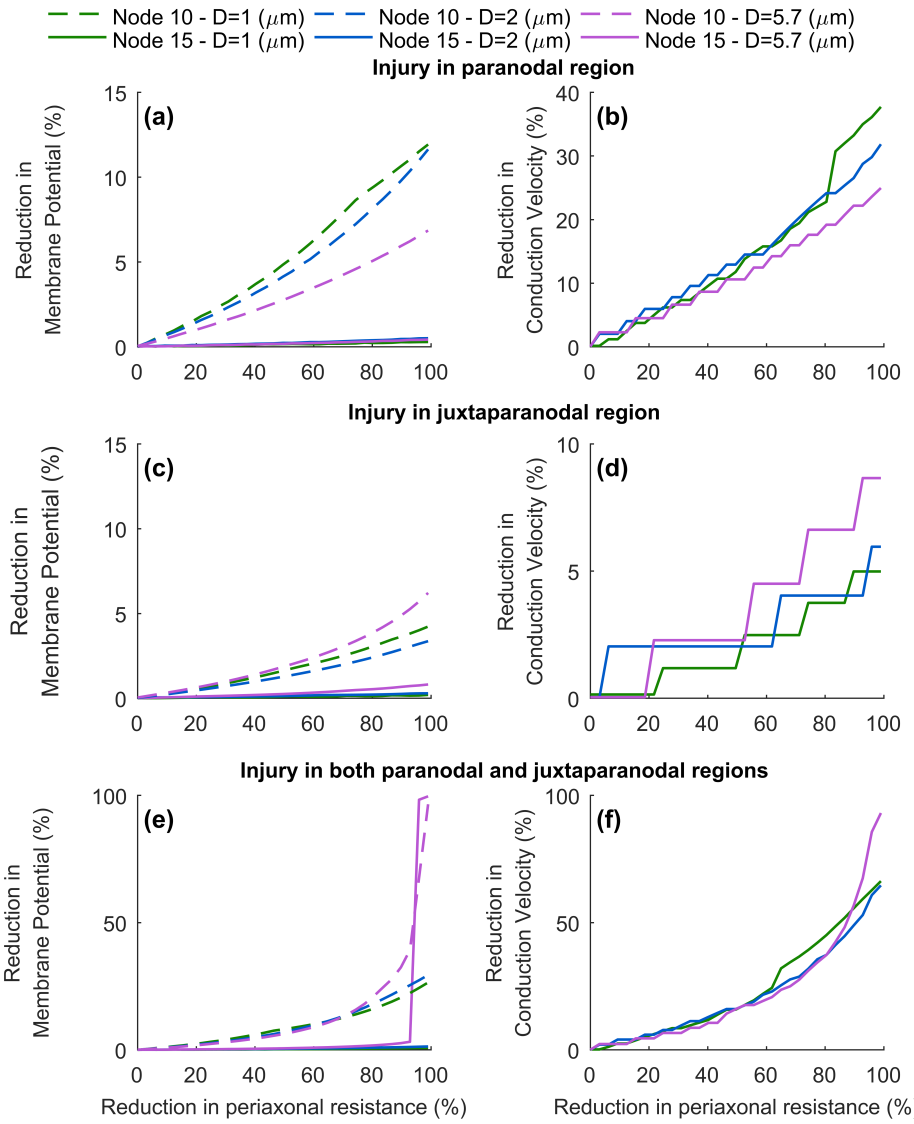

Figure 3.6: Myelin detachment reduces membrane potential and conduction velocity. Damage in the paranodal region had greater effects on membrane potential (a) and conduction velocity (b) than damage in the juxtaparanodal region. Myelin detachment in the juxtaparanodal areas had small effects on c) membrane potential and d) conduction velocity. Damage in both regions resulted in suppression of action potentials in the 5.7 μm but not the smaller axons (e) membrane potential amplitude and f) conduction velocity in axons). Results are shown for axons with diameter of 1 μm (green), 2 μm (blue) and 5.7 μm (purple) when 7 nodes were damaged.

Figure 3.7: The relative effects of different injury parameters on membrane potential and signal propagation on an axon with a diameter of 1 μm. In small axons (D= 1 μm), membrane potential (TP10) is more sensitive to variations of paranodal and juxtaparanodal periaxonal resistances at injury epicenter (Node 10). However, outside the damaged regions (Node 15), membrane potential (TP15) was most affected by the number of damaged nodes in small axons (D= 1 μm). Paranodal periaxonal resistance and number of damaged nodes are the most important parameters in predicting conduction velocity (CV) after injury.

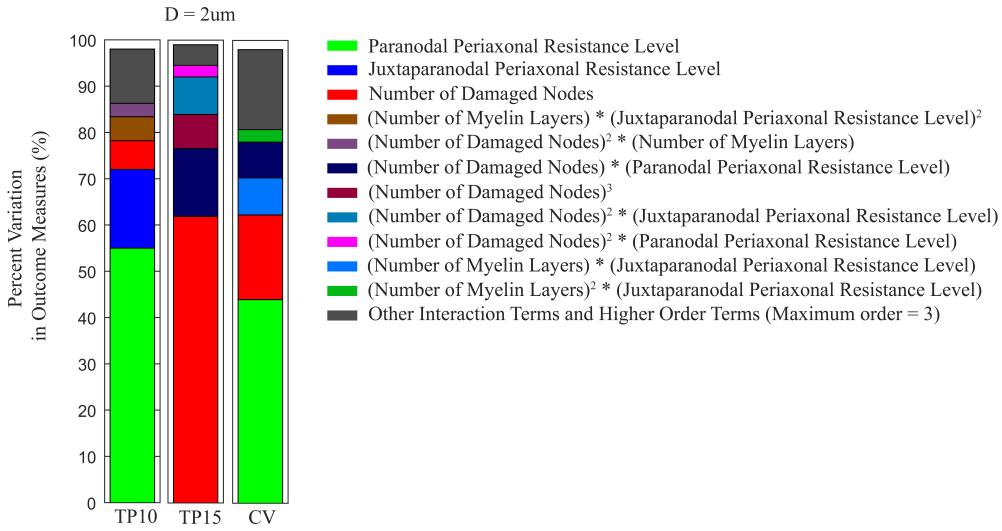

Figure 3.8: The relative effect of different injury parameters on membrane potential and signal propagation in axon with diameter of 2 μm. Paranodal and juxtaparanodal periaxonal resistances are the most important parameters in predicting membrane potential (TP10) at injury epicenter (Node 10). However, outside the damaged regions (Node 15), membrane potential (TP15) is more sensitive to variations of number of damaged nodes and paranodal periaxonal resistance. Similarly, conduction velocity (CV) was most affected by the paranodal periaxonal resistance and number of damaged nodes.

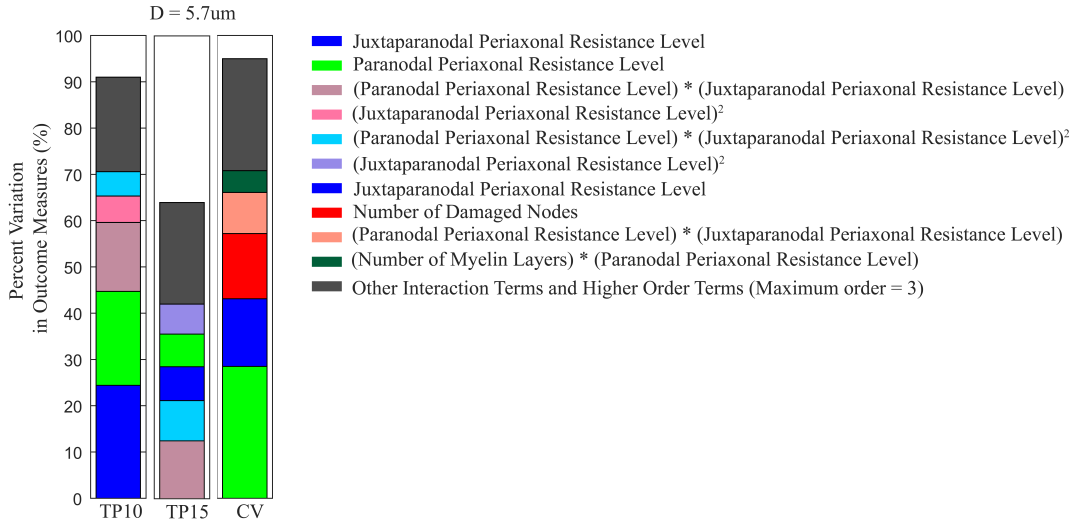

Figure 3.9: The relative effect of different injury parameters on membrane potential and signal propagation in axon with diameter 5.7 μm. Unlike smaller axons (D= 1 μm, 2 μm), injury parameters, their interaction terms, second and third order terms could only explain 91% and 64% of variation in membrane potential TP10 and TP15, respectively. Membrane potential (TP10) is more sensitive to variations of juxtaparanodal periaxonal resistance, paranodal periaxonal resistance and their interaction terms at the epicenter of injury. Similarly, paranodal and juxtaparanodal periaxonal resistances are the most important factors in predicting membrane potential (TP15) outside the damaged regions. Paranodal periaxonal resistance, juxtaparanodal periaxonal resistance and number of damaged nodes explained most of variation in conduction velocity (CV) in the large axon (D= 5.7 μm).

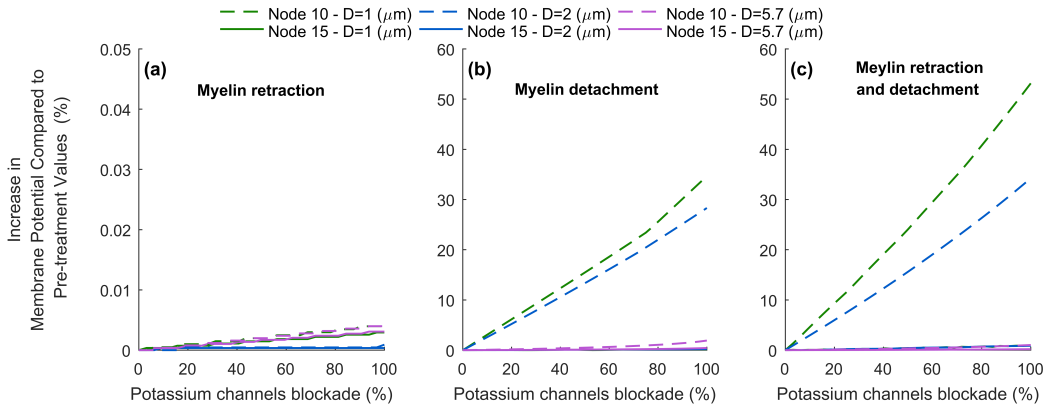

Figure 3.10: Potential effects of blocking fast K+ channels in the juxtaparanodal region on the recovery of membrane potential. Blocking potassium channels in axons with myelin retraction did not increase membrane potential substantially (a). However, blocking fast potassium channels following myelin detachment, increased membrane potential in the axons with diameter of 1 μm, 2 μm, and 5.7 μm to 35%, 28% and 2% from the pre-treatment values, respectively, at injury epicenter (Node 10) (b). Potassium channel blockers were most effective in increasing membrane potential in small axons when axons were damaged by both myelin retraction and myelin detachment (c).

3.5 Discussion

Correlating structural changes in the axon after spinal cord injury to functional disruption is important for understanding the significance of different measures of damage in long-term axonal recovery, studying the biophysical mechanisms of treatments, and identifying potential therapeutic targets to salvage mildly damaged axons from degeneration. However, the value and validity of a computational model depend on the accuracy of the model and the assumed input parameters. We developed a biophysical model that included the normal variation expected in axonal structure because axonal structures are known to affect signal conduction characteristics [32, 130]. In experiments, axonal diameter directly correlated with conduction velocity [130, 131]. The increase in conduction velocity in larger diameter myelinated axons is due to the corresponding increase in internodal length, which is observed to be directly correlated with axonal diameter and the decrease in membrane capacitance due to the myelin sheath around axons [1]. In our study, axonal diameter had the greatest effect (80%) on conduction velocity of the independent variables (the internodal length and the number of myelin layers were defined to be proportional to the axonal diameter and increased when the diameter increased) of all the tested parameters, reinforcing the need to implement a range of axon calibers in computation studies instead of relying on a single generic axon model. In addition, membrane potential was most sensitive to the length of nodal regions. The lengths of the nodes of Ranvier are small compared to the internodal sections. However, nodes contain a high concentration of sodium channels which provide the driving force for generating action potentials and increasing the membrane voltage. The results of our damage study indicated that myelin detachment was the key parameter predicting axonal function after subtle injury for small and large axons. These results also showed that axonal caliber affects the response of axons to the severity and type of myelin injury with larger axons being more affected by damage in the juxtaparanodal regions.

3.5.1 Study Limitations

Our results showed that the electrophysiological and structural properties of axons may have substantial effects on post-injury function. The simulations and modified models used in this study were based on the motor neuron fibers developed by McIntyre and colleagues [98]. However, more geometrically and electrophysiologically accurate models of CNS specific axons could be used to improve the accuracy of predictions in future studies. Currently, measuring many of the axonal parameters is not physically possible therefore a direct quantitative comparison between the results of this study and experiments on damaged axons is not possible. Instead, studying trends and the general behavior of axons after injury may be a more appropriate use for the biophysical models to explain injury-function relationships. The value of our model is in highlighting the structural parameters with the greatest effect on conduction characteristics for axons with varying calibers, which is important for

consolidating experimental observations and also necessary for developing models of neural networks. These models will allow us to combine observations from physiological studies of axonal conduction, and identify and test potential structural targets to improve functional recovery. Although several cellular structures may become damaged following neural tissue injury, the focus of this study was on myelin retraction and myelin detachment in paranodal and juxtaparanodal regions to avoid confounding variable effects masking the biophysiological and pathological processes. For computational efficiency a time step of 0.005 ms was used to complete the calculations for each simulation. In models of axonal damage this time step resulted in a threshold effect that limited the resolution of the simulations to 2-3% of the conduction velocity. The time step used was the same as that used in the original MRG models [98] and was half of those used in other injury simulations [95].

3.5.2 Computational Models of Axonal Function and Damage

Computational models of axonal function and damage provide critical tools for quantifying the relative contributions and interactions of normal structural variations and injury-related structural changes on signal conduction characteristics. Computational models have been developed using a range of methods from linear-nonlinear cascade to biophysical models that directly relate structural changes to function. Recent computational models of axonal injury showed that wide-spread paranodal myelin detachment and retraction in axons with a diameter of 1 µm reduced conduction velocity by 60%, and in more severe cases action potential generation may be blocked, entirely [37]. Experimental results showed a similar 60% reduction in conduction velocity in mild acute axonal white matter injury [92]. The results of the current study are similar; 59% and 53% reduction in conduction velocity, in 1 μm and 2 μm axons respectively, for 93% myelin detachment in paranodal and juxtaparanodal regions. Action potential propagation was never blocked in axons with diameter of 1 μm and 2 μm for the range of myelin retraction studied. Importantly, this study highlights that larger axons do not respond in the same way to demyelinating injuries as the small axons.

Functional electrical stimulation (FES) has been used for treatment of SCI patients for a long time [177, 178]. Neuron level computational models have been coupled with macro level tissue models to predict functional characteristics following electrical stimulation in the spinal cord [179]. Although these models incorporated variation in modeled axonal caliber they did not specifically quantify the effect of structural variations on signal conduction or allow for variations in the electrical parameters of the model. Importantly, extending the application of these coupled finite element and biophysical models to the study of spinal cord injury depends on well-defined biophysical models of axonal damage.

3.5.3 Biophysical Model Results Align With Experimental Observations

Experimentally, it is well accepted that the susceptibility of neurons to mechanical injury may vary due to differences in axonal structures [180]; however, structural variability has largely been ignored in computational studies. The presence of myelin sheaths increases axonal resistance to mechanical trauma over unmyelinated axons [81]. However, the relationship between axonal structure and injury has not been clearly defined. Experiments in brain tissue report that smaller axons are more vulnerable to trauma than large axons [81, 82], while experiments in isolated tissue did not find a strong correlation between axonal diameter and injury [145, 171, 181]. In spinal cord injury models, large axons appear more susceptible to injury than small axons [83–86]. These results highlight the challenges in studying axon injury mechanisms and the critical need to develop biophysical models that represent a broad range of axonal structures, as their response to injury and treatment may vary. In our model, different caliber axons responded to myelin retraction and detachment differently. Myelin detachment in the paranodal area had a greater effect on membrane potential in smaller axons (D= 1 μm and 2 μm) while detachment in the juxtaparanodal area had larger effect on the large axon's (D= 5.7 μm) membrane potential at both the epicenter of injury and distal nodes (Node 15). Although conduction velocity was less sensitive to juxtaparanodal myelin detachment than paranodal myelin detachment in all axons, juxtaparanodal myelin detachment had a sizable effect on conduction velocity in the largest axon (D= 5.7 μm). It is worth noting that the amount of myelin detachment in the paranodal and juxtaparanodal regions does not have a linear relationship with the reductions in conduction velocity and membrane potential. Our results show that when only 3 nodes are affected, even severe paranodal or juxtaparanodal myelin detachment cannot individually reduce membrane potential by more than 1% outside of injured areas.

Previous research indicates that increasing the number of myelin layers around axons increases conduction velocity [182]. Computational modeling has shown that the observed increase in conduction velocity plateaus when axons (D=1 μm) are covered by about 10 myelin lamellae [182]. Therefore, conduction velocity is more sensitive to the number of myelin lamellae when an axon is covered with only few numbers of myelin layers. Reduction in the thickness of myelin in the internodal areas induces a reduction in conduction velocity in axons with an average diameter of 2.3 μm [85]. Similarly, the results of our study suggest that number of myelin layers is an important factor in predicting membrane potential and conduction velocity (Fig. 3.7, 3.8 and 3.9) in all axon calibers. However, in subtle paranodal injury only a substantial reduction in the number of myelin layers has a significant effect on conduction velocity (Fig. 3.4d). Our results indicate that for a localized subtle injury (1 μm of the paranodal regions on either side of the nodes of Ranvier are demyelinated) conduction velocity drops significantly (24%-32%) which may affect sensory and motor functions of large animals [183] including humans. These results highlight the importance

of accurately modeling the myelin structure in the paranodal regions, which are adjacent to highly sensitive nodal areas as compared to internodal regions.

Although the application of potassium channel blockers in animal models of SCI has shown some promise [167,184], human trials resulted in inconclusive results [185–187]. Axon location and the mechanism of effect may partially explain why the application of these blockers shows variable results. Recent ex vivo studies showed that both 4-Aminopyridine (4-AP) and 4-aminopyridine-3-methanol (4-AP-3-MeOH), which are known as fast potassium channel blockers, enhanced impulse conduction following traumatic spinal cord injury or demyelinating disease [158,188]. In vitro experiments using guinea pig spinal cords showed that applying 100 μM 4-AP increased the membrane potential by 50% over pre-treatment values [92]. Interestingly, previous research showed that the ventral white matter of the guinea pig spinal cord contains 100 times more small axons (D=1 μm -2 μm) than large axons (D=9 μm-10 μm) [157]. The results of the current study indicate that blocking fast potassium channels increases membrane potential in axons with diameters of 1 μm and 2 μm with myelin detachment and myelin retraction (Fig. 5a), but does not significantly improve membrane potential in the large axon (D= 5.7 μm). Sun and colleagues observed no effect of axonal caliber on the response to the application of 4-AP-3-MeOH [158]. However, this was concluded based on the responsiveness of whole spinal cord white matter sections to variations in stimulus, not by direct observation [158]. Experiments by Devaux and colleagues [137], which grouped axonal behaviour into three approximate diameters (D=0.7 μm, 1.2 μm and 2.1 μm) and directly observed variations in axonal scale on conduction characteristics, indicated that small axons got the most benefit from 4-AP and dendrotoxin-1 (DTX). It should be noted that 4-AP is a broad-spectrum potassium channel blocker [143,164] and beneficial applications of these treatments might be due to effects of this blocker on other potassium channels or neuronal structures. In vitro and in vivo studies suggest that the application of a clinical dosage of 4-AP did not have a consistent effect on spinal cord injury patients and demyelinated axons [185, 186, 189, 190]. It was an effective treatment for potentiating synaptic transmission and increasing muscle twitch tension which may be very important in mediating the beneficial effects of 4-AP in demyelinating diseases such as multiple sclerosis [164, 189]. More recent studies suggest that 4-AP may have neuroregenerative effects and promote remyelination in peripheral nerve injury in mice [191]. Ultrastructural analysis of damaged sciatic nerve in mice have shown that localized 4-AP treatment increases the axonal area and myelin thickness following injury and enhanced both the speed and extent of restoration of normal conduction velocity [191]. Moreover, the results of this study show how sensitive the amount of signal recovery is to the type of injury. For example, although potassium channel blockers were not very effective in signal recovery when axons were damaged with only myelin retraction, the effect of these blockers on axons with both myelin retraction and detachment was significant (Fig. 3.10). Further studies should highlight the relationship between type of injury, axonal morphol-

ogy and the application of potassium channel blockers to maximize the action potential recovery. In addition, the results of our study emphasize that changes in axonal conduction resulting from myelin retraction and detachment are not exclusively due to fast potassium channel exposure. Therefore, coupling potassium channel blockers with other treatments that address the effects of myelin retraction and detachment may be more effective.

3.6 Conclusion

In this study, we have established the significant contribution of structural variations on axonal function both in healthy and damaged axons. Our model was based on a previously well studied and validated model of mammalian axons [98,138,140] which is used for several clinical applications such as brain and spinal cord stimulation [179, 192]. Our new model can incorporate other cellular structures with high spatial accuracy in sections of interest for axons with different calibers. Our results showed that myelin detachment had a greater effect on functional disruption following axonal injury than myelin retraction in all axons; however, the amount of functional disruption was highly dependent on axonal caliber. The model demonstrated that blocking fast potassium channels is more effective in small axons for recovering signal amplitude than in large axons. Due the complexity and difficulty of performing controlled mechanical injury and electrophysiological recording at the axonal level, the available literature is very limited. The results of this study motivate the need for further controlled laboratory experiments that quantify changes in axonal structure and functional outcomes. Advanced technologies such as optical tweezers [193], coherent anti-Stokes Raman scattering (CARS) [194], and stretchable microelectrode arrays [195] may help in generating an injury, imaging the injury, and recording electrical signals at the axonal level, respectively.

Computational models are becoming increasingly important in preliminary studies of spinal cord injury pathophysiology [196] and treatment [179, 197]. These models will aid in designing animal and laboratory experiments. Incorporating structural variability in these computation models is important for highlighting sources of experimental variability and identifying potential challenges in translating from small scale animal models (e.g. mice or rats) to larger animal models (e.g. pig, dog or non-human primate) and human subjects early in a study.

Chapter 4

Quantifying the Effect of a Sectioning Method for Increasing Geometrical Resolution on Computational Cost for Axons Modeled in NEURON

4.1 Abstract

Computational models help to increase our understanding of the injury mechanism in axons and neural networks. NEURON is a commonly used simulation software for modeling morphological and electrophysiological properties of axons separately. However, to simulate some abnormalities, high geometrical resolution is required in the model. High geometrical resolution is achieved by increasing the number of segments in each section of the NEURON model. This results in higher computational cost and slows down simulations in large networks of axons or repeated simulations. Uniform segmentation also complicates the consistency of comparisons of simulation results across axons of different caliber. In this paper, we assessed an alternative approach that separates geometrical resolution from computational cost by allowing sections to be subdivided in the model non-uniformly, by introducing subsections of the same structure. To determine the computational accuracy and cost of this approach, we compared the results of the McIntyre model of myelinated axon and Sundt model of unmyelinated axon with our modified models. The results indicate that the proposed approach is a viable option for increasing geometrical resolution with reduced computational resources while keeping the maximum error of action potential amplitude and velocity at less than 1% (using type I models) compared to the original models. The modified models may reduce the simulation time by up to 98% for fine geometrical resolutions (0.125μm). This approach makes comparisons of simulation results amongst different

axons more consistent and facilitates model conceptualization by making the translation of experimental observations to computational simulations more intuitive.

4.2 Introduction

Neuronal abnormalities from injury or disease, such as the loss of myelin sheaths, spheroid formation, and breakage of microtubules may extend over small or large regions of specific axonal structures [198, 199]. Computational models provide a mechanism to simultaneously study the array of structural and electrophysiological changes and to quantify their relative effects on action potential propagation. NEURON [200] is a popular simulation software that facilitates creating different axonal structures and defining their morphological and electrophysiological properties separately. Each neuronal structure in NEURON is defined with a cylindrical-shaped section which itself is divided into one or more equal length compartments which are referred to as segments.

In developing NEURON models, spatial resolution and geometrical resolution are two highly interdependent concepts that need to be considered together and usually they have the same value in neuron models. In a given NEURON model, in order to accurately reproduce neuronal transient signals that are derived from passive and active channels, the spatial resolution of the model should be increased, and the length of each compartment should be a fraction of the length constant at the frequencies of interest. The spatial resolution can be increased by increasing the number of segments in each section and therefore reducing the length of each compartment. However, the more segments a model has, the more computationally expensive the simulations will be. Finding the right number of compartments and their length to achieve the desired spatial accuracy in a model has been a research question for a long time for the computational neuroscience community [201]. In NEURON, Ted Carnavale and Hines introduced a solution for unmyelinated structures to determine the right value for each compartment length which is generally referred to as the d_lambda rule. However, the original form of this tool cannot be used for all NEURON models as it was developed for unmyelinated axons and additional considerations need to be taken when myelinated axons are being studied in NEURON which is beyond the scope of this paper. On the other hand, to study fine neuronal structures such as pieces of dendrites [202] or to simulate small and subtle neuronal injuries that are extended over multiple regions of an axon such as post trauma paranodal myelin retraction [201, 203–205] or spheroid formation, specific control over the precise, submicron morphology of the axon is required. NEURON provides a method to alter and assign electrophysiological and morphological properties within a section using the normalized position ($0 \leq x \leq 1$, in which $x = 1$ corresponds to the absolute section's length). However, this method is limited by the number of segments (Nseg) in the section as electrophysiological and morphological properties are invariant along the length of each segment [200].Therefore, similar to spatial resolution,

when a fine geometrical resolution is needed, then the number of segments increases which results in a higher computational cost that slows down the simulation of individual neurons or their network behaviour. A potential alternative solution is to increase the number of segments locally to achieve the desired geometrical resolution where injury is being simulated. Although this method does not increase the computational cost compared with increasing the number of segments across all axonal sections, it reduces the consistency between different models. This issue becomes exacerbated when different caliber axons, in which the same axonal structure (ex. paranodal and juxtaparanodal regions, etc.) may have different lengths depending on the axonal caliber, are simulated in the same study and each simulation may end up having different numbers of segments and spatial resolution. In addition, simulation software programs like NEURON may limit the number of segments that can be defined in axonal structure. For example, the maximum number of segments in a NEURON section is 32,766 which might not be enough to achieve fine geometrical resolution (e.g. < 0.2 μm) in long neuronal structures and at the same time be unnecessarily too many for other short structures in the same model. Moreover, in case of simulating abnormalities, having a dependency between the number of segments and injury length makes the model conceptualization difficult particularly when one is translating experimental observations to computational simulations.

In this paper, we are assessing a new approach using NEURON's conventional tools for implementing axonal models which separates geometrical resolution from computational power and spatial resolution in regions of interest. Our assessments are done on the commonly used McIntyre model of myelinated motor neurons [206] and an unmyelinated model of sensory neurons developed by Sundt and colleagues [207] in NEURON but can apply more broadly to any NEURON implementation.

4.3 Method

Several models of single neurons have been developed to simulate action potential generation and signal transfer along neuronal cells. In this paper we used two publicly available models of myelinated and unmyelinated neurons to study the effectiveness of the proposed approach in increasing geometrical resolution while reducing computational cost. The model of a myelinated axon developed by McIntyre et al. [206] using the NEURON environment has been used for various applications such as deep brain stimulation and transcutaneous spinal cord stimulation [208, 209]. Although the model was initially developed based on morphological data from cats with fiber diameters ranging from 5.7 to 16.0 μm, it has been used to study abnormalities and treatment methods in humans with different axon calibers [210–212]. On the other hand, a non-specific model of unmyelinated dorsal root ganglion (DRG) neurons was developed by Sundt et al. [207] in NEURON that was used to study nociceptive transmission [213] and stimulation in pain suppression [214]. Both models'

Table 4.1: The Original Sundt And McIntyre (D=5.7μm) Models' Information: Section Names, Length And Number of Segments in The Original Models.

Model	**Section Name**						**Total Sections**	**Total Segments**
McIntyre	NODE	PARA	JUXTA	INTRA				
# of Sections	21	40	40	140[1]				
Length (μm)	1	3	35	60.43			241	241
# of Segments	1	1	1	1				
Sundt	SOMA	STEM	TJ_PERI	TJ_CENT	CENT	PERI		
# of Sections	1	1	1	1	1	1		
Length (μm)	25	75	100	100	5000	5000	6	600
# of Segments	100	100	100	100	100	100		

1 This is based on having a seventh INTRA section in the internodal region of the McIntyre model as described in the method section.

files (obtained from ModelDB [215]) were converted to a Python script to facilitate easier parameter control and more efficient computational processing to simulate axons with diameter of 1 μm, 2 μm, and 5.7 μm [204] in the McIntyre model and 0.4 μm in the Sundt model [207].

Briefly, the McIntyre model is composed of 10 different sections between each neighbouring node of Ranvier: two myelin attached sections (PARA), two main juxtaparanodal sections (JUXTA) and six stereotyped internodal sections (INTRA) (Fig. 4.1a, 4.1b). Three active channels (fast and persistent sodium, and slow potassium) are in the nodal areas that help in generating action potential and modeled using modified Hodgkin-Huxley based equations. The axonal membrane in the juxtaparanodal regions is covered by fast potassium channels [206]. On the other hand, the Sundt model is composed of a soma section (SOMA), a stem axon section (STEM), a central axon section (CENT), a peripheral axon section (PERI), Tjunction Central (TJ_CENT) and Tjunction_Peripheral axonal (TJ_PERI) sections (that connect the central and peripheral axons to the stem axon) (See Fig. 4.2a). All sections of the original Sundt model have 100 segments except the SOMA (Nseg=1). In order to compare the computational costs and geometrical resolutions in our simulations more consistently, we also set the number of segments in the SOMA to be 100 (see Table 4.1). In our simulations, the original files were used to compare the computational cost of using the McIntyre and Sundt models with the modified models using our approach which is described below. However, the internodal region in the McIntyre model is composed of six INTRA sections (Fig. 4.1b). In order to simulate symmetric and asymmetric abnormalities in the internodal region better, a seventh INTRA section was inserted in the internodal region while keeping the total region length constant (Fig. 4.1c). A summary of available structures in each model, its length and the number of segments is provided in Table 1.

The geometrical resolution and computational accuracy of NEURON models depend on the number of segments used [200, 216]. Increasing the number of segments, increases the computational costs and slows down the simulations. Our approach for separating geometri-

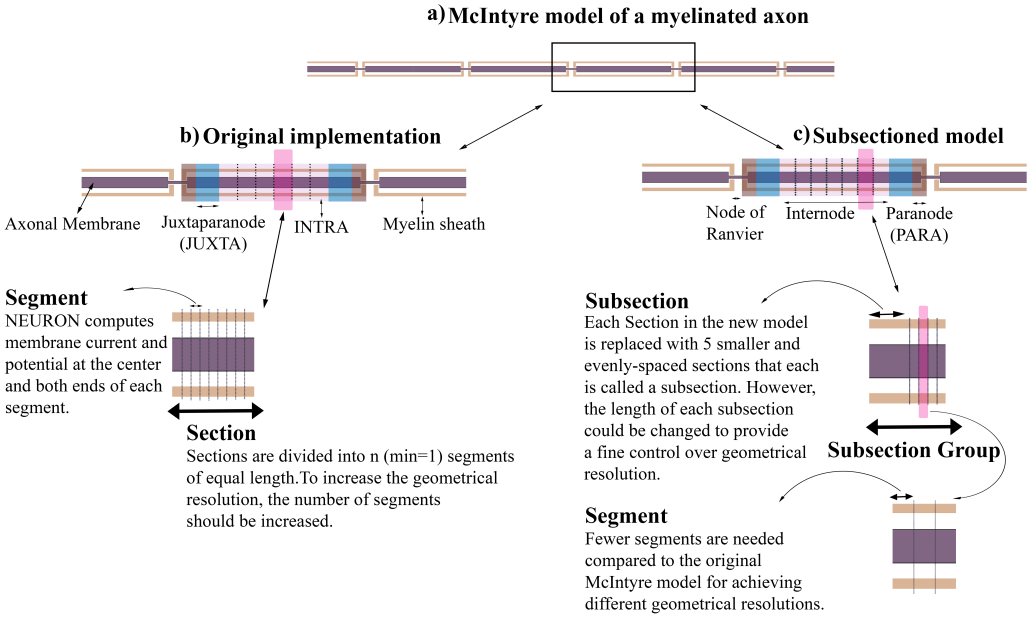

Figure 4.1: (a). An illustration of McIntyre myelinated axon in NEURON. (b). McIntyre model is composed of 10 different sections between each neighbouring node: two myelin attached sections (PARA), two main juxtaparanodal sections (JUXTA) and six stereotyped internodal sections (INTRA). By default, each section in McIntyre model is composed of only one segment however, the number of segments should be increased to achieve the desired geometrical resolution. (c). The subsectioned model is similar to the original McIntyre model except that each section is subdivided into five shorter subsections that form a subsection group. The length of each subsection can be changed continuously, and subsections do not need to be of equal length which gives finer control over geometrical resolution.

cal resolution from computational segments was to split the NEURON sections representing each structure (Ex. Node, PARA, JUXTA, INTRA in McIntyre model or SOMA, STEM, TJ_PERI, TJ_CENT, CENT, PERI in Sundt model) of the original model into five NEURON sections in the modified model which could vary in length while the total length of the structure remained constant (Fig. 4.1c and 4.2c). We call each of these shorter NEURON sections a subsection. Therefore, each section of the original model will be represented by a Subsection Group (Fig. 4.1c and 4.2c) that includes 5 subsections. Having five subsections with definable geometry per structure provides the ability to simulate axonal changes, injury or disease effects in one or more subsections and change the length of the damaged regions continuously as opposed to discrete amounts (where geometrical resolution = total length of a section / number of segments). However, there are two different options for choosing the number of segments in the subsectioned models (Nseg'). The first option (Type I models) is to keep the overall number of segments and compartments in both models the same. Therefore, the number of segments in the subsectioned models (Nseg') should be set to be

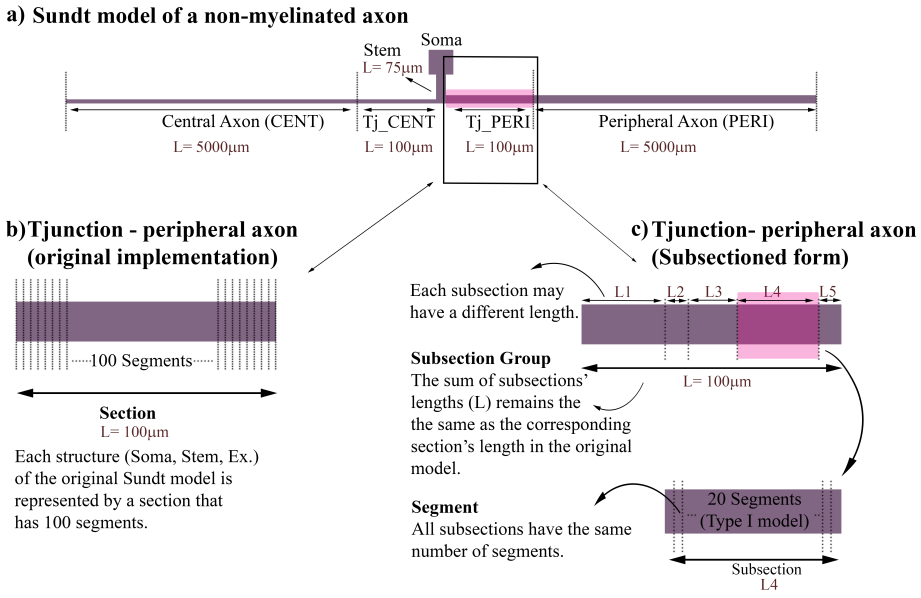

Figure 4.2: (a). An illustration of Sundt model of unmyelinated axon in NEURON. Sundt model is composed of a soma section, a stem axon section, a central axon section, a peripheral axon section, Tjunction-central and Tjunction_peripheral axonal sections. (b). Each structure of the original Sundt model is represented by an unmyelinated section that has 100 segments (c). Each structure of the original model is subdivided to five subsections that form a subsection group. The length of each subsection can be changed continuously, and subsections do not need to be of equal length which gives finer control over geometrical resolution.

Table 4.2: Study Parameters And Values For the Subsectioned McIntyre and Sundt models.

Model and Parameters	**Parameter Value**
Subsectioned McIntyre	
(D=1 μm, 2 μm and 5.7 μm)	
Structure of Interest	NODE, PARA, JUXTA, INTRA
Position of Short Subsection	SubSection_1, SubSection_2, SubSection_3, SubSection_4, SubSection_5
# of Affected Subsections	1, 3, 5, 7
Percent Length of Subsection	0.001%, 5%, 10%, 15%, 20%
# Of Segments	3 (Type I model), 15 (Type II model)
Subsectioned Sundt	
(D= 0.4 μm)	
Structure of Interest	SOMA, STEM, TJ_PERI, TJ_CENT, CENT, PERI
Position of Short Subsection	SubSection_1, SubSection_2, SubSection_3, SubSection_4, SubSection_5
# of Affected Subsections	1
Percent Length of Subsection	0.001%, 5%, 10%, 15%, 20%
# Of Segments	20 (Type I model), 100 (Type II model)

one fifth the number of segments in the original models (Nseg) because each structure of the original models was subdivided into five subsections in the modified models. However, the local spatial accuracy of these models (Type I models) may change when the lengths of individual subsections change in a subsection group (Fig. 4.1c). In this case, there might be one or more subsections that their lengths are longer than 0.2 of the subsection group's total length (or corresponding section's length) (See Fig. 4.1c) and hence the number of segments per unit length of the subsection decreases. Therefore, these models may not always meet the requirements determined by d_lambda rule or similar approaches for guaranteeing spatial accuracy. However, the second option (Type II models) is to set the number of segments in the subsectioned models (Nseg') the same as the number of segments (Nseg) in the original models. In this case, the spatial accuracy of the subsectioned models is always guaranteed in all simulations however, the computational cost of running the simulations will increase substantially.

In order to compare the computational accuracy and results of the subsectioned models with the original models, it is necessary to find the stable state and the ground truth signal for each of the McIntyre and Sundt models. However, the Sundt model of unmyelinated neurons was originally developed based on the d_lambda rule in NEURON [207]. The shortest length constant at 100 Hz (λ100) for the Sundt model is 178.41μm [207] and the default value of d_lambda in NEURON is 0.3 which is recommended for most of the simulations [200]. Since each section of the Sundt model has 100 segments [207], the maximum length of a compartment in this model is 50μm which is less than 53.52μm (=178.41μm * 0.3) recommended by the d_lambda rule. Therefore, the model parameters that were recommended by the original study [207] were used for further analysis and comparisons with the subsectioned models' results. However, since the original d_lambda formula was developed for unmyelinated axons, it is necessary to find the ground truth for the McIntyre

model. This was done by increasing the number of segments (Nseg) and comparing the results at each stage until the response for the models stabilized. Therefore, the number of segments in all sections of the McIntyre model was increased from 1 to 35 by a series of odd values (n=1, 5, 15, 25, 35) to keep the middle point of each segment. This ensured signal recordings were always at the same location. Action potential signals were recorded from node 5 (V1) and node 10 (V2) of the axon. V1 and V2 signals corresponding with each Nseg value were compared with the same signal when an increased Nseg value was used (e.g. 1→5, 5→15, etc.) by calculating the root mean square error (RMSE) values. The model outputs were considered stable when the difference in total root mean square error (=RMSE for V1 + RMSE for V2) of the action potential signals in two consecutive simulations was $\leq$ 1 mV. After finding the ground truth models, two separate computational studies were performed for each of the McIntyre and Sundt models in order to validate the stability of the different subsectioned models (Type I and Type II) and to quantify the accuracy of action potential calculations particularly when the length of one subsection is orders of magnitude shorter than the other subsections. The five independent input parameters that were included in the study are shown in Table 4.2. The Percent Length of Subsection (PLS) value determined the length of the subsection based on the total length of the corresponding structure (Node, PARA, JUXTA, INTRA in McIntyre model and SOMA, STEM, TJ_PERI, TJ_CENT, CENT, PERI in Sundt model). In order to find the limits of the model and assess the stability of the subsectioned models within a range of physiologically relevant values, the lower and upper bounds of PLS were set to 0.001% and 20%, respectively. The number of Affected Subsections (NAS) determined how many axonal structures have at least one subsection with its length less than 20 percent of the corresponding section's length. However, since there is only one object of each of the axonal structures (SOMA, STEM, TJ_PERI, TJ_CENT, CENT, PERI) in the Sundt model, this value was kept at 1 for all simulations. As a result, 800 simulations were executed for each of the subsectioned McIntyre models (D=1μm, 2μm, 5.7μm). Similarly, 200 simulations were run for the subsectioned Sundt models (D=0.4μm). The number of segments (Nseg') were 3 and 15 for type I and II subsectioned McIntyre models, respectively. Similarly, the type I subsectioned Sundt model had 20 and the type II subsectioned Sundt model had 100 segments (Nseg').

In a separate set of simulations, to compare the computational cost of running the original and subsectioned versions of the McIntyre and Sundt models we adjusted the model parameters (number of segments per structure) for each of the original models and executed the simulations to match specific geometrical resolutions. For the McIntyre model (D=1μm, 2μm, 5.7μm), the target geometrical resolutions were 1μm, 0.5μm, 0.25μm and 0.125μm. However, the lengths of the central and peripheral axons in the Sundt model (D=0.4μm) are 5000μm. Since the maximum allowed number of segments in a NEURON section is 32766, it was not possible to achieve the geometrical resolution of 0.125μm in the Sundt model using the conventional approach. The maximum geometrical resolution in the original

Sundt model is 0.15μm by increasing the number of segments to 32,766 and not changing the structure of the original model. In all simulations, the number of segments was the same along each axonal model. Both the subsectioned (type I and II) and original models were run 3 times for each geometrical resolution value (to take into account the background operating system activities) and the averaged run-time values were used for comparison.

In all simulations, an intracellular current stimulus of 2nA for 0.1mS was applied to the axon to locally depolarize the stimulation point and initiate the action potential [206]. In the McIntyre models, the stimulation point was in the center of node 1 of the axon and in the Sundt model the stimulation point was at x=0.9 (normalized position) of the peripheral axon. The axons were implemented as finite length neurites. In the McIntyre models, nodes 5 and 15 were chosen for recording action potential amplitude and conduction velocity to avoid sealed-end effects [201]. In the Sundt models, the recordings were done in the center of peripheral and central axons. In order to compare the simulation results and runtimes consistently, a fixed time step of 0.005 ms was used for all calculations.

4.4 Results

The number of segments (1, 5, 15, 25, 35) in the McIntyre model demonstrated that the McIntyre model became stable and action potential amplitude and velocity absolute values converged when Nseg $\geq$ 15 (RMSE $\leq$ 1 mV) (Fig. 4.3). Accordingly, the outputs of the McIntyre model with Nseg=15 were considered as the ground truth (Fig. 4.3d). The total RMSE values when comparing the outputs of the original McIntyre model for when Nseg =1 and Nseg=15 (1 $\rightarrow$ 15) are 28.23 mV, 21.66 mV and 27.28 mV for the axons with the diameter of 1μm, 2μm and 5μm, respectively. To match the total number of segments in each section, Nseg$'$ = (Nseg/5) was used in simulations using type I subsectioned McIntyre models. The Nseg' value was set to be 15 in type II subsectioned McIntyre models. Our results (Fig. 4.4a, c, e, g) show that the outputs of the type I subsectioned McIntyre and Sundt models match (RMSE = 0 mV) with the original models when the subsections were evenly distributed. The results of type II subsectioned McIntyre models (Fig. 4.4b, d, f) are also consistent with the original models but the error rates are slightly more (RMSE $\leq$ 2 mV) than type I. However, the conduction velocity in the type II subsectioned Sundt model of unmyelinated axons was changed and the amount of total RMSE (15.498 mV) was substantially increased (Fig. 4h).

The results of the computational study indicate that both types I and type II subsectioned McIntyre models of myelinated axons are stable and the amounts of variability in action potential amplitudes and velocity are small. In order to quantify this variability, the total RMSE values (deviation from the ground truth models) for all 800 simulations of subsectioned McIntyre models were calculated (Table 4.3). The maximum total RMSE values were 1.880455 mV, 1.213116 mV and 1.818676 mV for subsectioned McIntyre models with

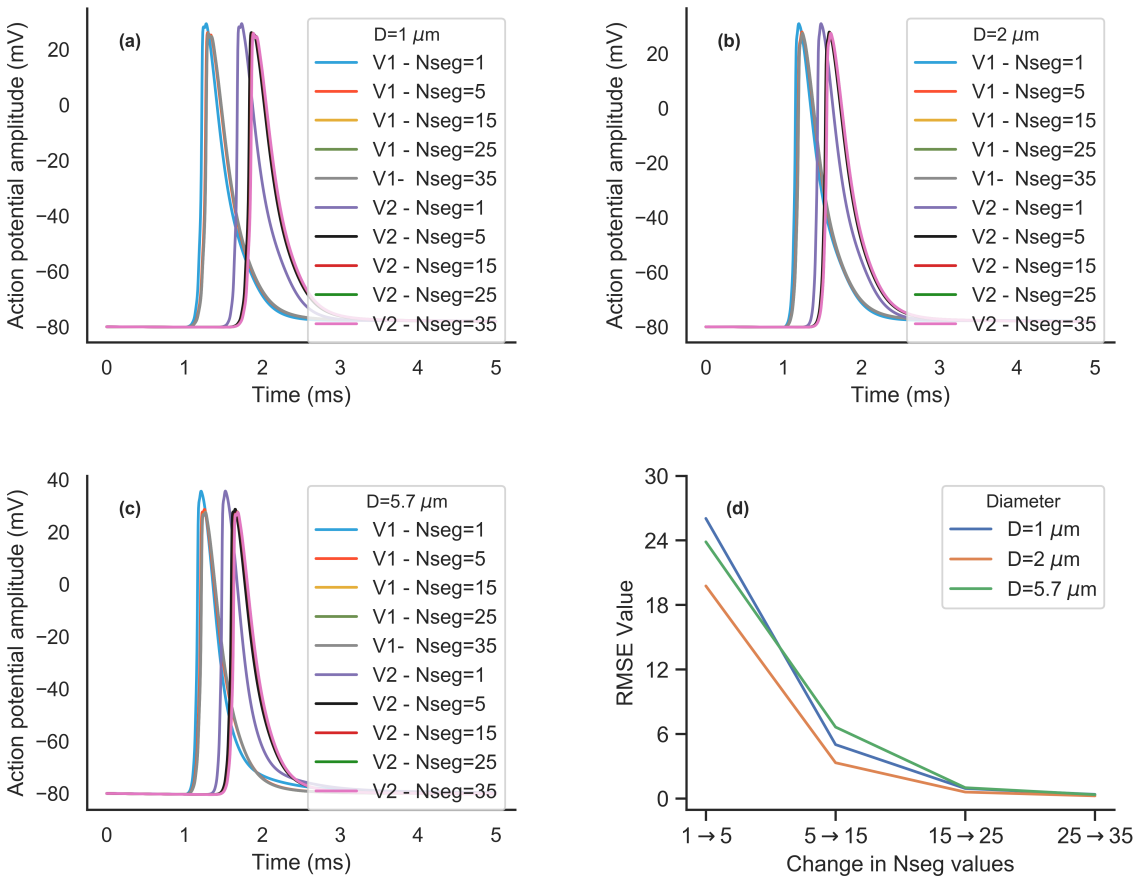

Figure 4.3: A comparison of action potential signals (V1 recorded from node 5 and V2 recorded from node 15) of McIntyre model when the number of segments (Nseg) were changed from 1 to 35 for axons with the diameter of 1 μm (a), 2 μm (b) and 5.7 μm (c). d) shows that the total RMSE value (RMSE for V1 + RMSE for V2) of the difference between two consecutive simulations for different Nseg values becomes ≤ 1 for all axons when there are 15 segments in all sections of the McIntyre model.

Table 4.3: RMSE Values (mV) For Type I and II of Subsectioned McIntyre and Sundt Models

Diameter	Nseg'	Count	Mean	Std	Min	25%	50%	75%	Max
Sundt D=0.4 μm	20	400	0.00003	4.19E-05	6.47E-13	2.44E-08	0.000009	0.000042	0.000206
	100	400	15.49774	3.99E-08	1.55E+01	1.55E+01	15.49774	15.49774	15.49774
McIntyre D=1.0 μm	3	400	0.017137	0.043519	1.64E-11	9.73E-08	0.000528	0.005415	0.288
	15	400	1.824911	0.009126	1.79E+00	1.82E+00	1.824946	1.824947	1.880455
McIntyreD=2.0 μm	3	400	0.010673	0.027077	1.36E-11	7.71E-08	0.000351	0.003225	0.179465
	15	400	1.177966	0.005766	1.15E+00	1.18E+00	1.177988	1.177988	1.213116
McIntyreD=5.7 μm	3	400	0.014439	0.027919	1.99E-11	2.90E-08	0.000437	0.015587	0.176749
	15	400	1.784028	0.005693	1.76E+00	1.78E+00	1.784176	1.784176	1.818676

the diameter of 1μm, 2μm and 5μm, respectively (See Fig. 5a, b, c, d, e, f). The standard deviation for peak action potential amplitudes (V1 and V2) and velocities for type I and type II subsectioned McIntyre models (D=1μm, 2μm and 5μm) were less than 0.01 mV and

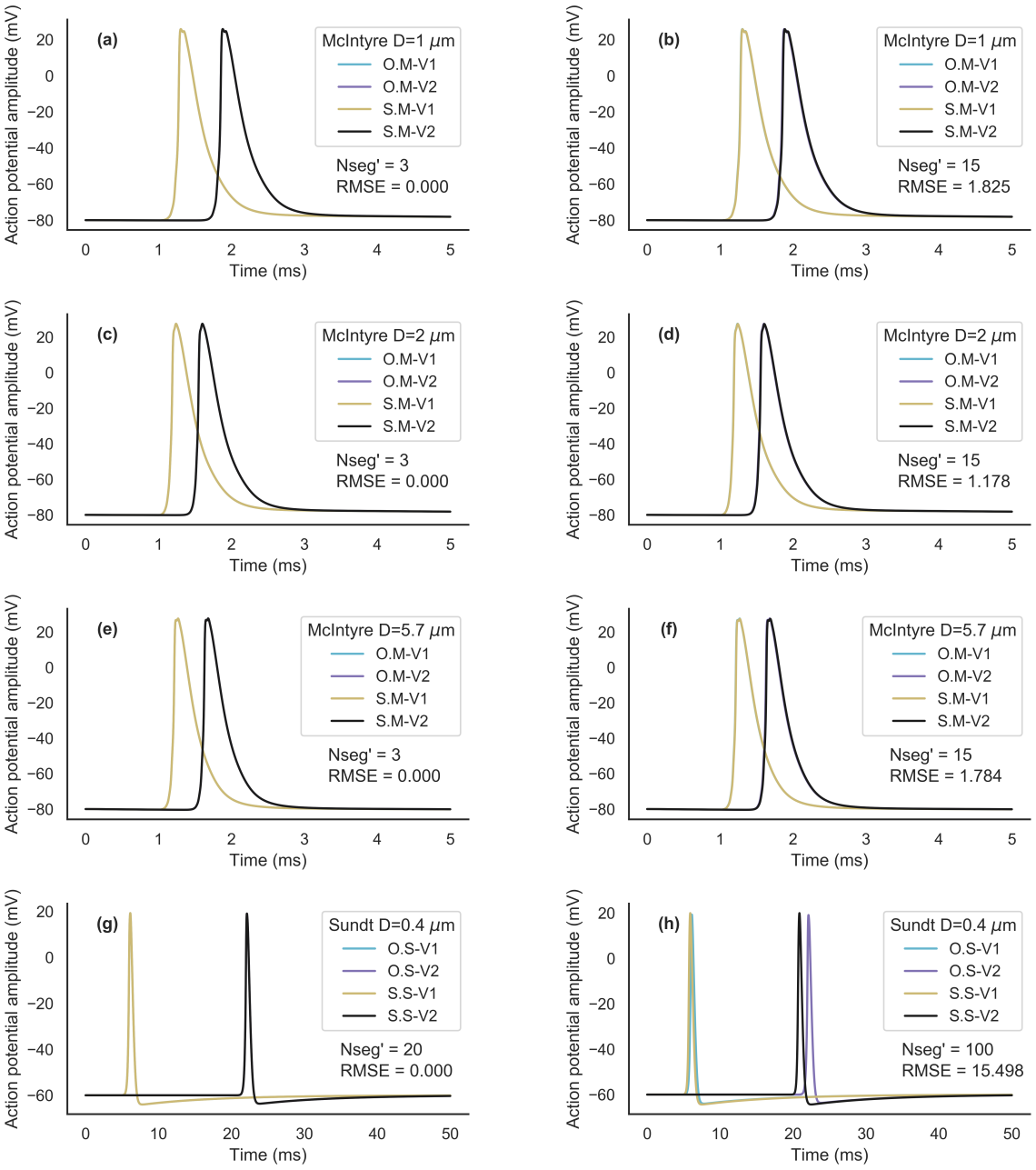

Figure 4.4: A comparison of action potential signals of type I and II subsectioned models of McIntyre (D = 1μm, 2μm and 5.7μm) and Sundt models (D = 0.4μm) with the original model outputs when all subsections are equally distributed. The RMSE value for type I models (left) that has the same number of total segments as the original models is zero millivolts. Although the outputs of the type II subsectioned McIntyre models (b, d, and f) match with the original models (RMSE <2 mV), the type II subsectioned Sundt model (h) generates more error (RMSE=15.496 mV). O.M = Original McIntyre model. S.M = Subsectioned McIntyre model. O.S = Original Sundt model. S.S = Subsectioned Sundt model.

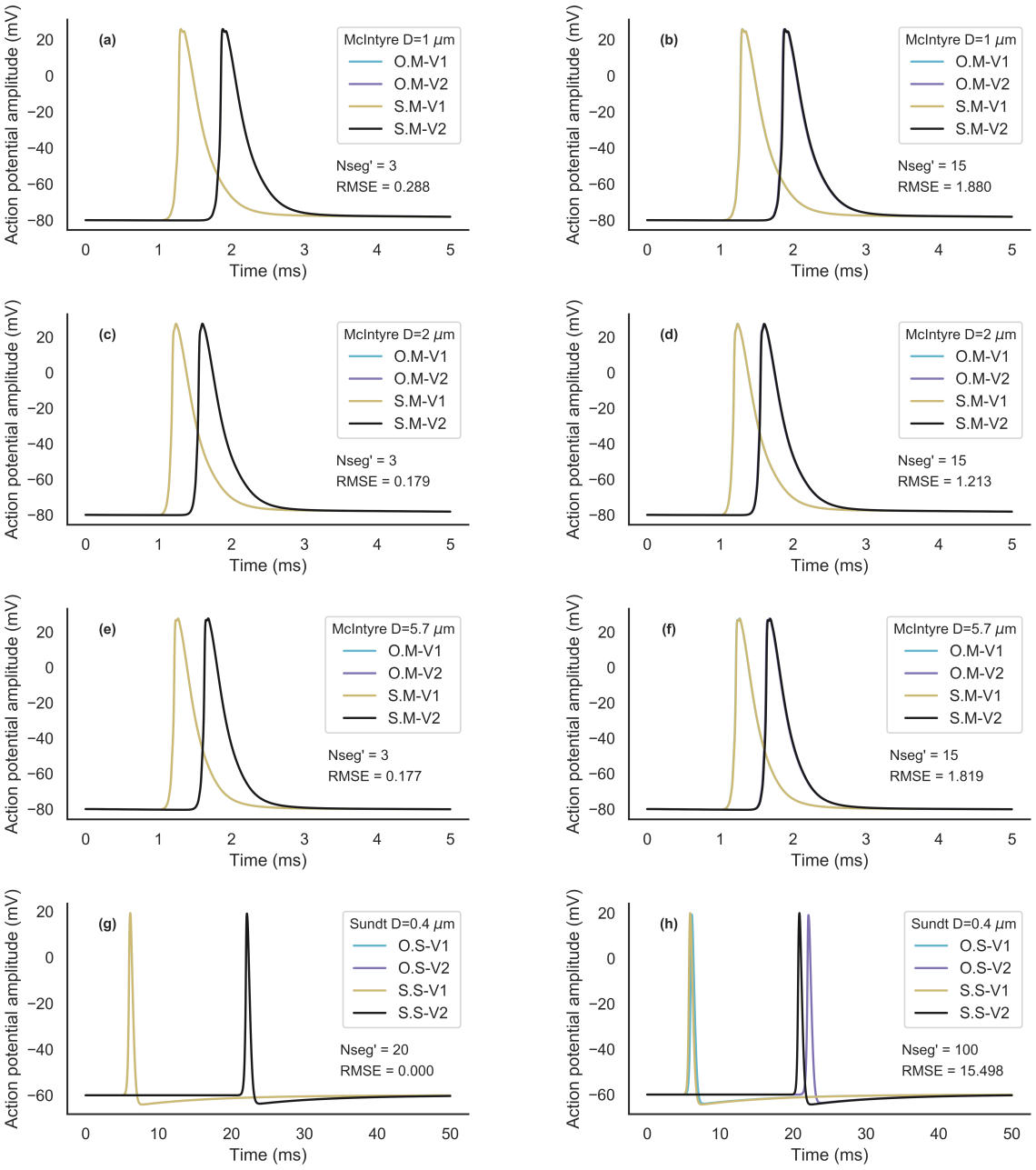

Figure 4.5: A comparison of action potential signals of type I (left) and type II (right) subsectioned models of the McIntyre (D = 1μm, 2μm and 5.7μm) and the Sundt models (D = 0.4μm) with the original model outputs for the parameters that generated the maximum RMSE. O.M = Original McIntyre model. S.M = Subsectioned McIntyre model. O.S = Original Sundt model. S.S = Subsectioned Sundt model.

0.006 m/s, respectively (Table 4.4). For subsectioned Sundt models, the maximum total RMSE values of type I and type II models were 0.000206 mV and 15.497740 mV, respectively (Table 4.3). Although the amount of RMSE for type II subsectioned Sundt model was

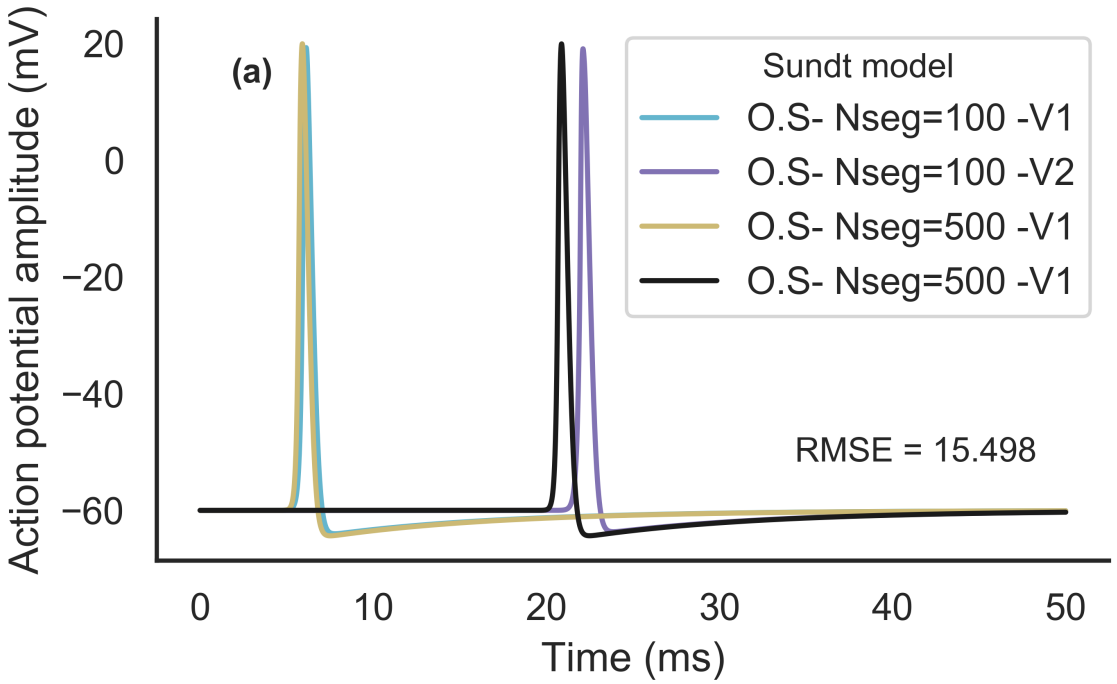

Figure 4.6: A comparison of action potential signals of original Sundt model when number of segments is increased from 100 to 500. O.S = Original Sundt model

greater than the other models in this study (Fig. 4.5h), the action potential amplitude and velocity values were very stable around their mean values (Table 4.4). In order to investigate the cause of large RMSE value for type II subsectioned Sundt model, we increased the number of segments in the original Sundt model from Nseg=100 to Nseg=500 and compared the action potential signals. As it is shown in Fig. 4.6, increasing the number of segments from 100 to 500 in the original model changes the action potential velocity substantially and generates the same amount of RMSE (15.498 mV) as the type II subsectioned model generates (Nseg$'$=100). This suggests that the RMSE value for type II subsectioned model will be reduced if more segments were used in the original Sundt model.

In order to compare the computational efficiency of the original and subsectioned models, the number of segments in the original models was increased to achieve different geometrical resolutions (See Table 4.5). The averaged simulation run-times and number of segments for original (Nseg') and subsectioned (Nseg$'$) models are shown in Table 4.5. Our results (Fig. 4.7) show that using subsectioned models may reduce the simulation run-time substantially when consistent computational accuracy and high geometrical resolution control over the electrophysical and morphological features of the myelinated and unmyelinated axons are needed. Our results indicate that by using the type I subsectioned models, the simulation run-time was reduced by up to 98% and 55% in McIntyre model when geometrical resolutions were 0.125μm and 1μm, respectively. However, the simulation runtimes of the original

Table 4.4: Mean and Standard Deviation Values For Peak Action Potential And Velocity values For Type I and II Subsectioned McIntyre And Sundt Models.

Diameter	Nseg'	Peak AP - V1 (mV)		Peak AP – V2 (mV)		Velocity (m/s)	
		Mean	Std	Mean	Std	Mean	Std
SundtD=0.4 μm	20	19.290486	0	19.090438	3.41E-06	0.32833	0
	100	19.949077	0	19.930257	2.68E-07	0.348029	0
McIntyre D=1.0 μm	3	25.817754	0.000038	25.842158	2.47E-03	3.478261	0
	15	25.695418	0.000008	25.719842	1.60E-03	3.448276	0
McIntyreD=2.0 μm	3	27.50401	0.000473	27.481535	4.32E-03	5.555175	0.005375
	15	27.331959	0.000105	27.344232	9.01E-04	5.479452	0
McIntyreD=5.7 μm	3	27.578187	0.000249	27.663848	2.71E-03	12.195122	0
	15	27.379131	0.000061	27.408432	9.77E-04	11.904762	0

McIntyre model of axons with the diameter of 1μm and 2μm were shorter than type II subsectioned model's runtimes for geometrical resolutions 1μm and 0.5μm. Similarly, by using the sub-sectioning (type I and II) approach, the simulation runtimes were reduced in Sundt model of unmyelinated axons. Type I subsectioned model reduced the simulation run-time by 99% compared with the original Sundt model when geometrical resolution was 0.15μm.

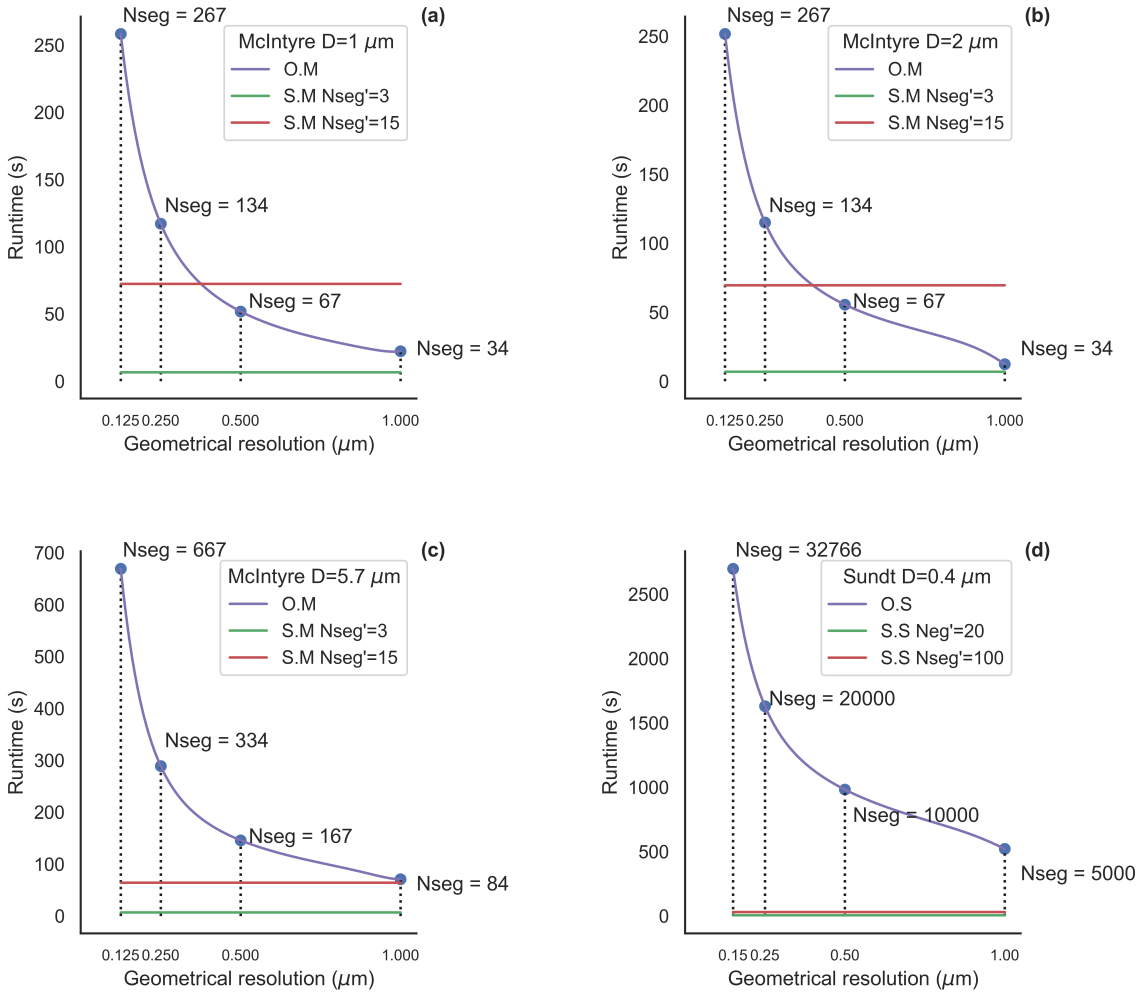

Figure 4.7: A comparison of simulation runtimes to achieve different geometrical resolutions for original and type I and type II subsectioned McIntyre (a, b, and c) and Sundt (d) models. Type I models reduced the simulation time in all simulations. However, type II models could only reduce the runtime when the number of segments (Nseg) required to achieve the desired geometrical resolution in the original models was greater than the number of segments (Nseg') in the subsectioned models times five. The values for simulation runtimes of subsectioned models are based on the average runtimes of the base subsectioned models (when the length of each subsection was 0.2 of the total length of the subsection group) that was described in the method. O.M = Original McIntyre model. S.M = Subsectioned McIntyre model. O.S = Original Sundt model. S.S = Subsectioned Sundt model.

Table 4.5: A Comparison of Simulation Runtimes of Original and Subsectioned Versions of McIntyre and Sundt Models. The Number of Segments for Each Simulation is the Same Along All Axonal Sections.

Diameter (μm)	Model	Geometrical resolution (μm)	Original model Nseg	Original model Runtime (s)	Subsectioned model Nseg'		Subsectioned model Runtime (s)
0.4	Sundt	1	5000	521.08	Type I	20	5.56
					Type II	100	31.2
0.4	Sundt	0.5	10000	981.7	Type I	20	5.56
					Type II	100	31.2
0.4	Sundt	0.25	20000	1630.09	Type I	20	5.56
					Type II	100	31.2
0.4	Sundt	0.15	32766	2697.56	Type I	20	5.56
					Type II	100	31.2
1	McIntyre	1	34	22.27	Type I	3	6.68
					Type II	15	72.47
1	McIntyre	0.5	67	51.86	Type I	3	6.68
					Type II	15	72.47
1	McIntyre	0.25	134	117.15	Type I	3	6.68
					Type II	15	72.47
1	McIntyre	0.125	267	258.24	Type I	3	6.68
					Type II	15	72.47
2	McIntyre	1	34	12.3	Type I	3	6.93
					Type II	15	69.54
2	McIntyre	0.5	67	55.48	Type I	3	6.93
					Type II	15	69.54
2	McIntyre	0.25	134	114.97	Type I	3	6.93
					Type II	15	69.54
2	McIntyre	0.125	267	251.61	Type I	3	6.93
					Type II	15	69.54
5.7	McIntyre	1	84	70.93	Type I	3	6.75
					Type II	15	64.31
5.7	McIntyre	0.5	167	145.78	Type I	3	6.75
					Type II	15	64.31
5.7	McIntyre	0.25	334	288.83	Type I	3	6.75
					Type II	15	64.31
5.7	McIntyre	0.125	667	669.21	Type I	3	6.75
					Type II	15	64.31

4.5 Discussion

An important aspect of computational modeling is to systematically and comprehensively map the response of an outcome to variations in parameters in a way that cannot be achieved in laboratory, animal or clinical studies. However, the value and validity of a computational model depends on the accuracy of the model and the assigned input parameters. In applying computational models, one should factor in different sources of error before drawing conclusions. There are multiple potential sources of error in collecting data from empirical experiments such as morphological measurement errors, variability in firing rate, background activities, and electrode-related recording variability. The sensitivity of model outputs to axonal parameters, modeling methods and related errors is one of the key factors that should be considered when interpreting the results of computational studies. For example, our previous research testing the effects of normal variation in axon morphology on conduction [204] has shown that normal variation in nodal length explains 53% of the

variation in membrane potential models of intact axons. Similarly, changes in normal nodal diameter explained 81% of the variation in conduction velocity. Therefore, accurate measurement of the morphological properties of axons is important for having valid results. The results of this study indicate that using non-uniform subsections to represent each axonal structure in NEURON models is a feasible option for increasing geometrical resolution continuously without increasing the number of segments and computational costs.

The d_lambda rule or similar approaches are helpful in guaranteeing computational accuracy of unmyelinated axonal models at the frequencies of interest [201]. However, increasing the number of segments locally or across the entire axonal model to increase the geometrical resolution may change the model outcomes and induce some errors in comparing the results of different simulations. Our results show that when the number of segments in the original McIntyre model increased (from 1 to 15), the model outputs were changed as well (the total RMSE values were 28.23 mV, 21.66 mV and 27.28 mV for axons with the diameter of 1μm, 2μm and 5μm, respectively). In addition, to achieve fine geometrical resolutions using the conventional approach of increasing the number of segments, the simulation run-time slows down. Our results show that increasing the geometrical resolution from 1μm to 0.125μm in McIntyre model of myelinated axons increased run times 20 fold. Similarly, increasing the geometrical resolution from 1μm to 0.15μm in Sundt model of unmyelinated axons increased run times approximately 5 fold. Moreover, since the maximum number of allowed segments in a NEURON section is 32,766, depending on the dimensions of neuronal structures in different models, it may not be possible to achieve the desired geometrical resolution by increasing the number of segments.

The new approach assessed in this study allows for consistency in assigning and changing the morphological and electrophysiological properties in short and long axonal structures and across axons of different scales when the same geometrical accuracy is required. The value of this approach is in achieving the same level of accuracy as the original models with substantially reduced (up to 99%) computational cost. However, this approach is most effective when a high geometrical resolution over a limited number of continuous but distinct regions along the axons is needed. Some examples of this are in studying: paranodal myelin injury, ionic channels dispersion, or spheroid formation in different regions of axon. However, the limitation of this approach is that there are only four degrees of freedom in each section (since each section is subdivided into five shorter subsections) to modify the axonal properties in the regions of interest. However, the flexibility of this approach can be increased by either combining this method with the conventional method of increasing the number of segments (however, fewer segments are needed and simulations will be faster compared to just increasing the number of segments) or by increasing the number of subsections in each subsection group. In both cases, the stability and computational accuracy of the models should be confirmed before using the simulations results. Moreover, our results (Fig. 4.7) show that unlike type I subsectioned models (Nesg$'$=Nseg/5), type II models

(Nseg′=Nesg) do not always reduce simulation runtimes. In fact, they can only save time when the number of required segments (Nseg) to achieve the desired geometrical resolution in the original model is greater than the number of subsections in each section group times the number of segments (Nseg′) in the subsectioned model. However, as it was shown in Fig. 4.3 and 4.6, the outputs of NEURON models may change as the number of segments change. This could confound the simulation results and make studying the effects of subtle abnormalities and changes on action potential amplitude and velocity challenging. Therefore, type II subsectioned models may provide more consistent results when comparing the effects of injuries over small and large lengths of damaged regions in axonal simulations.

Traumatic brain and spinal cord injuries may cause focal or diffuse injuries such as subtle myelin retraction and detachment [198, 204] in axons that result in network disruption. This may produce clinically important impairments [217]. Studying the effects of subtle injuries in axonal level and the network behavior following injury and investigating the effects of rescuing those mildly damaged axons before the condition progresses and damage is irreversible is important for finding new treatments and early interventions. Saving of up to 99% of the computational cost for each axon is useful in computational studies of axonal networks. Our results suggest that type I subsectioned models always perform faster than the type II subsectioned models as they have fewer number of compartments. However, in order to guarantee the spatial accuracy of NEURON models it is better to use type II models that have the same number of segments as the original models that are developed based on d_lambda rule or similar approaches. Type I models may be very useful in running a large set of simulations very fast (and accurately as it was suggested by Table 4.3 and 4.4) to reduce the parameter space that has to be simulated by more accurate methods like type II models. Moreover, the sub-sectioning approach discussed in this paper makes model conceptualization and experiment design easier as it does not require mapping injury length to the number of segments in each section and in axons with different scales. This results in easier and more intuitive translation of experimental observations to computational simulations.

Chapter 5

The Effect of Spheroids on Action Potential Propagation in Axons of Varied Calibre

5.1 Abstract

Axonal spheroid formation is one of the first clinical pathologies observed following brain injury and in various central nervous system diseases such as multiple sclerosis (MS). However, variations in spheroid presentation in the human brain have not been thoroughly quantified and the functional effects of spheroid formation on action potential propagation have not been established. We performed a detailed morphological analysis on axonal spheroids identified in confocal images of formalin-fixed paraffin-embedded white matter brain tissue from patients with MS or acute cerebral infarct. We then developed computational models of spheroid formation for axons with different calibres (D=1μm, 2μm and 5.7μm). Our results show that there is a significant difference in the distribution of spheroids' volume, area, Feret diameter and the maximum spheroid diameter to normal axonal diameter ratio across axons with different diameters in the brain samples. Our computational studies indicate that small axons (D=1μm) are more sensitive to spheroid formation than the large axons (D=2μm and 5.7μm). The stepwise regression analysis results suggest that spheroid diameter to normal axonal diameter ratio, location, and demyelination level predict more than 45% of the variation in action potential amplitude and velocity post-injury.

5.2 Introduction

Traumatic brain injury (TBI), spinal cord injury (SCI) and multiple sclerosis (MS) share some similar pathophysiological features of axonal degeneration that precede neuronal death [218]. The formation of focal axonal swelling (spheroid) is one of the most common structural changes following spinal cord compression injuries [219]. Prior studies indicate that axonal spheroids may appear as early as five minutes post SCI [78] and may enlarge

up to 30 times the normal axon diameter [82]. Several studies have also reported axonal spheroid formation in patients with Alzheimer's disease [220,221] , Parkinson's disease [222], traumatic brain injury [78,219,223], spinal cord injury [78] and multiple sclerosis [224,225]. Spheroids and demyelination have been observed in acute MS white matter lesions [225]; however, demyelination is not a pre-requisite for spheroid formation, and axonal fragmentation was reported in animal models of MS with an intact myelin sheath [224]. The ability to detect subtle pathological changes and understanding their affect on axonal function is important for diagnosing and treating affected tissues early in the disease and injury progression.

Axonal damage may trigger several injury mechanisms simultaneously that result in different electrophysiological and morphological abnormalities. However, treatments often target single injury mechanisms (e.g., neurofilament damage, membrane permeability etc.) and neuronal structures (e.g., potassium channels). Isolating and studying the functional effects of each of the axonal injuries is very difficult employing *in vitro* or *in vivo* experiments. Although some studies suggest spheroid formation may cause functional deficits in patients [79,226,227], there is no experimental data to quantify the relation between axonal spheroids and action potential generation in a single axon or large networks of axons. Most of our knowledge about the functional effects of focal axonal spheroid (FAS) formation is based on computational studies. Computational studies using FitzHugh–Nagumo based models [226] of non-myelinated axons suggest three main outcomes, 1- transmission, 2- reflection and 3- blockade may occur following spheroid formation. The geometry of spheroids, in particular their tapering, was identified as a key parameter that determines if the action potential gets blocked or passed. It was shown that a sharp increase in axonal diameter may block action potential propagation while a gradual increase in axonal diameter may support signal propagation even for large spheroids in non-myelinated axons. However, computational studies of myelinated axons with diameters of 0.408 μm, 0.48 μm and 0.6 μm [79] showed that axons with a large spheroid, with an abrupt diameter change, in internodal regions may still continue propagating action potentials. In these studies, the geometrical differences of spheroids such as tapering were not wholly included in the model. Most of the literature on axonal spheroids have been focused on reporting spheroid diameters and post-injury frequency of spheroid formation along the axons [78]. The amount of published data on geometrical characteristics of spheroids and their variability among different axonal sizes is very limited. Most of the current literature describing spheroid morphology is based on animal models of human diseases or controlled *in vitro* experiments, which may be different from spheroids in the human CNS. Developing biophysical models of spheroids that link the physical characteristics of spheroids to action potential propagation dynamics could assist in distinguishing the effect of spheroid morphology on axonal function in humans.

The overall goal of this study was to quantify the physiological impact of human CNS axonal spheroids on action potential propagation by analyzing and characterizing the spheroids

Table 5.1: Patient information

Case	Age(years)	Sex	Diagnosis	PMI*	Anatomical location
1	40	Male	MS (acute)	Unknown	Periventricular white matter
2	71	Male	Infarct (1 month)	1 day	Parietal lobe
3	45	Female	MS (life long)	Unknown	Cerebellum
4	82	Male	Infarct (5 days)	1 day	Parietal

*Post-mortem interval

that appear in human brain tissue. To be more specific, we focused on spheroids that were formed by swelling in the axolemma, not the myelin layer. Our hypotheses were (1) that spheroid morphological properties vary based on the size of the axon and (2) that spheroid size, location and axonal diameter would affect the function of axons. The specific objectives were (1) to characterize the morphological properties of axonal spheroids identified in confocal microscopy of human brain pathology samples, (2) to map the relative effects of variations in spheroid parameters such as diameter, location, length and frequency on predicted signal conduction characteristics using a biophysical computational model in three myelinated axon models with different diameters. This is the first study to quantify the amount of variation in the diameter of the axolemma along the length of spheroids and to measure spheroid volume and surface area in human brain samples, to integrate normal structural variation into computational models of spheroids in myelinated axons, and to highlight the interactive effects of normal structural variations and damage on axonal function.

5.3 Materials and Method

5.3.1 Patient selection

The Clinical Research Ethics Board of the University of British Columbia (H01-70430) approved the study. This study was conducted on archival, paraffin-embedded, formalin-fixed brain tissues obtained from two people with multiple sclerosis and two people with acute cerebral infarct (mean age 59.5 years, range 40-82 years) (Table 5.1). Following death written consent was obtained from the next of kin for autopsy and use of their brain tissue for scientific research. The diagnoses were confirmed by a neuropathologist, and the brain blocks were anonymized for sectioning and staining.

5.3.2 Tissue processing and immunohistochemistry

Tissue sections (8 µm thickness) were prepared for immunofluorescence. Briefly, formalin-fixed sections were heated in a tissue-drying oven for 25 minutes at 60°C. To deparaffinize, the slides were washed in 3 changes of xylene for five minutes each at room temperature (RT) followed by rehydration in a graded series of ethanol washes. Antigen retrieval on these

sections was performed by microwave irradiation (R-410DKC, Sharp) at power 90 and 70 for two minutes each and then at power 50 for six minutes in 10 mmol/L sodium citrate buffer (PH 6.0), sections were allowed to cool for 20 minutes at RT and then washed in phosphate buffered saline with Tween (PBS-T).

Immunofluorescent staining was performed on three serial sections from white-matter regions of the selected blocks using multi-step staining. Briefly, slides were kept for 30 min in PBS containing 5% (v/v) normal donkey serum at room temperature. The block was removed, and the slides were incubated overnight at RT in chicken polyclonal neurofilament (NF) antibody (Ab) (AbCam (ab72997), San Francisco, CA, USA) at a dilution of 1/100 on a shaking plate. The slides were washed in PBS-T three times for five minutes at RT the day after. Donkey anti-chicken AlexaFluor 647 (ThermoFisher/Molecular Probes, Eugene, OR, USA) at a dilutation of 1/200, as secondary Ab was used to stain NF. Nuclear staining was performed using 4',6-Diamidino-2-Phenylindole (DAPI) (ThermoFisher/Molecular Probes, Eugene, OR, USA), and this was followed by staining with 0.15 - 0.3 percent Sudan Black B (SBB) (Fisher Scientific, Fair Lawn, NJ, USA) in 70% ethanol in order to minimize autofluorescence [228–230]. The negative control slide was stained using the appropriate isotype control antibody at matched concentrations.

5.3.3 Image Acquisition

To locate the regions of interest (ROIs) in normal-appearing white matter, lesions were first outlined and excluded from imaging based on the absence of SBB staining using the acquired brightfield images. ROIs were outlined for each section (at least 10 mm away from the edge of lesions and avoiding neurofilament-labeled fiber tracts emerging from gray/white matter lesions [231]) and studied using Leica SP8X STED white light laser confocal microscope, 100X/1.4 Oil HC PL APO CS2 STED, WD 0.13 mm objective and HyD detectors (Leica Microsystems, Wetzlar, Gernay). Image acquisition was carried out using LAS AF software.

5.3.4 Spheroid detection and morphological analysis

Image analysis used custom scripts in Fiji (National Institutes of Health, Bethesda, Maryland, United States) [232], an open-source extension of ImageJ platform (National Institutes of Health, Bethesda, Maryland, United States) [233] for biological-image analysis and Matlab (MathWorks, Natick, MA, United States) [234]. Forty-eight confocal microscopy image stacks (110 μm X 110 μm images with layer range 17-48 images along the z-axis) were imported in ImageJ employing the Bio-Formats plugin (The Open Microscopy Environment, 2016). A line grid was laid over all images in Fiji which resulted in each image being divided into 81 smaller squares (total population size: 3888) with the area of $150\mu m^2$ each (See Figure 5.1a). To characterize spheroids properties and perform morphological analysis with a 95% confidence level and 5% margin of error, 384 squares were selected randomly and analyzed as described in the following procedure. A random number generation algo-

rithm was used [235] to generate a sequence of eight unique numbers between 1 and 81, corresponding to a square number for each image set. A trained reviewer scrolled over each layer in the z-stack for each square and identified spheroids. Any spheroid overlapping the grid lines were also included in the study. For each spheroid, the boundary of the spheroid (ROI) at each plane was marked using Fiji's freehand tool and selections were added to Fiji's ROI manager as long as the spheroid's boundary could be clearly distinguished from the background image. Finally, the selected ROIs were used to measure several morphological parameters of each spheroid, including diameter, surface area, volume, and maximum Feret diameter (the longest distance between any two points along the selection boundary) in Fiji (See Table 5.2).

Although axons are generally thought to have a circular cross-section and have a cylindrical shape [236], axonal spheroids may have asymmetrical geometry and more sophisticated approaches should be used to calculate their diameters. Previous studies [237] focused on measuring the diameter of biological structures similar to axons, such as retinal vessels, measured the radius of the maximum inscribed circle along the vessel's medial axis (center-line) [238, 239] to estimate its local diameter in two dimensions. However, this approach fails to capture subtle diameter changes along axonal spheroids with irregular shapes and asymmetric geometry. Therefore, in this paper, we employed a modified approach that is described here. To find a spheroid's diameter, the original spheroid images and their respective ROIs were imported in Matlab and converted to binary masks to classify image pixels (spheroid vs background) and define the region of interest in Matlab (See Figure 5.1c). To make the boundaries of the spheroid smoother, a 5X5 blur filter (a kernel with a value of 0.04 at each cell) [240] was applied to each binary spheroid mask and the output image was thresholded (pixel intensity > 0.5) again. In order to find the overall shape of each spheroid, the medial axis of each spheroid's binary mask was found in Matlab using the BWmorph library [234]. For each spheroid mask, small spurs (branches) were removed to only keep the longest connected line that forms the center-line of the spheroid. A second-order polynomial was fitted to the points (window size $= 5$) on the center-line to find the slope of the tangent at each point along the spheroid's medial axis. The diameter was defined as the Euclidean distance between the two crossing points on the spheroid's boundary which were found by drawing a perpendicular line at each point along the center-line (see Figure 5.1b). However, because of the irregularity in the shape of spheroids, there were some points on the center-line with a sharp change in the slope value. In order to correct diameter measurements, a two-step adaptive local outlier detection algorithm was used first to find the points with more than three scaled median absolute deviations (MAD) away from the median and then the points with more than three standard deviations from the mean in a moving window (size $= 5$ pixels). The detected outlier values were replaced by the value of the nearest non-outlier point in the same window. Finally, all the calculated diameter values were smoothed

Table 5.2: Spheroid parameters measured in Fiji and Matlab.

Parameter	Unit	Description
AxonD	(μ)	The normal diameter of the axon
Diameter	(μ)	The diameter of the spheroid along its center-line at each plane in the z-stack
Area	(μm^2)	Area of the spheroid at each plane in the z-stack
Perimeter	(μ)	Perimeter of the spheroid at each plane in the z-stack
Max Feret Diameter	(μ)	Max Feret Diameter at each plane in the z-stack
Volume	(μm^3)	Spheroid's volume
Spheroid Diameter Ratio (SDR)	-	The ratio of spheroid's maximum diameter to the axon's normal diameter
Central Region Length Ratio (CLR)	-	$\frac{x_{max}-x_\beta}{x_{max}-x_\alpha}$ (see Figure 5.1)
Lateral Region Length Ratio (LLR)	-	$\frac{x_\beta-x_\alpha}{x_{max}-x_\alpha}$ (see Figure 5.1)
Lateral Region Average Diameter Ratio (LADR)	-	$\frac{\text{Average diameter of points between } x_\alpha \text{ and } x_\beta}{D_{max}}$

with a low-pass moving average filter (windows size= 5) and results were scaled based on the physical dimensions of confocal microscopy images for each spheroid.

In order to describe the diameter changes along the spheroid center-line, we followed the approach suggested by Mia and colleagues [226, 227] for studying morphological abnormalities and tapering in non-myelinated axons. Three points along the center-line of each spheroid mask were marked in the plane that the spheroid had the maximum diameter. First, the point that the spheroid had its maximum diameter (x_{max}) was identified and then the diameter differences (δ_D) between the maximum point and both ends of the spheroid in the same plane were calculated. The endpoint that had a greater diameter difference with the maximum diameter point was selected. Subsequently, by traversing along the center-line of the spheroid from the selected end point, the first points that had a diameter of greater than or equal to the diameter of the selected end point plus 10% (x_α) and 90% (x_β) of δ_D were marked. Accordingly, spheroid diameter ratio (SDR), spheroid central region length ratio (CLR), spheroid lateral region length ratio (LLR) and spheroid lateral region average diameter ratio (LDR) were calculated (see table 5.2) using the marked key points for each spheroid.

5.3.5 Computational Modeling and Axonal Spheroid Simulations

Computational models were used to quantify the functional effects of spheroids. However, to be consistent with our histopathological observations from confocal microscopy images, we focused on spheroids that are formed by the change in the size of axolemma and not the myelin sheath surrounding the axons. Simulations were performed for axons with different scales and the diameters of 1μm, 2μm, 5.7μm using the validated biophysical model of mammalian axons that we previously described [241, 242]. This model is based on the geometrically accurate model of myelinated motor neurons developed by McIntyre and colleagues [2]. However, the model was modified to allow computationally efficient simulation of fine axonal abnormalities and, more importantly, allows for consistency in comparison of simulation results across axons of different scales when the same geometrical accuracy

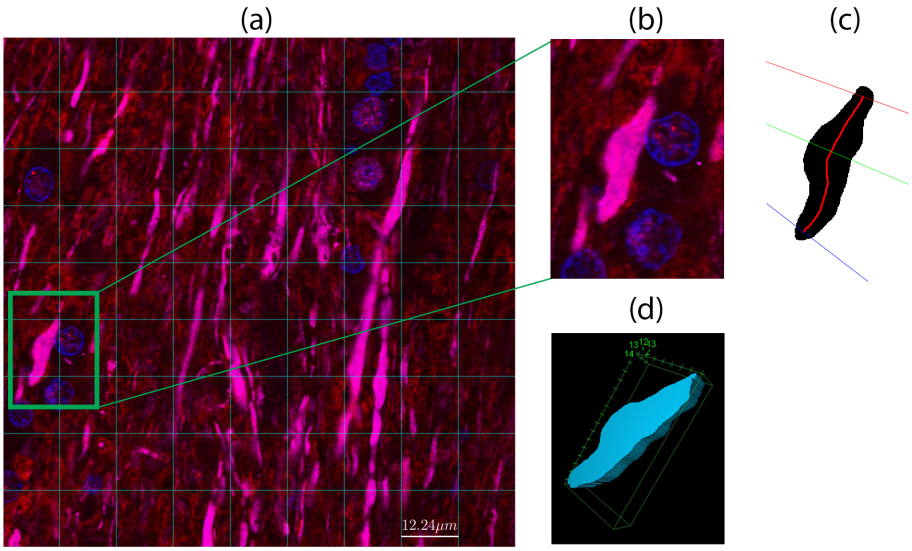

Figure 5.1: Axonal spheroids identified in confocal images. (a) shows a 2D image of a sample collected from human brain tissue. Each confocal image is composed of multiple layers of 2D planes stacked together along the z-axis. Axons are stained with NF (magenta) and nuclei with DAPI (blue). (b) is a zoomed view of the spheroid in the green rectangle in (a). The boundaries of each spheroid were marked in each plane that was used for creating 3D volumes and 2D binary masks. (c) Shows the binary mask of the spheroid in Matlab. The red line is the medial axis of the spheroid. The perpendicular lines to the medial axis of each spheroid mask were used to measure diameter along the spheroids' center-line. (d) a 3D representation of the spheroid in ImageJ to calculate spheroid volume and 3D Feret diameter.

is required. The modified model was composed of 11 different sections between each neighbouring node of Ranvier: two paranodal sections (PARA), two main juxtaparanodal sections (JUXTA) and seven stereotyped internodal sections (INTRA). Each section was composed of five subsections. The lengths of the subsections can be changed individually while keeping the total length of the section constant. All subsections were then composed of three equally-length segments (n_{seg}) to guarantee computational stability in simulations. Electrophysiological and morphological properties of each segment were the same along its length. Three active channels, fast and persistent sodium, and slow potassium, were in the nodal areas that help in generating action potentials and were modelled using modified Hodgkin-Huxley based equations. The axonal membrane in the juxtaparanodal regions was covered by fast potassium channels [2].

A comprehensive sensitivity study was done to investigate the relative effects of different spheroid parameters, including spheroid's maximum diameter, tapering and frequency on action potential disruption. For simplicity, we focused on symmetrical spheroids. Axonal spheroids were simulated by increasing the axons' diameter in the swollen regions and changing related electrophysiological properties of the axons accordingly. In particular, the density of ion channels per unit area was reduced such that the total number of active ion channels in the spheroid regions kept constant before and after spheroid formation. There is no experimental data on the amount of change in the values of axoplasmic resistivity before and after spheroid formation in axons. Therefore, following the approach used by Kolaric and colleagues [79] and Mia and colleagues [226, 227] the axoplasmic resistivity (70 Ω cm) of the axon were kept constant before and after injury in our simulations. However, diameter dependent passive properties of the axon, including axoplasmic resistance, axolemma capacitance, and membrane conductance, were changed as the size of the axonal membrane changed in swollen regions.

Spheroid tapering was modelled by splitting each spheroid into three regions **(See Figure 5.2)**. The middle region was the center of the spheroid with the maximum diameter (D_{max}) which was equal to the normal axonal diameter in that region multiply by diameter change ratio. Regions one and three were the lateral portions of the spheroid with the same diameter and length. Spheroids were not bounded by a specific axonal region and could be extended to several regions. In other words, depending on the length of the spheroid, one or more axonal regions (nodes, paranode, etc.) could be overlapped by each spheroid region (regions 1, 2, and 3). Therefore, the diameter of each axonal section was changed to be the same as the diameter of the overlapping spheroid region. However, regardless of the axonal diameter in the swollen region, the electrophysiological properties of each section were changed independently from the rest. Other than spheroid's total length, all spheroid morphological parameters (see Table 5.3) were based on the experimental measurements obtained from the human brain tissue samples. Therefore for each spheroid parameter (SDR, CLR and LADR), the minimum, maximum and the middle values of measurements from

Table 5.3: Sensitivity study parameters

Parameter	Values
Fiber diameter	$1\mu m$, $2\mu m$, $5.7\mu m$,
Spheroid location	Node, Paranode, Juxtaparanode, Internode
SDR	1.7, 20.3, 39
Spheroid length	$1\mu m$, 3 μm, 10 μm
CLR	0.1, 0.42, 0.82
LADR	0.55, 0.75, 0.95
Spheroid's demyelination level	0%, 50%, 100%
Frequency	1, 3, 5, 7

our histological observations (see Table 5.4) were used in these simulation. In order to study the effects of spheroid location (node, paranode, juxtaparanode, etc.) on axonal function, we set the length of spheroids in our sensitivity study such that some spheroids were bounded in only one axonal region (See Table 5.3).

Following performing the sensitivity analysis, a series of simulations were done to study specific effects of spheroid formation on action potential propagation for selected configurations in more detail. In the first experiment, to investigate how the changes in the values of spheroid's tapering related parameters (CLR and LADR) affect action potential amplitude and conduction velocity, one single spheroid (SDR=20.3) with the length of $1\mu m$ was modelled at a node of Ranvier in the middle of the three axon models with the diameters of $1\mu m$, $2\mu m$, $5.7\mu m$. CLR and LADR values were changed from 1 to 82 (n=10) and from 0.55 to 0.95 (n=10), respectively. To quantify the effect of spheroid location and frequency of axon physiology, the spheroid's location (i.e. node, paranode, juxtaparanode and internode) and the number of spheroids (1, 3, 5, 7) were changed (SDR=20.3, length= 1 μm, CLR=0.42 and LADR=0.75). To quantify the interaction between spheroid location and the SDR value, a spheroid (CLR=0.42, LADR=0.75) with the length of $1\mu m$ was modelled and spheroid location and SDR (1.7-39, n=10) changed. Finally to map the interaction between spheroids and demyelination on signal conduction, spheroids (SDR=20.3, CLR=0.42, LADR=0.75) with the lengths of 1 μm were modelled at different myelinated regions of the axon and the level of demyelination was changed (0-100%, n=11). Demyelination was modelled by reducing the thickness of the myelin layers in swollen regions.

The axonal model used for these simulations had 21 nodes of Ranvier, and the epicentre of spheroid formation was at node 10. To generate an action potential in the axon, a depolarizing current of 2nA with the duration of 1ms was injected in node 0 of the axon. In order to avoid sealed end effects [1], recordings were done from nodes 5 and 15 of the axon. All simulations were run with a time step of 0.005 ms.

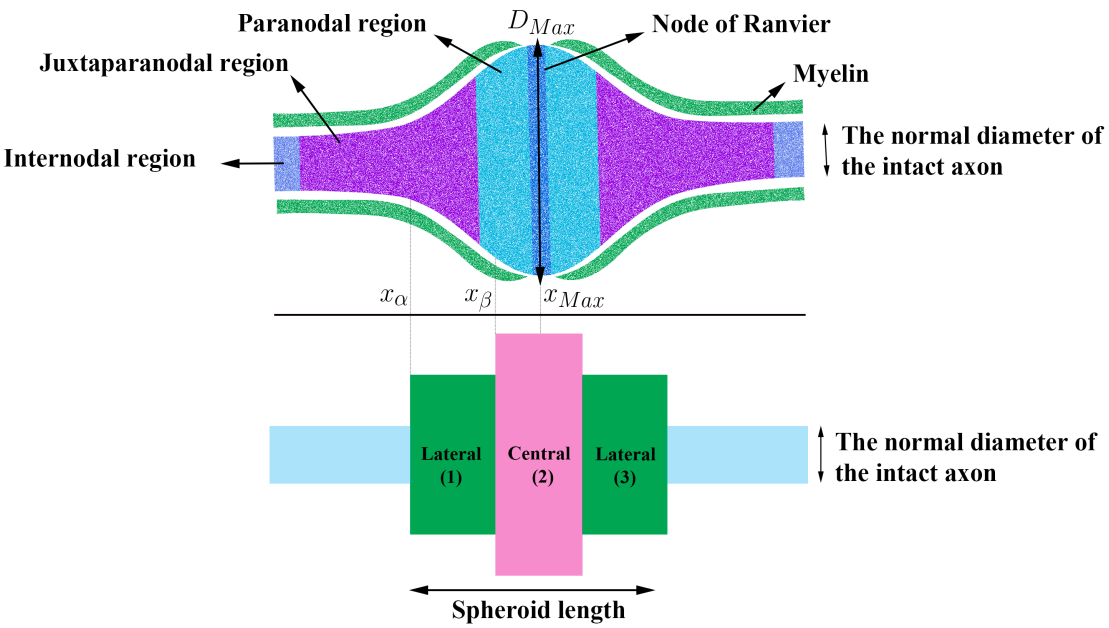

Figure 5.2: An axonal spheroid and its representation in Neuron. Top: shows an illustration of a spheroid centered at the node of Ranvier of a myelinated axon that is expanded over paranodal and juxtaparanodal regions. Bottom: The spheroid tapering was modelled by splitting the spheroid in three regions. In this example model, the central region (pink) of the spheroid is overlapping with the nodal and paranodal regions of the axon. The diameter of each point of the axolemma in the central region is equal to the maximum diameter (D_{Max}) of the spheroid in the top image. However, regardless of the diameter of each point, the electrophysiological properties (including the myelination level) of these sections were changed individually in Neuron. The boundary and the length of the lateral regions of the spheroid (green) were determined by identifying the x_α and x_β points along the spheroid (see table 5.2). In this example, the lateral regions of the spheroid are overlapping with paranodal and juxtaparanodal regions of the axon. The diameter of each point of the axolemma in the lateral regions is equal to the average diameter of all points between the x_α and x_β points of the damaged axon. However, similar to the central region, all other parameters (e.g. number of myelin layers, number and types of ion channels, axolemma resistance and capacitance, etc.) were changed individually to simulate the electrophysiological properties of each axonal region (i.e. paranode, juxtaparanode, etc.).

5.3.6 Statistical analysis

Statistical analyses were performed by SciPy library [243] implemented in IPython version 7.4.0 [244] and JMP (Version 15. SAS Institute Inc., Cary, NC, 1989-2019). Axons were placed into four groups based on the normal axonal diameter's quantiles of identified spheroids. D'gostino and Pearson's test [245, 246] of normality showed that the data distribution in each group is not Gaussian. Therefore, the non-parametric Kruskal-Wallis H-test was used to test if there was a significant difference (α=0.05) in the median values of each measured parameter between different groups. Conover's post-hoc test [247] was used to make pairwise comparisons between different groups.

5.4 Results

5.4.1 Detection and quantification of axonal spheroids in human brains samples

Two hundred and thirty-seven spheroids were identified and marked from the brain tissue of four patients for further analysis after a double-blind review of axons in different layers of confocal images by moving the plane of focus up and down through each section. The normal axonal diameter for identified spheroids ranged from 0.244 μm to 2.78 μm (mean: 0.791 μm and std: 0.383 μm). Axons were categorized in four groups (G1: (0.244 μm, 0.487μm] | count= 61, G2: (0.487 μm, 0.653 μm] count=60, G3: (0.653 μm, 0.9 μm] count=57, G4: (0.9 μm, 2.78 μm], count: 59) based on the normal axonal distribution quantiles. Preliminary analysis suggested a non-Gaussian distribution for spheroid parameters such as diameter, volume and surface area. Therefore, non-parametric tests were employed to study variations among different axonal groups. Spheroids' volume ranged from $4.02\mu m^3$ to $3926.5\mu m^3$ (mean: 160.87 μm^2, std: 478.41 μm^2). Spheroids' surface area (in the image plane) was ranged from 1.04 μm^2 to $533.64\mu m^2$ (mean: 31.07 μm^2, std: $64.79\mu m^2$). Feret diameter, the longest distance between any two points along the spheroid's ROI boundaries in 3D space, was measured for each spheroid and ranged from $3.51\mu m$ to $57.30\mu m$ (mean: $10.64\mu m$, std: $7.06\mu m$). The results of Kruskal-Wallis H-test and post-hoc Conover test suggested there is a significant difference (α<0.05) in distribution of spheroids' volume ($\chi^2 = 91.55$, $p < 0.001$), surface area in 2D planes ($\chi^2 = 96.77$, $p < 0.001$) and Feret diameter in 3D space ($\chi^2 = 79.42$, $p < 0.001$) among different axonal groups (ie. G1, G2, G3, G4). In general, larger diameter axons have higher median values of spheroid's volume, surface area (in 2D planes) and the 3D Feret diameter than smaller axons (see table 5.4).

The diameter of each spheroid along its center-line was measured at different levels (total of 2339 planes) in the z-axis, and the level that each spheroid had its maximum diameter was found. The overall maximum diameter for each spheroid ranged from $1.7\mu m$ to $23.09\mu m$ with the mean and standard deviation of $3.343\mu m$ and $2.48\mu m$, respectively. However, the lowest value for the maximum spheroid diameter among all 2339 planes was $1.1\mu m$. The

minimum and maximum value for SDR, the spheroid's maximum diameter to the axon's normal diameter ratio, were 1.69 and 38.96, respectively. The mean and standard deviation for SDR were 4.99 and 3.24, respectively. Given the normal variability in the size and diameter of spheroids and the constraints imposed by the resolution of the original confocal microscopy images and spheroid masks, it was only possible to apply 10%-90% rule (see methods section) to 2106 images (planes) for 211 spheroids to get an accurate measure of CLR, the normalized length of the central part of the spheroid, LLR, the normalized lateral region length ratio and LADR, the lateral region average diameter ratio along spheroids' center-lines. However, for consistency, we calculated CLR, LLR and LADR values for each spheroid in the plane that the SDR value was maximum. The mean value for CLR, the normalized length of the central part of the spheroid, was 0.2±0.13 (0.01 - 0.82). On the other hand, the mean value for LADR, lateral region average diameter ratio, was 0.77±0.08 (0.55 - 0.95). Kruskal-Wallis H-test suggests that the CLR ratio had the same distribution among different axonal size groups ($\chi^2 = 3.334$, $p = 0.343$). On the other hand, there was a significant difference ($\chi^2 = 15.06$, $p = 0.002$) in the LADR ratio distribution across different axonal groups. Similarly, SDR ratio's distribution was significantly different ($\chi^2 = 59.16$, $p < 0.001$) across axonal groups and smaller groups had higher median SDR values than the larger axonal groups (see table 5.4).

5.4.2 The effects of axonal spheroids on action potential propagation

To evaluate the possible effects of spheroids on signal conduction, 11,665 simulations with different injury settings were performed for axons with the diameters of $1\mu m$, $2\mu m$ and $5.7\mu m$. Action potential amplitude and velocity values in intact axons ranged from 25.84 mV to 27.66 mV and 3.48 m/s to 12.2 m/s, respectively.

Spheroid parameters with the greatest effect on membrane potential

A series of simulations determined the relative effects of axonal spheroids and local demyelination on membrane potential and conduction velocity. The studied parameters are spheroid's length, SDR, CLR, LADR, local demyelination level, location, and frequency of spheroid formation along the axon. Multiple stepwise regression analysis was conducted in JMP. The linear models (3rd order polynomials and interaction terms) explained 82.3%, 80.7% and 81.1% of the variation in membrane potential of damaged axons with the diameters of $1\mu m$, $2\mu m$ and $5.7\mu m$, respectively. Stepwise regression analysis revealed that spheroid's location (31.2%, 26.9% and 25.7%), SDR (12.1%, 12.5% and 9%) and demyelination level (6.8%, 6.6%, and 10.6%) are the main predictors ($P<0.05$) of the amount of post-injury variation in membrane potential in axons with the diameter of $1\mu m$, $2\mu m$ and $5.7\mu m$ (see Figure 5.3). The frequency of spheroids explained only 2.4% and 3.2% of the variation in action potential amplitude of axons with the diameters of $1\mu m$ and 5.7μ, respectively. In contrast, the action potential amplitude of the axon with the diameter of $5.7\mu m$

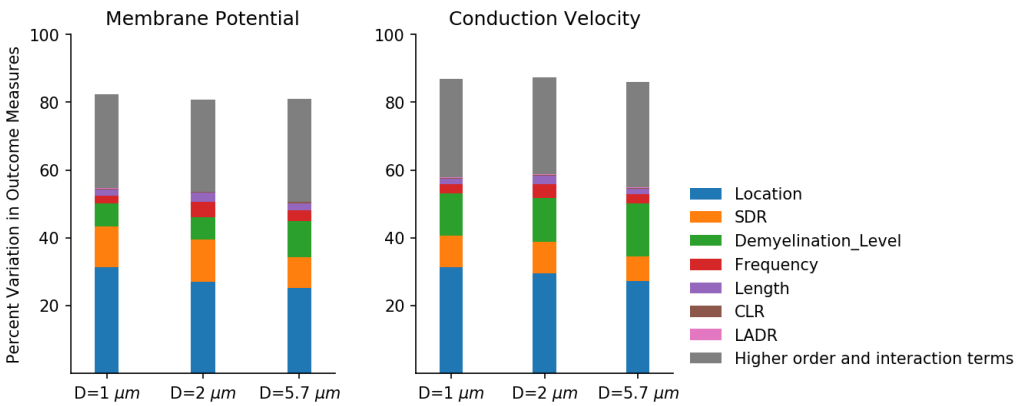

Figure 5.3: The relative effects of axonal swelling injury parameters on membrane potential and action potential propagation on axons with the diameters of $1\mu m$, $2\mu m$ and $5.7\mu m$. Spheroid's location (Node, Paranode, etc.), SDR and spheroid's demyelination level are the key predictors of membrane potential and conduction velocity in all axons.

was slightly more sensitive (4.5%) to spheroid frequency. Membrane potential in axons with the diameters of $1\mu m$, $2\mu m$, and $5.7\mu m$ was less sensitive to spheroid length (1.7%, 2.8%, 2.2%). The rest of the variation in membrane potential was due to interaction terms and higher-order terms.

Similarly, linear models explained 86.8% (D=$1\mu m$), 87.5% (D=$2\mu m$) and 86.4% (D=$5.7\mu m$) of variation in conduction velocity of damaged axons in our simulations (Figure 5.3). Conduction velocity in axons with the diameter of $1\mu m$, $2\mu m$ and $5.7\mu m$, was more sensitive to the spheroid location (31.3%, 29.4% and 27.3%) and demyelination levels (12.5%, 13% and 15.7%). SDR accounted for 9.3%, 9.3% and 7% of the variation in action potential conduction velocity in axons with the diameter of $1\mu m$, $2\mu m$ and $5.7\mu m$, respectively. On the other hand, the frequency of spheroid formation along the axons explained 2.7%, 4% and 2.7% of conduction velocity variation in axons with the diameters of $1\mu m$, $2\mu m$ and $5.7\mu m$, respectively. Spheroid length, LADR, CLR and higher order terms are responsible for the rest variation in action potential conduction velocity.

Specific cases of spheroid formation

A series of simulations were done to quantify the effects of the variation in different spheroid parameters, including SDR, CLR, LADR, frequency and demyelination levels on action potential propagation. In the first experiment, we modelled one single spheroid (SDR=20.3, Length=1 μm) located at the tenth node of Ranvier (node 10) of axons with the diameters of $1\mu m$, $2\mu m$ and $5.7\mu m$. CLR and LADR values were changed from 0.01 to 0.82 and from 0.55 to 0.91, respectively. Our results indicate that the relationship between spheroid parameters and action potential amplitude and velocity is highly non-linear (see Figure 5.4). Although the small (D=$1\mu m$) and large (D=$5.7\mu m$) axons failed to conduct action potential signals

for a wide range of CLR and LADR values (Figure 5.4), there was a small reduction (<2%) in action potential amplitude of the axon with the diameter of $2\mu m$. However, the speed of signal propagation in the axon with the diameter of $2\mu m$ was reduced substantially (mean=41.95%, std=10%). On the other hand, for a specific combination of parameters (CLR=0.01 or 0.037 and 0.55<LADR<0.95) all axons could transmit signals, however, the speed of signal propagation was reduced by 20.68% to 42.21% compared to the intact axons (Figure 5.4d, 5.4e, and 5.4f).

The results of the second experiment to study the effects of spheroid location and frequency on action potential amplitude and velocity (see Figure 5.5) showed that nodes of Ranvier are the most sensitive point along the length of an axon; that even a medium-sized spheroid (SDR=20.3, L=$1\mu m$) may completely block action potential signals in the small (D=$1\mu m$) and large (D=$5.7\mu m$) axons. In contrast, juxtaparanodal and internodal regions had the highest robustness to spheroids with intact myelin sheaths in all axons. Increasing the number of spheroids along the axon led to a further reduction in action potential amplitude and velocity in all axons (figure 5.5a-f). Although the $2\mu m$ axon showed similar overall behaviour, it was more robust to disruptions in action potential propagation due to spheroid formation in the nodes of Ranvier and paranodal regions (Figure 5.5b and 5.5e).

The results of the experiment to quantify the effects of spheroid location and SDR on action potential conduction and amplitude (figure 5.6) showed that increasing the SDR value for a single spheroid (L=$1\mu m$, CLR=0.42, LADR=0.75) decreased the ability of axons to conduct action potentials or caused signal propagation blockade when the SDR value was greater than 27 in all axons.

The results of the experiment to map the interaction between spheroids location and demyelination levels on signal conduction indicate that the paranodal region was most sensitive to spheroids. When spheroids were at three paranodal regions (adjacent to nodes 9, 10 and 11) of the small axon (D=$1\mu m$), conduction was blocked even in the absence of any demyelination (see Figure 5.7). Larger axons (D= 2 $\mu m$and $5.7\mu m$) showed similar behaviour, however, transmitted action potentials unless the spheroids were fully demyelinated. Juxtaparanodal and internodal regions were more robust to spheroid formation. All axons could continue signal propagation with minimum reduction in action potential amplitude (<0.05%) or velocity (<1.8%) compared to intact axons when spheroids were at juxtaparanodal or internodal regions even when the thickness of the myelin sheath was reduced by 90% (Figure 5.7) of their normal values. However, propagation stopped in all simulated axons when all three spheroids were fully demyelinated.

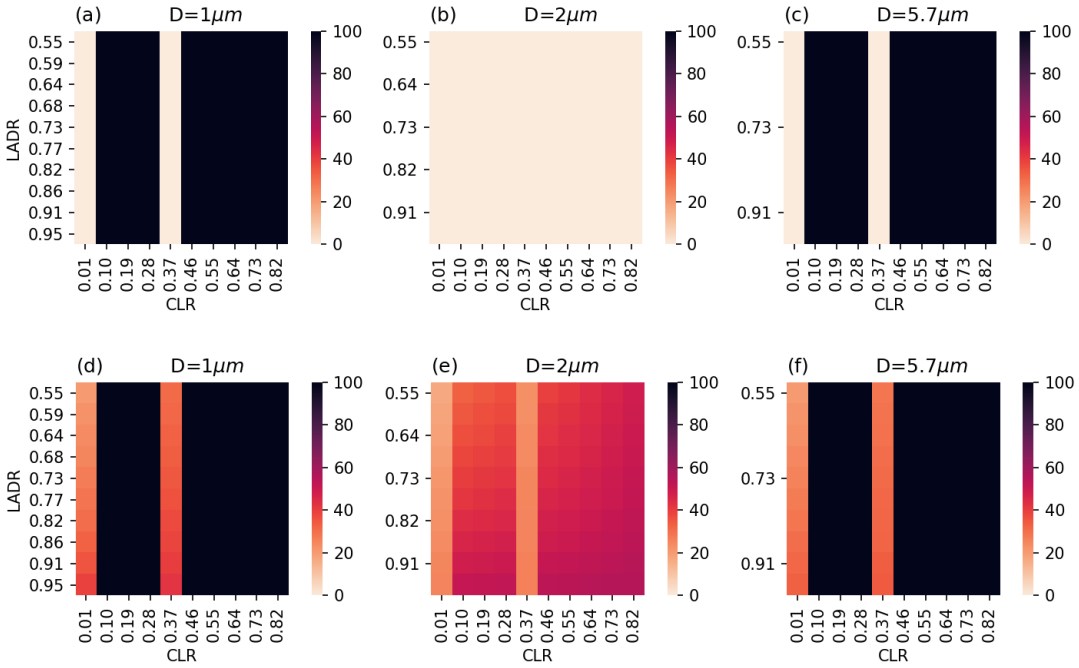

Figure 5.4: Percent reduction in membrane potential amplitudes (a, b, c) and conduction velocities (d, e, f) because of variations in CLR and LADR when a single spheroid with the SDR of 20.3 and length of $1\mu m$ was modelled in node 10 of axons with the diameters of $1\mu m$, $2\mu m$ and $5.7\mu m$. The relationship between axonal size, membrane potential and spheroid parameters is highly non-linear. Although action potential propagation was blocked (a, d, c, f) in small (D=$1\mu m$) and large (D=$5.7\mu m$) axons when CLR >0.46, the axon with the diameter of $2\mu m$ could still propagate AP signals with minimal reduction in their amplitudes (b) however at much lower (<60%) velocities (e) compared to the intact axon with the same size.

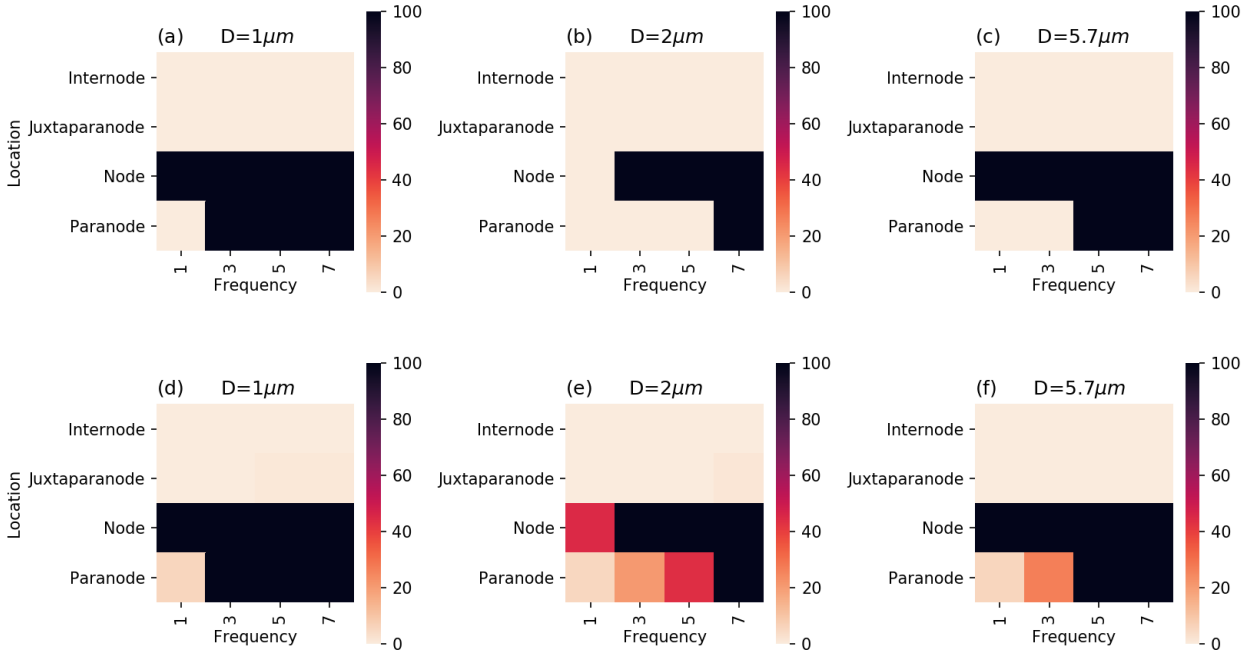

Figure 5.5: Percent reduction in membrane potential amplitudes (a, b, c) and conduction velocities (d, e, f) because of variations in spheroid location and frequency in axons with the diameters of $1\mu m$, $2\mu m$ and $5.7\mu m$ (injury epicenter: node 10). Spheroid's length $=1\mu m$, CLR=0.42 and LADR=0.75. Nodes of Ranvier are the most sensitive part along the axons that formation of even one relatively large spheroid (SDR=20.3) in those regions can cause a complete blockage of the transmission of neural messages.

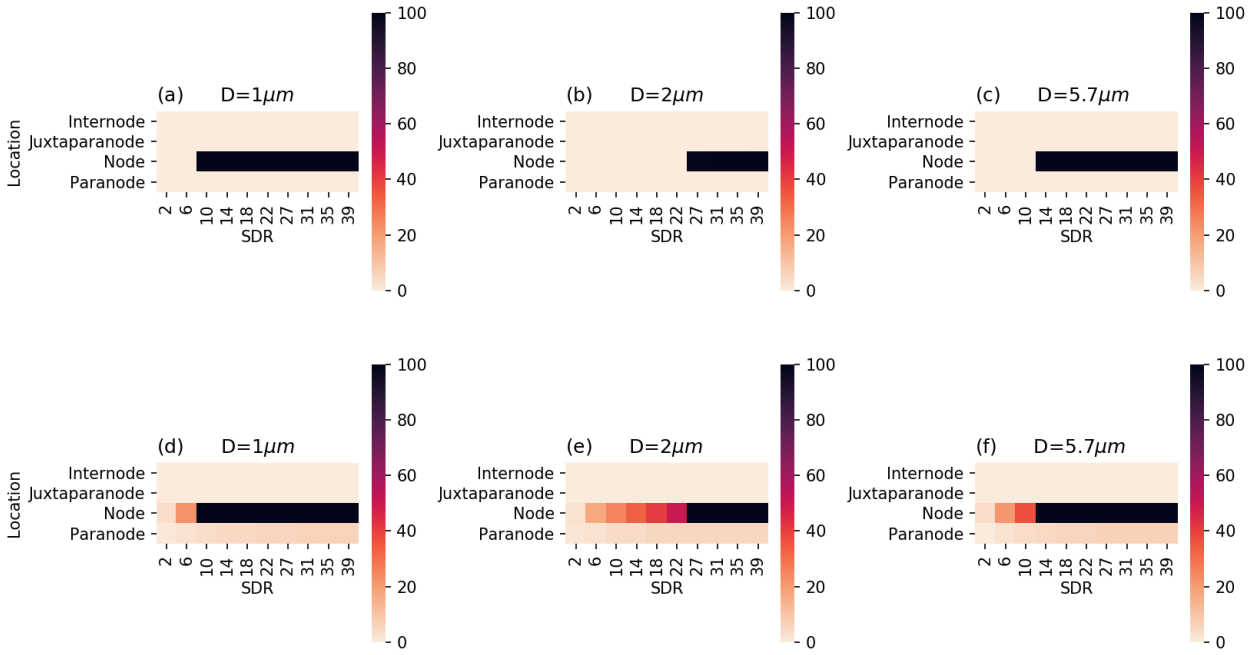

Figure 5.6: Percent reduction in membrane potential amplitudes (a, b, c) and conduction velocities (d, e, f) because of variations in spheroid location and SDR (injury epicenter: node 10) in axons with the diameters of $1\mu m$, $2\mu m$ and $5.7\mu m$. Spheroid's length $=1\mu m$, CLR=0.42 and LADR=0.75, Frequency=1. When located in nodes of Ranvier, even small or medium size spheroids (SDR<20, length $=1\mu m$) can disrupt action potential propagation.

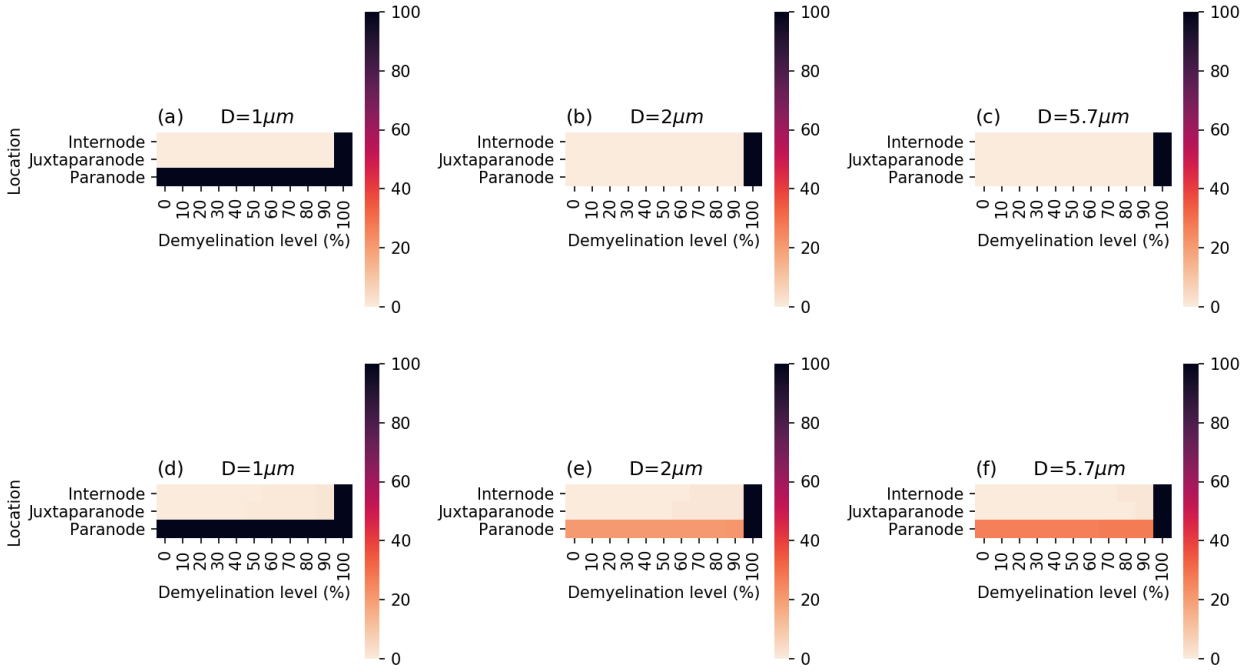

Figure 5.7: Percent reduction in membrane potential amplitudes (a, b, c) and conduction velocities (d, e, f) because of variations in spheroid location and demyelination levels (injury epicenter: node 10) in axons with the diameters of $1\mu m$, $2\mu m$ and $5.7\mu m$. Three spheroids with the length of $1\mu m$ and SDR value of 20.3 (CLR=0.42 and LADR=0.75) were modeled in different myelinated axonal regions. Paranodal regions were most sensitive to spheroid formation and conduction disruption. Spheroid formation and mild demyelination reduced conduction velocity in all axons however, action potential propagation was blocked when all three spheroids were completely demyelinated.

Table 5.4: Descriptive statistics of spheroids' measures from human brain tissue

		Group 1	Group 2	Group 3	Group 4
AxonD (μm)	mean	0.404	0.577	0.779	1.245
	std	0.068	0.047	0.069	0.405
	min	0.244	0.488	0.660	0.920
	50%	0.418	0.590	0.787	1.120
	max	0.487	0.653	0.900	2.780
SDR	mean	6.196	5.108	4.521	4.077
	std	2.469	4.671	2.115	2.718
	min	3.588	3.159	2.261	1.688
	50%	5.429	4.292	3.623	3.311
	max	16.503	38.969	10.349	18.184
Volume (μm^3)	mean	19.818	59.473	77.380	211.466
	std	31.801	247.182	108.383	533.385
	min	4.147	4.023	7.590	7.723
	50%	11.194	19.521	36.792	62.277
	max	233.689	1931.382	497.585	3926.528
Area (μm^2)	mean	7.523	18.149	24.071	47.900
	std	7.012	52.152	24.921	74.660
	min	2.871	3.506	3.283	5.983
	50%	5.099	9.232	14.046	21.464
	max	46.726	410.294	114.880	500.212
CLR	mean	0.216	0.202	0.193	0.193
	std	0.104	0.128	0.127	0.149
	min	0.047	0.017	0.030	0.011
	50%	0.188	0.184	0.170	0.158
	max	0.500	0.663	0.600	0.820
LADR	mean	0.801	0.785	0.765	0.742
	std	0.078	0.074	0.074	0.080
	min	0.620	0.619	0.588	0.546
	50%	0.806	0.793	0.773	0.741
	max	0.935	0.921	0.951	0.892
3D Feret Diameter (μm)	mean	6.432	9.670	11.699	15.329
	std	2.736	6.429	5.614	9.078
	min	3.515	4.250	3.794	5.438
	50%	5.444	7.176	10.988	13.490
	max	18.885	38.904	29.100	57.302

5.5 Discussion

The proper functioning of axons is vital for the transmission of neural signals. Spheroid formation is one of the early and common axonal pathologies in MS, TBI and SCI [219]. Although recent 3D microscopy studies have shown that the cross-section shape and diameter of individual axons may vary along their length [248], large or sudden changes in

the diameter of axons may cause functional disruption [79, 226]. While there have been some preliminary investigations into the effect of spheroids on neurophysiology, this study expands the work to include the interaction of normal variation in axon morphology with the presence of spheroids.

These results of this paper agree well with existing studies on spheroids suggesting that the larger the spheroids are, the stronger their effects are on action potential propagation [79, 226]. However, the studies on unmyelinated axons [226, 227] indicate that other than the spheroid's diameter, the geometry of spheroids and the rate of change in diameter plays a key role in determining if a spheroid blocks conduction. The results of our morphological analysis show that spheroids' geometry are very different and there is a wide variation in values of spheroid tapering-related parameters (CLR, LADR, SDR) in damaged CNS axons (Table 5.4). Although the change in CLR and LADR values in our simulation of myelinated axons changed the dynamics of signal propagation in some cases (see Figure 5.4), the results of stepwise regression analysis (Figure 5.3) indicate the relative effects of CLR and LADR values on action potential amplitude were smaller than the other parameters within the range of values studied in this paper.

Different axonal structures may be damaged following mechanical trauma, and several mechanisms trigger secondary injury. Among them, myelin damage [143, 181, 249] and spheroid formation have been observed in numerous in-vivo studies, and many experimental treatment strategies are aimed at mitigating the effects of these structural changes [93,157,158,188]. However, the spheroid formation can occur with demyelination or separately. Although demyelination is the hallmark of MS, recent studies on animal models of experimental autoimmune encephalomyelitis (EAE) shows that axonal spheroids may appear in axons with an intact myelin sheath [224]. On the other hand, several other studies reported myelin injury in swollen regions of axons following trauma [250] or in other CNS diseases. Depending on the type and severity of the injury, one or more spheroids may appear along the axon [82, 251].

Previous computational studies suggest that the functional effects of single spheroids located in internodal regions of myelinated axons are limited, and the diameter of spheroids should be beyond observed physiological values in experimental studies [79] to see significant effects. Our results indicate that as long as some extent of the myelin sheath covers the spheroids, single spheroids in internodal regions did not block signal propagation within the range of values studied in this research. Similar behaviour was seen for the spheroids in the juxtaparanodal regions. However, the results of the current study suggest that paranodal regions are far more sensitive to spheroid formation than juxtaparanodal and internodal regions. Previous observations indicate that paranodal regions are more susceptible to myelin injury [92,93,252] and spheroid formation following trauma. Studies on MS patients reported that paranodal axoglial junctions might become damaged in the normal-appearing white

matter of the brain [253]. Also, animal models of MS show formation of axonal spheroids in paranodal regions [224].

In contrast with internodal and juxtaparanodal regions, the results of our computational sensitivity study showed that a single medium-sized spheroid (L=3μm and SDR=20.3) with intact myelin sheath in the paranodal region was enough to block signal propagation in all axons with the diameters of 1μm, 2μm and 5.7μm. Demyelination in wide regions of the axon may slow down action potential propagation or block neural signals altogether. In particular, myelin damage in paranodal regions has a substantial effect on the axon's ability to conduct signals [37, 241]. Although it is reported that some completely demyelinated axons can still propagate signals [79, 254], when myelin injury and axonal swelling occur in non-nodal regions of the axon, their combined effect may block signal propagation. Our results (Figure 5.7) showed that even a thin layer of the myelin sheath covering the swollen region of the axon could significantly support action potential propagation. However, when spheroids are completely demyelinated, the axon's ability to propagate action potentials reduces substantially and action potentials are blocked.

Nodes of Ranvier are essential for generating action potential in myelinated axons, and any damage in these regions may block signal propagation. Previous literature suggests that Ranvier nodes experience high amounts of stress following diffuse brain injury [144] as myelin sheaths do not protect them. In MS patients, axonal spheroids may appear at nodes of Ranvier in normal-appearing white matter tissue [253]. This research indicates that nodes of Ranvier are the most sensitive region along axons to the spheroid formation. Our results show that when there were three small spheroids (SDR=1.7 and L=3μm) in three consecutive nodes of Ranvier, action potential was blocked in all axons. In our simulations, only one spheroid (CLR=0.42, LADR=0.75) with the SDR of 10 and length of 1μm in a node of Ranvier was enough to block signal propagation in the small axon (D=1μm) and substantially reduce conduction velocity in the larger axons (D= 2μm and 5.7μm)

Although there is a normal variation in the size of axons, their susceptibility to injury might be different. Previous studies have reported a 100 fold difference in the diameter of axons in the central nervous system ranging from 0.1μm to $> 10\mu m$ [34]. The diameter of axons may increase over time [255] to facilitate action potential propagation and communicate at higher rates [34]. The results of our morphological analysis of human brain samples indicate that there was a 10 fold difference in the normal diameter of axons for identified spheroids ranging from 0.24μm to 2.78μm. Observations in previous studies show that small axons are more susceptible to spheroid formation and the number of spheroids that appear along axons following strain injury has a inverse relationship with the axon/bundle diameter [87]. Previous models [79] suggest that larger spheroids are needed for blocking signal propagation in axons with larger diameters and increasing the axonal base diameter recovered conduction for the same spheroid size in computer simulations. In our study, the smallest axon (D=1 μm) was most sensitive to the spheroid formation. However, although

larger spheroids in terms of the absolute value of spheroid diameter were needed to block action potentials in axons with the diameters of $2\mu m$ and $5.7\mu m$, the overall relationship between the normal axonal diameter and the minimum SDR value needed for blocking AP propagation was not linear (Figure 5.6); and a linear regression relating normal axonal diameter and spheroid diameter could not predict the amount of functional disruption in our models. However, analyzing the results of our sensitivity study revealed that the average amounts of reduction in action potential amplitude and conduction velocity were increased as the value of SDR increased for each axon regardless of other spheroid parameters (CLR, LADR, length, frequency, etc.). Our morphological measurements (Table 5.4) showed that while the median values of spheroids' volume were higher for larger axons, the median SDR values had a reveres relationship with axonal diameter. The median values of SDR for the identified spheroids in human brain tissue were 5.42, 4.29, 3.62 and 3.11 for the axons in groups 1, 2, 3 and 4, respectively. This suggests that as the diameter of axons increases, the SDR value decreases, which might be a protective mechanism for larger axons to maintain conduction.

Therefore, in addition to what was suggested in previous studies [226] that spheroid tapering is an important factor for determining the dynamics of signal propagation in unmyelinated axons, the results of this study suggest that spheroid location and SDR are the two most important parameters for predicting signal propagation in the myelinated axon. However, in this study, we focused on investigating the propagation of low-frequency signals and single action potentials in myelinated axons. In many of our simulations, there was only a marginal reduction in the amplitude of action potential signals post-swelling; however, the reduction in conduction velocity was sizable. Previous research has shown that neurons may fire at different rates (from 1Hz to >100Hz) [34]. Recent computational studies on unmyelinated axons [226] have shown that axonal spheroids may act as a filter and change the frequency of spike trains or even reflect action potential signals in the opposite direction. This may completely change the information content being transmitted between neurons and cause functional disabilities. Therefore, further studies need to be done to explore the relationship between different spheroid parameters and the changes in spike train frequency in myelinated axons. This observation could suggest a functional target for detecting subtle axon damage in white matter before demyelination occurs. Moreover, although the general notion is that axons are considered as long cylinders with an almost constant circular cross-section along their length, recent observations with 3D electron microscopy indicate that the cross-section of axons have an oval shape and their diameters change [248]. These geometrical differences need to be taken into account in future computational models when studying functional effects.

A key challenge in studying diseases such as MS, TBI and SCI and linking observed histological changes to functional implications is that we are limited to studying deceased human subjects or replicating human disease in animals with different biophysical and

morphological characteristics. Coupling pathological observations from human tissues with computational models of axonal function provides a unique tool to quantify the potential impact of changes in the axonal structure on function. We expect this research to lay the quantitative foundation for new potential functional markers of white matter tissue damage and provide further insights into how axonal spheroids may affect function. Technologies such as EEG, MEG, and embedded electrode arrays directly measure neuron function. However, they depend on quantitative metrics to effectively differentiate a diseased or injured condition. This study's results may help in augmenting our understanding of the relationship between clinical signals from these technologies and patients' symptoms. This work will lay the foundation for new research to link the structure-function relationship of injured CNS axons and provide a pathway to integrate advanced technologies to identify subtle CNS damage that may not be detectable with traditional imaging techniques.

Chapter 6

Discussion

6.1 Discussion

Computational modelling of the nervous system provides a complimentary tool to overcome some of the limitations of current animal and in-vitro models of neurological diseases and injuries. In recent years, the interest of the neuroscience community in employing biophysical models has risen as they let us change and study the effects of individual injury parameters on signal conduction, and they can be cheaper and faster than animal studies. Increased computational power has facilitated large scale simulations and increasingly complex and accurate model development [256, 257]. Computational models allow us to comprehensively explore and narrow the parameter space to experimentally test treatments with the highest promise and minimize the number of animals involved in those studies. These models also facilitate the exploration of mechanisms of action that result in experimentally observed phenomena. In this thesis, we employed a series of computational models to investigate the relationship between different neuropathologies reported in human patients and animal models of TBI, SCI and MS (chapters 3, 4, 5) on axonal function. The objective of these studies was to develop accurate models that balance complexity with computational costs.

In mammals, white matter tissue mainly consists of oligodendrocytes with their myelin sheaths and axons (chapter 1). Unlike unmyelinated axons, where sodium channels (Nav1.2) are distributed along the axon, the inhibitory effects of myelin sheaths in myelinated axons result in the clustering of sodium channels (Nav1.6) at the nodes of Ranvier [258]. This unique structure makes myelinated axons conduct signals faster and more energy-efficiently which is required for fast cognitive, motor and sensory function. The integrity of myelin layers and myelin-axolemma junctions around the nodes of Ranvier are essential for maintaining axonal ionic balance, the proper function of neurons, and action potential generation. Demyelination (Chapter 3 and 5) and axonal swelling (Chapter 5) are hallmarks of axonal injury in TBI [82, 252], SCI [143], MS [162], ischemic stroke [259] and other neurological diseases which are associated with functional disruption and slow information processing in patients [252, 260–262]. Nodal and paranodal disruptions have been reported in mod-

els of auto-immune diseases [263–265] and previous experiments showed that the myelin sheath in the paranodal and juxtaparanodal regions experience high stress levels following strain injury [89, 171] and TBI [252]. These events may damage the myelin layers in those regions, increase the periaxonal gap (the space between the axolemma and myelin sheath) and expose the fast potassium channels located in juxtaparanodal regions. Although the relative length of the paranodal and juxtaparanodal regions is short compared to length of the internodal regions (<5%) [37], the results of our study (chapter 3) suggest that even subtle myelin abnormalities in those regions may have sizable effects on action potential amplitude and velocity. Previous research indicates that the susceptibility of axons of different calibre to mechanical trauma and myelin damage is different. Our results reinforce the interaction of axon calibre and myelin damage on the extent of functional disruption. Studies on TBI models of mice showed that paranodal disruptions have significant effects on action potential velocity three days post injury. Function recovery was observed in injured mice at two weeks post injury - which aligns with the time frame required for remyelination [252]. The results of this thesis suggest that myelin detachment in the paranodal and juxtaparanodal regions has a bigger effect on membrane potential and conduction velocity than myelin retraction. Similar to what was demonstrated in Chapter 5, our myelin injury model suggests that even a thin layer of myelin can be very beneficial in supporting axons in conducting action potentials. Interestingly, recent studies [266] have shown that neuronal activity in demyelinated axons promotes oligodendrocyte differentiation and remyelination. Hence, early interventions to stop or reduce demyelination in damaged axons not only help some axons continue signal propagation (chapter 3 and 5) but may also indirectly increase the recovery of axons following the acute phase of injury because of the remaining activity of neurons.

Focal spheroid formation is another hallmark of axonal injury in neurological abnormalities including TBI [78, 219, 223], SCI, Alzheimer's [220, 221], Parkinson's [222], and MS [224,225]. Axonal spheroids may appear because of structural changes in the axolemma, breakage of microtubles and local accumulation of neuronal cargo in different parts of the axon or over-activation of glutamate receptors [267]. Previous experiments have reported that the diameter of these spheroids may be up to 30 times that of the normal axonal diameter [82]. A sequence of spheroids may appear along a damaged axon. However, spheroids may be much smaller depending on the type and the severity of the injury. It has been shown that axonal spheroids and the changes in axonal diameter affect the integrity of myelin layers locally [268] and may disrupt action potential propagation in myelinated [79] and unmyelinated [226] axons.

To study the effects of spheroids' geometrical variations, demyelination level, location and frequency of spheroid formation on action potential generation we developed a model of spheroid formation and performed a comprehensive study on axons with the diameters of 1 μm, 2 μm, and 5.7 μm (chapter 5). However, in order to study subtle abnormalities that

may cross different axonal structures (node, paranode, etc.) such as spheroids in different computational models, high geometrical resolution is needed. The conventional method to increase geometrical resolution in NEURON is to increase the number of segments. However, this results in increasing the computational cost and time of running simulations significantly which becomes a challenge in simulation of large axonal networks. On the other hand, when simulating the same abnormality in neurons with different size, the number of segments in each structure may vary from one neuron to another neuron. It confounds computational results and makes comparison of results challenging. We employed a novel approach (chapter 4) to increase the geometrical resolution in single axons and large axonal networks that is also applicable to all existing myelinated and non-myelinated neuronal models in NEURON. The new model may reduce the computational cost by up to 99% compared to the conventional methods (increasing segments) and makes the comparison of results among axons with different calibers more consistent. Employing the new model allowed us to extend the boundaries of spheroids to different axonal structures and change the electrophysiological and morphological properties of the spheroids as needed.

Our results (chapter 5) indicate that the relationship between axonal function and different spheroid's parameters is non-linear. The results of the current study suggest that myelinated axons of different size respond differently to spheroids. Among all studied parameters, spheroid diameter ratio (SDR), location and demyelination level are the main predictors of functional disruption after injury in myelinated axons. Previous literature reported axonal spheroids in nodes of Ranvier in normal-appearing white matter tissue of MS patients [253] and indicate that paranodal regions are more susceptible to myelin injury [92,93,252] and spheroid formation following trauma. The results of this thesis indicate that nodes of Ranvier and paranodal regions are the most sensitive regions along axons to the functional disruptions following spheroid formation. This suggests that more targeted treatments need to be developed that focus on these two regions.

Animal models are the traditional method for studying brain and spinal cord injuries. Although non-human mammals and humans share many common physiological properties, the important differences in the geometry of their brain, craniospinal angle, white to gray matter ratio and the number and size of spinal tracts may lead to substantial differences in behavioural and histopathological responses to the same injury type and severity level from species to species [269–273]. For example, previous literature suggest that smaller animals have a tendency to have smaller axons and larger animals present larger axonal diameters in their spinal cords [274–276]. Past studies report that the average diameter of axons in the pyramidal tracts of rats ranges from 0.72 μm [277,278] to 1.18 μm [279] while 90% of axons are smaller than 1.5 μm [276]. However, cats have larger axons (0.25 μm - 23 μm) in their pyramidal tract [275] while the majority of axons are less than 2 μm in diameter [275,280]. The axonal diameter in pyramidal tract of monkeys ranges from 0.04 μm to 9.48 μm [281] whereas, the diameter of axons in the pyramidal tract of human spinal cord varies from 0.3

μm [282] to 20 μm [283]. However, it is important to note that experimental limitations and histological distortions may have confounded measurements as an axon with the diameter of 23 μm in cats is quite large even for humans and monkeys [276].

Axons with different diameters may respond differently to injuries and diseases. Throughout this thesis, variation in axonal calibre was included to quantify the interaction of axon diameter with damage parameters. In this thesis (chapter 5), we collected and analyzed confocal microscopy images from post-mortem human brain tissue of four MS and infarct patients. Following identification and labeling spheroids in myelinated axons and performing image processing, a new data-set of morphological features of the spheroids (including diameter, Feret diameter, volume and area) in the human brain was created. Our results suggest that there is a significant difference between the morphological features of these spheroids such as SDR ratio (the spheroid's maximum diameter to axonal diameter ratio) and spheroids' volume among axons with different diameters. Our analysis revealed that although the size of absolute value of the maximum spheroid's diameter value in larger axons might be larger than the smaller axons, there is an inverse relationship between the SDR value and the normal axonal diameter in damaged axons in the human brain tissue. Therefore, it is important to perform injury models across a wide range of axons to get a more comprehensive understanding of the relationship between axonal morphological features and injury parameters.

Although there are important ethical and economical issues around use of animals in studying the brain and spinal cord diseases, due to very complex structure and function of the nervous system the use of animals models is still vital. In the past two decades, new treatments and neuroprotective drugs were developed that showed promising effects in animal models of brain injury; however, all failed in Phase II or Phase III clinical trials [269]. The efficacy and effectiveness of drugs and therapies depend on the electrophysiological and morphological properties of target cells. Therefore, the choice of animal model is a very important issue to consider for maximizing the possibility of finding an effective treatment for SCI and TBI in humans. Rats and mice are the most commonly used animals for SCI research [276] due to access and cost considerations as well as the extensive available literature on the their anatomical and functional analysis related techniques [284–286]. However, there are substantial differences in terms of axonal size, neuroanatomical, neurophysiological and behavioral characteristics of of these animals from humans [276, 287, 288]. The results of Chapters 3 and 5 of this thesis showed that the mechanism of injury might depend on axonal diameter. In addition, the results of Chapter 3 suggest that the efficacy of treatments such as potassium channel blockers may vary in axons of different calibers. In our simulations, when axons were damaged by both myelin retraction and myelin detachment, potassium channel blockers were more effective (54% and 34% increase in membrane potential compared to pretreatment values in axons with diameters of $1\mu m$ and 2 μm, respectively). However, blocking fast potassium channels in the large axon (D = 5.7 μm)

could not increase membrane potential by more than 2% at the epicenter of injury, and action potential propagation was not recovered in distal nodes. Therefore, it is important to not only consider electrophysiological difference in neurons but also take morphological differences into account when developing and testing new treatments and drugs following neurological injuries.

In agreement with previous studies [288, 289], the results of this thesis supports using of nonhuman primates (NHPs) in TBI and SCI studies. NHPs share more physiological features with humans and the size and variability [276,290] of their axons are more similar to humans than small mammals. This may facilitate the successful translation of new therapies to humans and minimize the risk of side effects. However, not all NHPs are the same. Considering the similarities in size, pharmacodynamics, electrophysiological properties of blood-brain barrier (BBB) and recovery time frames, the macaque monkey is a more suitable candidate for animal studies than other NHPs [288]. While small animal models continue to be useful for making mechanistics observations and to understand fundamentals of biological processes, our work supports the suggestion that larger animal models should be used in preclinical trials as an intermediate step before human studies [269, 288, 289].

Previous studies suggest that there might be some sex-based differences in outcomes after traumatic brain injury in animals and humans [291, 292]. Although there are some observations indicating that females may have higher concussion rates [293–295] and worse outcomes than males following sport injury [296–298], the effects of sex on TBI and SCI patients in clinical settings is not completely understood yet [292, 299, 300]. Factors like the differences in metabolism, brain function and pre-injury comorbidities may affect functional outcome post injury [269] in each sex. Experimental evidence suggest that the female sex hormone, progesterone, has neuroprotective effects and may improve neurological function following injury in humans [292, 299, 301]. However, recent *in vivo* studies revealed that axons from human females have smaller diameter than those from males (in the absence of progesterone) and also showed substantially more spheroids post mechanical injury [298]. Studies using diffusion MRI have shown that the mean axonal diameter in females is smaller than males in different sections of the human corpus collosum [302] and the white matter volume is larger in males than females [303]. Previous studies have shown that the smaller axons are more vulnerable to stretch injury, myelin damage and spheroid formation. Our results also indicate that smaller axons are more sensitive to spheroid formation and experience disruption in their function (Chapter 5). Therefore, progesterone might be one the natural solutions that evolved to protect small axons of females from brain and spinal cord injury. However, it is important to note that since most of the animal studies are done with males, it is vital to include more female animals in future investigations and study the relationship between axonal size, injury parameters, sex and the effectiveness of different treatments.

Although animal studies are useful in elucidating the short term effects of new drugs in living organisms, the long term effects of new drugs when humans use them may be different from the short term effects. In addition, animal models are limited because of the number of outcome measures that can be measured during the course of a study. The injury process may be affected by several factors such as immune system response, genetic predispositions, regeneration, etc. Biophysical computational models combined with animal experimental models of the brain and spinal cord injury provide a great opportunity to study the effects of the injury mechanism on neural function and highlight potential targets for treatments. These models may also provide a means to translate results from animal studies onto simulated human scale models and help in performing more targeted and effective preclinical trials.

Genetic, biochemical and neuroimaging biomarkers can provide important information in the diagnosis of traumatic brain and spinal cord injury. Although extensive research has been done to identify different biomarkers for evaluation of TBI and SCI [304–309], there is still a need for developing new clinically relevant and common biomarkers in humans and animals for proper and timely translation of animal studies to humans [269]. Specific physiological, molecular and biochemical biomarkers such as Alpha-II-spectrin [305,306], aldolase C (ALDOC), brain lipid binding protein (BLBP), astrocytic phosphoprotein (PEA15) and glutamine synthetase (GS) [310] help in monitoring and proper assessment of the severity of injury and the efficacy of treatments [269]. With the recent advancement in diagnosing, monitoring and neuroimaging technologies such as functional MRI, positron emission tomography (PET) and Magnetoencephalography (MEG), it is possible to measure different biochemical, anatomical, functional and genetic biomarkers simultaneously to get a more comprehensive overview of the state of the injury in animals and humans at a time. The use of multi electrode arrays (MEAs) is becoming increasingly more prevalent within the neuroscience research community to monitor neuronal function in animal studies in different stages of injury [311–314]. However, their application in clinical setting is limited as they are highly invasive. On the other hand, techniques such as MEG with very high spatial and temporal resolution could assist in identifying abnormal localized function non-invasively. However, identifying the most important structural and electrophysiological predictors of function is important for finding new therapeutic targets. The use of conventional mathematical methods such as principle component analysis (PCA) to identify the most important parameters that affect the injury outcomes combined with novel artificial intelligence and machine learning algorithms to analyze neuroimaging data sets and electrophysiological recordings may help in identifying new biomarkers for early detection of pathologies and selecting more specific treatments.

Although different drugs and treatments have been developed to recover action potential propagation in injured axons in animal and *in vivo* studies, most of them have not yet translated into clinical therapies for human injuries [269,315]. Following injury, several structures

may be damaged and cause functional disruption. The results of the current study suggest that the extent and effects of each injury parameter on axons with different morphological and electrophysiological properties might be different even in the same species. Therefore, in order to develop new effective treatments for patients with brain and spinal cord injury, a multifaceted approach to use multi-functional agents and/or combination therapies should be used [269,316,317]. A combination of the application of pharmaceutical agents, stem cell therapy and other approaches such as electrical stimulation with complementary targets and effects may have more significant neuroprotective and/or neurorestorative effects. In addition, testing new drugs and methods developed based on animal models of rodents in preclinical studies with NHPs help in reducing the potential side effects and maximizing the chance of successful translation of these treatments in clinical trials in humans.

6.2 Recommendations for future work

Although the imaging and electrophysiological recording technologies have advanced in the past few years, there is currently no recording data from single cells that compare the axonal function before and after myelin damage or spheroid formation in the central nervous system. Therefore direct quantitative comparison between the results of this study and experiments on damaged axons is not possible. Instead, comparing the trends and the overall behaviour of axons with reported observations in experiments of axonal injury might be a better option to study the underlying relationship between structural changes and functional disruptions. However, it is important to develop new protocols and perform new experiments to measure the structural and related functional changes more accurately. In recent years, new methods have been developed to obtain stem cells from humans and differentiate them into neurons *in vitro* by overexpression of Neurogenin-2 (Ngn2) [298, 318]. Moreover, dynamic stretch injury of cultured axons have been done successfully in several studies [161, 298, 319]. Advanced imaging technologies such as transmission electron microscopy (TEM) and serial block-face scanning electron microscopy [320] provide high resolution images that can be used to study ultrastructural changes of axons before and after injury. In addition, with the recent advancement in fine microelectrode arrays, complementary metal-oxide–semiconductor (CMOS) nanoelectrode arrays (CNEA) [321] and acquisition systems [322] real-time and high-precision extracellular and intracellular recording from cultured neurons has become possible.

The simulations and modified models used in this study were based on the geometrically accurate models of motor neuron fibers developed by McIntyre and colleagues [2]. The models had a double cable structure to take the myelin sheath and other membrane mechanisms into account. The nodal diameter of the simulated fibers were $0.7\mu m$, $1.4\mu m$, $1.9\ \mu m$ for the axons with the diameters of $1\mu m$, $2\mu m$ and $5.7\mu m$, respectively. Although these values are within the reported ranges for axonal diameter values in the human CNS [290] and

what we observed in our morphological analysis of the human brain (chapter 5), the axonal diameter ranges from 0.1 μm [34] to 20 μm in the human CNS [283]. Therefore, developing more accurate and specific axonal models that incorporate more membrane mechanisms and simulate electrochemical processes inside neurons for different regions of the CNS may help to improve the accuracy of the predictions. Further, there may be sex differences in axon calibre range or distribution as well as differences in structures such as channel distributions. Through this work we see the important functional implications of subtle changes in axonal structure or injury. It will be important to ensure biophysical models such as the one used in this study, fully represent the diversity of human axonal morphology.

The focus of the current thesis was on investigating the changes in propagation of single action potentials in damaged axons. However, axons in different CNS regions or in the same axonal bundle/tract (e.g corticospinal tract in the spinal cord) may have different calibers and fire at higher rates to encode and transmit the information to other neurons in the network [34]. Moreover, the firing frequency of axons may vary in different animals. For example, previous studies have reported that cortical fast-spiking neurons may fire at 453 Hz in humans whereas the neurons in the association cortex (entorhinal) of mouse could generate action potential at much lower frequencies (342 Hz) [323]. It is shown that axonal injuries such as spheroids may act as low-pass filters in non-myelinated axon [226] and disrupt the proper transmission of neural messages. Therefore, it is important to investigate the effect of the abnormalities studied in this thesis on the propagation of high frequency signals in myelinated axons of different caliber to get a more comprehensive understanding of the structure-function map in damaged axons in different animals.

Currently, magnetic resonance imaging (MRI) is one of the first diagnostic procedures done following admission of TBI or SCI patients to the hospital. Although conventional MRIs are very useful for highlighting structural damage to the CNS tissue, the amount of information one can get regarding functional status of damaged axons is minimal. On the other hand, more advanced technologies such MEG, high-resolution MRI and DTI (Diffusion Tensor Imaging) Tractography [324] have become more available and allow better measures of the post-injury functional, structural and connectivity changes of axons. Correlating brain structural changes with function and scaling the predictions in larger networks of axons can be the next front for understanding the mechanisms and effects on injury.

6.3 Concluding remarks

During this project we employed different advanced numerical methods and computational models to characterize morphological changes in damaged axons and study the effects of some of most common axonal injuries on signal propagation in the central nervous system. To this end, the key contributions and findings of this thesis can be summarized as follows:

- Developing a biophysical model of axons with diameters of $1\mu m$, $2\mu m$ and $5.7\mu m$ to study the effects of paranodal and juxtaparanodal myelin injury and identifying the axonal structures with highest impact on membrane potential and conduction velocity in intact axons. Our results show that length of nodes of Ranvier (which are covered with high number of sodium channels) and axonal diameter are the most important factors in predicting the amplitude and velocity of action potentials in intact axons, respectively. Therefore, precise measurements of morphological and electrophysiological properties of nodes of Ranvier and axonal diameter are necessary for improving the accuracy of predictions in intact and damaged axons.In addition, using a single generic axon model (as many previous studies have) to simulate damage will not fully capture the varied response of normal axons to injury.

- Quantifying the relative effects of myelin retraction and myelin detachment in paranodal and juxtaparanodal regions on signal propagation. The results of our damage study indicate that myelin detachment was the key parameter for prediction of the variation in axonal dysfunction after subtle myelin injury in small and large axons. Our results also show that axonal caliber affects the response of axons to the severity and type of myelin retraction and detachment injury with larger axons being more affected by damage in the juxtaparanodal regions. Therefore, pharmacological agents and neuroprotective treatments may need to target different regions of small and large axons following myelin damage.

- Studying the relative efficacy of potassium channel blockers on recovery of action potentials in damaged axons with different diameters and identifying the optimal targets for potassium channel blockers. Our results indicate that potassium channel blockers were most effective in small diameter (D= 1 μm and 2 μm) axons but less effective in larger axons (D= 5.7 μm). Moreover, the efficacy of potassium channel blockers varied based on the nature and combination of different injuries. This could have implications in treatment efficacy and scaling treatments from small animal models to humans.

- Developing and validating a novel approach for increasing the geometrical resolution in biophysical models of myelinated and unmyelinated axons in NEURON that reduces computational cost by up to 98% compared to the conventional methods. This will enable larger and more diverse simulations of neural injuries in an efficient manner.

- Developing a new dataset of human brain spheroids by identifying and labeling axonal spheroids in confocal microscopy images from post-mortem human brain tissue and performing accurate morphological measurements by developing advanced and customized diameter measurement algorithms. Our results indicate that there is a significant difference in the distribution of spheroid morphological features such as

SDR, volume, area and Feret diameter across axons with different calibers. The results of this study show that the median value of SDR (the spheroid's maximum diameter to the axon's normal diameter ratio) was higher for smaller axons than the axons with larger diameters.

- Developing a novel biophysical model of axonal spheroids and studying the functional effects of spheroids on signal propagation that resulted in identifying the most important spheroid parameters for predicting the degree of functional disruption in axons of different diameter. The results of this thesis indicate that the relationships between spheroid morphological properties, axonal caliber and action potential amplitude and velocity are nonlinear. The spheroids' SDR and demyelination level are the two leading predictors of the amount of post-injury variation in membrane potential in axons with the diameter of 1 μm, 2 μm and 5.7 μm. However, conduction velocity is more sensitive to the spheroids' location and demyelination level. Nodes of Ranvier and paranodal regions are the most sensitive regions along the length of axons to spheroid formation and might be therapeutic targets for restoring action potential signals following injury.

Bibliography

[1] Sterratt, D., Graham, B., Gillies, A. & Willshaw, D. *Principles of Computational Modelling in Neuroscience* (Cambridge University Press, Cambridge, 2011).

[2] Mcintyre, C. C. & Grill, W. M. Extracellular Stimulation of Central Neurons : Influence of Stimulus Waveform and Frequency on Neuronal Output Extracellular Stimulation of Central Neurons : Influence of Stimulus Waveform and Frequency on Neuronal Output. *Journal of neurophysiology* **88**, 1592–1604 (2002).

[3] Danner, S. *Computer simulation of electrically stimulated nerve fibers in the human spinal cord* (2010).

[4] Feigin, V. L. *et al.* Global, regional, and national burden of neurological disorders, 1990–2016: a systematic analysis for the global burden of disease study 2016. *The Lancet Neurology* **18**, 459–480 (2019).

[5] Mai, J. K. & Paxinos, G. *The human nervous system* (Academic Press, 2011).

[6] Herculano-Houzel, S. The human brain in numbers: a linearly scaled-up primate brain. *Frontiers in human neuroscience* **3**, 31 (2009).

[7] Veening, J. G. & Barendregt, H. P. The regulation of brain states by neuroactive substances distributed via the cerebrospinal fluid; a review. *Cerebrospinal Fluid Research* **7**, 1–16 (2010).

[8] Xie, L. *et al.* Sleep drives metabolite clearance from the adult brain. *science* **342**, 373–377 (2013).

[9] Iliff, J. J. *et al.* A paravascular pathway facilitates csf flow through the brain parenchyma and the clearance of interstitial solutes, including amyloid β. *Science translational medicine* **4**, 147ra111–147ra111 (2012).

[10] Iliff, J. J. *et al.* Brain-wide pathway for waste clearance captured by contrast-enhanced mri. *The Journal of clinical investigation* **123**, 1299–1309 (2013).

[11] Madden, M. E. Diagnostic imaging of cerebrovascular injury. *Radiologic technology* **79**, 535MR–549MR (2008).

[12] Luders, E. *et al.* Positive correlations between corpus callosum thickness and intelligence. *Neuroimage* **37**, 1457–1464 (2007).

[13] Morton, S. M. & Bastian, A. J. Cerebellar control of balance and locomotion. *The neuroscientist* **10**, 247–259 (2004).

[14] Zee, D. S., Leigh, R. J. & Mathieu-Millaire, F. Cerebellar control of ocular gaze stability. *Annals of Neurology: Official Journal of the American Neurological Association and the Child Neurology Society* **7**, 37–40 (1980).

[15] Koziol, L. F., Budding, D. E. & Chidekel, D. From movement to thought: executive function, embodied cognition, and the cerebellum. *The Cerebellum* **11**, 505–525 (2012).

[16] Akshoomoff, N. A. & Courchesne, E. Erp evidence for a shifting attention deficit in patients with damage to the cerebellum. *Journal of Cognitive Neuroscience* **6**, 388–399 (1994).

[17] Nattie, E. Co2, brainstem chemoreceptors and breathing. *Progress in neurobiology* **59**, 299–331 (1999).

[18] Lang, I. M. Brain stem control of the phases of swallowing. *Dysphagia* **24**, 333–348 (2009).

[19] Jones, B. E. Arousal systems. *Front Biosci* **8**, 438–51 (2003).

[20] Smith, L. H. & DeMyer, W. E. Anatomy of the brainstem. In *Seminars in pediatric neurology*, vol. 10, 235–240 (Elsevier, 2003).

[21] Nógrádi, A. & Vrbová, G. Anatomy and physiology of the spinal cord. In *Transplantation of neural tissue into the spinal cord*, 1–23 (Springer, 2006).

[22] Nicholas, D. S. & Weller, R. O. The fine anatomy of the human spinal meninges: a light and scanning electron microscopy study. *Journal of neurosurgery* **69**, 276–282 (1988).

[23] Hyman, S. E. Neurotransmitters. *Current biology* **15**, R154–R158 (2005).

[24] Lodish, H. *et al.* Neurotransmitters, synapses, and impulse transmission. In *Molecular Cell Biology. 4th edition* (WH Freeman, 2000).

[25] Kandel, E. R. *et al. Principles of neural science*, vol. 4 (McGraw-hill New York, 2000).

[26] Gaskin, S. *Behavioral Neuroscience: Essentials and Beyond* (SAGE Publications, Incorporated, 2020).

[27] Waxman, S. G., Kocsis, J. D. & Stys, P. K. *The axon: structure, function, and pathophysiology* (Oxford University Press, USA, 1995).

[28] Bear, M. F., Connors, B. W. & Michael, A. Paradiso. Neuroscience: exploring the brain (2001).

[29] Reznik, J. *Rehabilitation in Spinal Cord Injuries* (Elsevier Health Sciences, 2020). URL https://books.google.ca/books?id=xbXrDwAAQBAJ.

[30] Waxman, S. G. & Swadlow, H. A. Ultrastructure of visual callosal axons in the rabbit. *Experimental Neurology* **53**, 115–127 (1976).

[31] Waxman, S. G. & Bennett, M. V. L. Relative conduction velocities of small myelinated and non-myelinated fibres in the central nervous system. *Nature* **238**, 217–219 (1972).

[32] Waxman, S. G., Kocsis, J. D. & Stys, P. K. *The axon: structure, function, and pathophysiology* (Oxford University Press, 1995).

[33] Purves, D. *et al.* Neuroscience. *Sunderland, MA: Sinauer Associates* **773** (2004).

[34] Perge, J. A., Niven, J. E., Mugnaini, E., Balasubramanian, V. & Sterling, P. Why Do Axons Differ in Caliber? *Journal of Neuroscience* **32**, 626–638 (2012). URL http://www.jneurosci.org/cgi/doi/10.1523/JNEUROSCI.4254-11.2012.

[35] Bodian, D. A note on nodes of ranvier in the central neevous system. *Journal of Comparative Neurology* **94**, 475–483 (1951).

[36] Thaxton, C. & Bhat, M. A. Myelination and regional domain differentiation of the axon. In *Cell Biology of the Axon*, 65–85 (Springer, 2009).

[37] Babbs, C. F. & Shi, R. Subtle paranodal injury slows impulse conduction in a mathematical model of myelinated axons. *PloS one* **8**, e67767 (2013).

[38] Dayan, P. & Abbott, L. F. Theoretical neuroscience: computational and mathematical modeling of neural systems. *Journal of cognitive neuroscience* **15**, 154–155 (2003).

[39] Zeberg, H., Blomberg, C. & Århem, P. Ion channel density regulates switches between regular and fast spiking in soma but not in axons. *PLoS computational biology* **6**, e1000753 (2010).

[40] Århem, P., Klement, G. & Blomberg, C. Channel density regulation of firing patterns in a cortical neuron model. *Biophysical journal* **90**, 4392–4404 (2006).

[41] Dewan, M. C. *et al.* Estimating the global incidence of traumatic brain injury. *Journal of neurosurgery* 1–18 (2018).

[42] Youssef, M. R. L. & Galal, Y. S. Causes and outcome predictors of traumatic brain injury among emergency admitted pediatric patients at cairo university hospitals. *The Journal of the Egyptian Public Health Association* **90**, 139–145 (2015).

[43] Koskinen, S. & Alaranta, H. Traumatic brain injury in finland 1991–2005: a nationwide register study of hospitalized and fatal tbi. *Brain Injury* **22**, 205–214 (2008).

[44] Tanielian, T. L., Tanielian, T. & Jaycox, L. *Invisible wounds of war: Psychological and cognitive injuries, their consequences, and services to assist recovery*, vol. 1 (Rand Corporation, 2008).

[45] Faul, M., Wald, M. M., Xu, L. & Coronado, V. G. Traumatic brain injury in the united states; emergency department visits, hospitalizations, and deaths, 2002-2006 (2010).

[46] Servadei, F., Compagnone, C. & Sahuquillo, J. The role of surgery in traumatic brain injury. *Current opinion in critical care* **13**, 163–168 (2007).

[47] Weiner, M. W., Crane, P. K., Montine, T. J., Bennett, D. A. & Veitch, D. P. Traumatic brain injury may not increase the risk of alzheimer disease. *Neurology* **89**, 1923–1925 (2017).

[48] Sivanandam, T. M. & Thakur, M. K. Traumatic brain injury: a risk factor for alzheimer's disease. *Neuroscience & Biobehavioral Reviews* **36**, 1376–1381 (2012).

[49] Hayes, J. P. *et al.* Mild traumatic brain injury is associated with reduced cortical thickness in those at risk for alzheimer's disease. *Brain* **140**, 813–825 (2017).

[50] Miller, D. R., Hayes, J. P., Lafleche, G., Salat, D. H. & Verfaellie, M. White matter abnormalities are associated with chronic postconcussion symptoms in blast-related mild traumatic brain injury. *Human brain mapping* **37**, 220–229 (2016).

[51] Michael Paul Mason. Traumatic brain injury basics (2018). URL https://www.brainline.org/article/traumatic-brain-injury-basics. [Online; accessed 6-February-2019].

[52] Pickett, W., Simpson, K., Walker, J. & Brison, R. J. Traumatic spinal cord injury in Ontario, Canada. *Journal of Trauma-Injury, Infection, and Critical Care* **55**, 1070–1076 (2003).

[53] DeVivo, M. J. Epidemiology of spinal cord injury. *Spinal Cord Medicine Principles and Practice.: Demos Medical Publishing: New York, NY, USA* 78–84 (2010).

[54] Acton, P. A. *et al.* Traumatic spinal cord injury in arkansas, 1980 to 1989. *Archives of physical medicine and rehabilitation* **74**, 1035–1040 (1993).

[55] DeVivo, M. J. Epidemiology of traumatic spinal cord injury: trends and future implications. *Spinal cord* **50**, 365–372 (2012).

[56] White, N.-H. & Black, N.-H. Spinal cord injury (sci) facts and figures at a glance. *Birmingham: National Spinal Cord Injury Statistical Center, Facts and Figures at a Glance* (2016).

[57] Gilmour, H., Ramage-Morin, P. L. & Wong, S. L. Multiple sclerosis: Prevalence and impact. *Health reports* **29**, 3–8 (2018).

[58] Orton, S.-M. *et al.* Sex ratio of multiple sclerosis in canada: a longitudinal study. *The Lancet Neurology* **5**, 932–936 (2006).

[59] Induruwa, I., Constantinescu, C. S. & Gran, B. Fatigue in multiple sclerosis—a brief review. *Journal of the neurological sciences* **323**, 9–15 (2012).

[60] Goldenberg, M. M. Multiple sclerosis review. *Pharmacy and Therapeutics* **37**, 175 (2012).

[61] BERGSNEIDER, M. *et al.* Dissociation of cerebral glucose metabolism and level of consciousness during the period of metabolic depression following human traumatic brain injury. *Journal of neurotrauma* **17**, 389–401 (2000).

[62] Vagnozzi, R. *et al.* Assessment of metabolic brain damage and recovery following mild traumatic brain injury: a multicentre, proton magnetic resonance spectroscopic study in concussed patients. *Brain* **133**, 3232–3242 (2010).

[63] Vespa, P. *et al.* Metabolic crisis without brain ischemia is common after traumatic brain injury: a combined microdialysis and positron emission tomography study. *Journal of Cerebral Blood Flow & Metabolism* **25**, 763–774 (2005).

[64] Adams, J. H., Graham, D., Murray, L. S. & Scott, G. Diffuse axonal injury due to nonmissile head injury in humans: an analysis of 45 cases. *Annals of Neurology: Official Journal of the American Neurological Association and the Child Neurology Society* **12**, 557–563 (1982).

[65] Chodobski, A., Zink, B. J. & Szmydynger-Chodobska, J. Blood–brain barrier pathophysiology in traumatic brain injury. *Translational stroke research* **2**, 492–516 (2011).

[66] Bouma, G. J. *et al.* Ultra-early evaluation of regional cerebral blood flow in severely head-injured patients using xenon-enhanced computerized tomography. *Journal of neurosurgery* **77**, 360–368 (1992).

[67] Kilinc, D., Gallo, G. & Barbee, K. A. Mechanical membrane injury induces axonal beading through localized activation of calpain. *Experimental neurology* **219**, 553–561 (2009).

[68] Lee, H. *et al.* Focal lesions in acute mild traumatic brain injury and neurocognitive outcome: Ct versus 3t mri. *Journal of neurotrauma* **25**, 1049–1056 (2008).

[69] de Lanerolle, N. C., Kim, J. H. & Bandak, F. A. Neuropathology of traumatic brain injury: comparison of penetrating, nonpenetrating direct impact and explosive blast etiologies. In *Seminars in neurology*, vol. 35, 012–019 (Thieme Medical Publishers, 2015).

[70] Johnson, V. E., Stewart, W. & Smith, D. H. Axonal pathology in traumatic brain injury. *Experimental neurology* **246**, 35–43 (2013).

[71] Smith, D. H., Hicks, R. & Povlishock, J. T. Therapy development for diffuse axonal injury. *Journal of neurotrauma* **30**, 307–323 (2013).

[72] Gentleman, S. *et al.* Axonal injury: a universal consequence of fatal closed head injury? *Acta neuropathologica* **89**, 537–543 (1995).

[73] CHRISTMAN, C. W., GRADY, M. S., WALKER, S. A., HOLLOWAY, K. L. & POVLISHOCK, J. T. Ultrastructural studies of diffuse axonal injury in humans. *Journal of neurotrauma* **11**, 173–186 (1994).

[74] Maxwell, W., Watt, C., Graham, D. & Gennarelli, T. Ultrastructural evidence of axonal shearing as a result of lateral acceleration of the head in non-human primates. *Acta neuropathologica* **86**, 136–144 (1993).

[75] Gennarelli, T. A., Thibault, L. E. & Graham, D. I. Diffuse axonal injury: an important form of traumatic brain damage. *The Neuroscientist* **4**, 202–215 (1998).

[76] Maxwell, W. L. Histopathological changes at central nodes of Ranvier after stretch-injury. *Microscopy research and technique* **34**, 522–535 (1996).

[77] Maxwell, W. L. *et al.* Focal axonal injury: the early axonal response to stretch. *Journal of Neurocytology* **20**, 157–164 (1991).

[78] Wang, J., Hamm, R. J. & Povlishock, J. T. Traumatic axonal injury in the optic nerve: evidence for axonal swelling, disconnection, dieback, and reorganization. *Journal of neurotrauma* **28**, 1185–1198 (2011).

[79] Kolaric, K. V., Thomson, G., Edgar, J. M. & Brown, A. M. Focal axonal swellings and associated ultrastructural changes attenuate conduction velocity in central nervous system axons: a computer modeling study. *Physiological reports* **1**, e00059 (2013). URL http://www.pubmedcentral.nih.gov/articlerender.fcgi?artid=3835014{&}tool=pmcentrez{&}rendertype=abstract.

[80] Liu, J., Liu, M. C. & Wang, K. K. Calpain in the cns: from synaptic function to neurotoxicity. *Science signaling* **1**, re1–re1 (2008).

[81] Reeves, T. M., Phillips, L. L. & Povlishock, J. T. Myelinated and unmyelinated axons of the corpus callosum differ in vulnerability and functional recovery following traumatic brain injury. *Experimental neurology* **196**, 126–137 (2005).

[82] Tang-Schomer, M. D., Johnson, V. E., Baas, P. W., Stewart, W. & Smith, D. H. Partial interruption of axonal transport due to microtubule breakage accounts for the formation of periodic varicosities after traumatic axonal injury. *Experimental neurology* **233**, 364–72 (2012). URL http://www.pubmedcentral.nih.gov/articlerender.fcgi?artid=3979336{&}tool=pmcentrez{&}rendertype=abstract.

[83] Blight, A. R. Cellular morphology of chronic spinal cord injury in the cat: Analysis of myelinated axons by line-sampling. *Neuroscience* **10**, 521–543 (1983). URL http://europepmc.org/abstract/MED/6633870http://linkinghub.elsevier.com/retrieve/pii/0306452283901501.

[84] Blight, A. R. Morphometric analysis of a model of spinal cord injury in guinea pigs, with behavioral evidence of delayed secondary pathology. *Journal of the Neurological Sciences* **103**, 156–171 (1991).

[85] Powers, B. E. *et al.* Axonal thinning and extensive remyelination without chronic demyelination in spinal injured rats. *The Journal of neuroscience : the official journal of the Society for Neuroscience* **32**, 5120–5 (2012). URL http://www.jneurosci.org/content/32/15/5120.shorthttp://www.pubmedcentral.nih.gov/articlerender.fcgi?artid=3335198{&}tool=pmcentrez{&}rendertype=abstract.

[86] Rosenberg, L. J. & Wrathall, J. R. Quantitative Analysis of Acute Axonal Pathology in Experimental Spinal Cord Contusion. *Journal of Neurotrauma* **14**, 823–838 (1997). URL http://online.liebertpub.com/doi/abs/10.1089/neu.1997.14.823.

[87] Dollé, J.-P., Morrison III, B., Schloss, R. S. & Yarmush, M. L. Brain-on-a-chip microsystem for investigating traumatic brain injury: Axon diameter and mitochondrial membrane changes play a significant role in axonal response to strain injuries. *Technology* **2**, 106–117 (2014).

[88] Rickett, T., Connell, S., Bastijanic, J., Hegde, S. & Shi, R. Functional and mechanical evaluation of nerve stretch injury. *Journal of medical systems* **35**, 787–93 (2011). URL http://www.ncbi.nlm.nih.gov/pubmed/20703726.

[89] Fu, Y., Sun, W., Shi, Y., Shi, R. & Cheng, J. X. Glutamate excitotoxicity inflicts paranodal myelin splitting and retraction. *PLoS ONE* **4** (2009).

[90] Huff, T. B. *et al.* Real-time CARS imaging reveals a calpain-dependent pathway for paranodal myelin retraction during high-frequency stimulation. *PloS one* **6**, e17176 (2011). URL http://www.pubmedcentral.nih.gov/articlerender.fcgi?artid=3048389{&}tool=pmcentrez{&}rendertype=abstract.

[91] Wolf, J. A., Stys, P. K., Lusardi, T., Meaney, D. & Smith, D. H. Traumatic axonal injury induces calcium influx modulated by tetrodotoxin-sensitive sodium channels. *Journal of Neuroscience* **21**, 1923–1930 (2001).

[92] Shi, R. & Blight, A. R. Compression injury of mammalian spinal cord in vitro and the dynamics of action potential conduction failure. *Journal of neurophysiology* **76**, 1572–1580 (1996).

[93] Shi, R. & Sun, W. Potassium channel blockers as an effective treatment to restore impulse conduction in injured axons (2011).

[94] Volman, V. & Ng, L. J. Computer modeling of mild axonal injury: implications for axonal signal transmission. *Neural computation* **25**, 2646–2681 (2013).

[95] Volman, V. & Ng, L. J. Primary paranode demyelination modulates slowly developing axonal depolarization in a model of axonal injury (2014). URL http://link.springer.com/article/10.1007/s10827-014-0515-7.

[96] Goldstein, L. E. *et al.* Chronic traumatic encephalopathy in blast-exposed military veterans and a blast neurotrauma mouse model. *Science translational medicine* **4**, 134ra60 (2012).

[97] Hines, M. L. & Carnevale, N. T. The NEURON simulation environment. *Neural computation* **9**, 1179–1209 (1997).

[98] McIntyre, C. C., Richardson, A. G. & Grill, W. M. Modeling the excitability of mammalian nerve fibers: influence of afterpotentials on the recovery cycle. *Journal of neurophysiology* **87**, 995–1006 (2002).

[99] Schutter, E. D. *Computational modeling methods for neuroscientists* (The MIT Press, 2010).

[100] Dayan, P. & Abbott, L. F. *Theoretical neuroscience: computational and mathematical modeling of neural systems* (Computational Neuroscience Series, 2001).

[101] Herz, A. V., Gollisch, T., Machens, C. K. & Jaeger, D. Modeling single-neuron dynamics and computations: a balance of detail and abstraction. *science* **314**, 80–85 (2006).

[102] Hodgkin, A. & Huxley, A. A quantitative description of membrane current and its application to conduction and excitation in nerve. *The Journal of physiology* **117**, 500–544 (1952). URL http://www.ncbi.nlm.nih.gov/pmc/articles/pmc1392413/.

[103] Izhikevich, E. M. *Dynamical systems in neuroscience* (MIT press, 2007).

[104] Pospischil, M., Piwkowska, Z., Bal, T. & Destexhe, A. Comparison of different neuron models to conductance-based post-stimulus time histograms obtained in cortical pyramidal cells using dynamic-clamp in vitro. *Biological cybernetics* **105**, 167 (2011).

[105] Izhikevich, E. M. Which model to use for cortical spiking neurons? *IEEE transactions on neural networks* **15**, 1063–1070 (2004).

[106] Young, J. Z. The functioning of the giant nerve fibres of the squid. *Journal of Experimental Biology* **15**, 170–185 (1938).

[107] Sakmann, B. & Neher, E. Patch clamp techniques for studying ionic channels in excitable membranes. *Annual Review of Physiology* **46**, 455–472 (1984).

[108] Rodriguez, B. M., Sigg, D. & Bezanilla, F. Voltage gating of Shaker K+ channels. The effect of temperature on ionic and gating currents. *The Journal of general physiology* **112**, 223–242 (1998).

[109] Hille, B. *Ion channels of excitable membranes*, vol. 507 (Sinauer Sunderland, MA, 2001).

[110] Povlishock, J. T. & Pettus, E. H. Traumatically induced axonal damage: evidence for enduring changes in axolemmal permeability with associated cytoskeletal change. In *Mechanisms of Secondary Brain Damage in Cerebral Ischemia and Trauma*, 81–86 (Springer, 1996).

[111] Pettus, E. H. & Povlishock, J. T. Characterization of a distinct set of intra-axonal ultrastructural changes associated with traumatically induced alteration in axolemmal permeability. *Brain research* **722**, 1–11 (1996).

[112] Boucher, P.-A., Joós, B. & Morris, C. E. Coupled left-shift of Nav channels: modeling the Na -loading and dysfunctional excitability of damaged axons. *Journal of computational neuroscience* **33**, 301–319 (2012).

[113] Tabarean, I. V., Juranka, P. & Morris, C. E. Membrane stretch affects gating modes of a skeletal muscle sodium channel. *Biophysical journal* **77**, 758–774 (1999).

[114] Carnevale, N. T. & Hines, M. L. *The NEURON Book*, vol. 30 (Cambridge University Press, Cambridge, 2006). URL http://books.google.com/books?hl=en{&}lr={&}id=YzcOyjKBPHgC{&}oi=fnd{&}pg=PA1{&}dq=The+Neuron+Book{&}ots=Ki6EKu{_}ZLd{&}sig=3Cd1R026GoIeT59HkXyV-xHm7Yohttp://ebooks.cambridge.org/ref/id/CBO9780511541612.

[115] Neuron. Neuron (2014).

[116] McDougal, R. A. *et al.* Twenty years of modeldb and beyond: building essential modeling tools for the future of neuroscience. *Journal of computational neuroscience* **42**, 1–10 (2017).

[117] Peterson, E., Izad, O. & Tyler, D. J. Predicting myelinated axon activation using spatial characteristics of the extracellular field. *Journal of neural engineering* **8**, 046030 (2011).

[118] Schiefer, M. A., Triolo, R. J. & Tyler, D. J. A model of selective activation of the femoral nerve with a flat interface nerve electrode for a lower extremity neuroprosthesis. *IEEE transactions on neural systems and rehabilitation engineering* **16**, 195–204 (2008).

[119] Wongsarnpigoon, A., Woock, J. P. & Grill, W. M. Efficiency analysis of waveform shape for electrical excitation of nerve fibers. *IEEE transactions on neural systems and rehabilitation engineering : a publication of the IEEE Engineering in Medicine and Biology Society* **18**, 319–28 (2010). URL http://www.pubmedcentral.nih.gov/articlerender.fcgi?artid=3071515{&}tool=pmcentrez{&}rendertype=abstract.

[120] Kilgore, K. L. & Bhadra, N. Nerve conduction block utilising high-frequency alternating current. *Medical and Biological Engineering and Computing* **42**, 394–406 (2004).

[121] Miles, J., Kilgore, K., Bhadra, N. & Lahowetz, E. Effects of ramped amplitude waveforms on the onset response of high-frequency mammalian nerve block. *Journal of neural engineering* **4**, 390 (2007).

[122] Birdno, M. J. *et al.* Stimulus features underlying reduced tremor suppression with temporally patterned deep brain stimulation. *Journal of neurophysiology* **107**, 364–383 (2012).

[123] Lubba, C. H. *et al.* Pypns: Multiscale simulation of a peripheral nerve in python. *Neuroinformatics* **17**, 63–81 (2019).

[124] Lasiene, J., Shupe, L., Perlmutter, S. & Horner, P. No evidence for chronic demyelination in spared axons after spinal cord injury in a mouse. *The Journal of neuroscience : the official journal of the Society for Neuroscience* **28**, 3887–3896 (2008).

[125] Varma, A. K. *et al.* Spinal Cord Injury: A Review of Current Therapy, Future Treatments, and Basic Science Frontiers. *Neurochemical Research* **38**, 895–905 (2013). URL http://link.springer.com/10.1007/s11064-013-0991-6.

[126] Alluin, O. *et al.* Examination of the combined effects of chondroitinase ABC, growth factors and locomotor training following compressive spinal cord injury on neuroanatomical plasticity and kinematics. *PloS one* **9**, e111072 (2014). URL http://www.pubmedcentral.nih.gov/articlerender.fcgi?artid=4211738{&}tool=pmcentrez{&}rendertype=abstract.

[127] Streijger, F. *et al.* Combinatorial treatment of acute spinal cord injury with ghrelin, ibuprofen, C16, and ketogenic diet does not result in improved histologic or functional outcome. *Journal of Neuroscience Research* **92**, 870–883 (2014). URL http://doi.wiley.com/10.1002/jnr.23372.

[128] Holt, A. B. & Netoff, T. I. Computational modeling of epilepsy for an experimental neurologist. *Experimental Neurology* **244**, 75–86 (2013). URL http://linkinghub.elsevier.com/retrieve/pii/S0014488612002014.

[129] Jérusalem, A., García-Grajales, J. A., Merchán-Pérez, A. & Peña, J. M. A computational model coupling mechanics and electrophysiology in spinal cord injury. *Biomechanics and modeling in mechanobiology* **13**, 1–14 (2013). URL http://www.ncbi.nlm.nih.gov/pubmed/24337934.

[130] Goldman, L. & Albus, J. S. Computation of impulse conduction in myelinated fibers; theoretical basis of the velocity-diameter relation. *Biophysical journal* **8**, 596–607 (1968).

[131] Hartline, D. K. & Colman, D. R. Rapid conduction and the evolution of giant axons and myelinated fibers. *Current biology : CB* **17**, R29–35 (2007). URL http://www.sciencedirect.com/science/article/pii/S0960982206025231http://www.ncbi.nlm.nih.gov/pubmed/17208176.

[132] Hines, M. L., Morse, T., Migliore, M., Carnevale, N. T. & Shepherd, G. M. ModelDB: a database to support computational neuroscience. *Journal of computational neuroscience* **17**, 7–11 (2004).

[133] Arlow, R. L., Foutz, T. J. & McIntyre, C. C. Theoretical principles underlying optical stimulation of myelinated axons expressing channelrhodopsin-2. *Neuroscience* **248**, 541–551 (2013). NIHMS150003.

[134] Bhadra, N., Lahowetz, E. a., Foldes, S. T. & Kilgore, K. L. Simulation of high-frequency sinusoidal electrical block of mammalian myelinated axons. *Journal of computational neuroscience* **22**, 313–26 (2007). URL http://www.ncbi.nlm.nih.gov/pubmed/17200886.

[135] Danner, S. M., Hofstoetter, U. S., Ladenbauer, J., Rattay, F. & Minassian, K. Can the human lumbar posterior columns be stimulated by transcutaneous spinal cord stimulation? A modeling study. *Artificial Organs* **35**, 257–262 (2011).

[136] Danner, S. M. *An application for learning and teaching extracellular stimulation of axons.* Ph.D. thesis, Fakultät für Informatik der Technischen Universität Wien (2011).

[137] Devaux, J. & Gow, A. Tight junctions potentiate the insulative properties of small CNS myelinated axons. *The Journal of cell biology* **183**, 909–21 (2008). URL http://jcb.rupress.org/content/183/5/909.shorthttp://www.pubmedcentral.nih.gov/articlerender.fcgi?artid=2592840{&}tool=pmcentrez{&}rendertype=abstract.

[138] Johnson, M. D. & McIntyre, C. C. Quantifying the neural elements activated and inhibited by globus pallidus deep brain stimulation. *Journal of neurophysiology* **100**, 2549–63 (2008). URL http://jn.physiology.org/content/100/5/2549.shorthttp://www.pubmedcentral.nih.gov/articlerender.fcgi?artid=2585404{&}tool=pmcentrez{&}rendertype=abstract.

[139] Lempka, S. F. *et al. The electrode-tissue interface during recording and stimulation in the central nervous system.* Ph.D. thesis, Case Western Reserve University (2010).

[140] McIntyre, C. C., Grill, W. M., Sherman, D. L. & Thakor, N. V. Cellular effects of deep brain stimulation: model-based analysis of activation and inhibition. *Journal of neurophysiology* **91**, 1457–69 (2004). URL http://jn.physiology.org/content/91/4/1457.shorthttp://www.ncbi.nlm.nih.gov/pubmed/14668299.

[141] Moffitt, M. A., McIntyre, C. C. & Grill, W. M. Prediction of Myelinated Nerve Fiber Stimulation Thresholds: Limitations of Linear Models. *IEEE Transactions on Biomedical Engineering* **51**, 229–236 (2004).

[142] Pelot, N. A., Behrend, C. E. & Grill, W. M. Modeling the response of small myelinated and unmyelinated axons to kilohertz frequency signals. In *2015 7th International IEEE/EMBS Conference on Neural Engineering (NER)*, 406–409 (IEEE, 2015). URL http://ieeexplore.ieee.org/lpdocs/epic03/wrapper.htm?arnumber=7146645.

[143] Ouyang, H. *et al.* Compression induces acute demyelination and potassium channel exposure in spinal cord. *Journal of neurotrauma* **27**, 1109–20 (2010). URL http://www.pubmedcentral.nih.gov/articlerender.fcgi?artid=2943505{&}tool=pmcentrez{&}rendertype=abstract.

[144] Reeves, T. M., Greer, J. E., Vanderveer, A. S. & Phillips, L. L. Proteolysis of submembrane cytoskeletal proteins ankyrin-G and alpha-II-spectrin following diffuse brain injury: A role in white matter vulnerability at Nodes of Ranvier. *Brain Pathology (Zurich, Switzerland)* **20**, 1055–1068 (2010). URL http://www.ncbi.nlm.nih.gov/pmc/articles/PMC3265329/.

[145] Sun, W. *et al.* Paranodal myelin damage after acute stretch in guinea pig spinal cord. *Journal of neurotrauma* **29**, 611–619 (2012).

[146] Berthold, C. H. & Rydmark, M. Anatomy of the paranode-node-paranode region in the cat. *Cellular and Molecular Life Sciences* **39**, 964–976 (1983).

[147] Berthold, C. H., Nilsson, I. & Rydmark, M. Axon diameter and myelin sheath thickness in nerve fibres of the ventral spinal root of the seventh lumbar nerve of the adult and developing cat. *Journal of anatomy* **136**, 483 (1983).

[148] Fiore, M. *Atlas of Human Histology* (Lea & Febiger, Philadelphia, 1981). URL http://scholar.google.ca/scholar?q=diFiori+MSH{&}hl=en{&}as{_}sdt=0,5{&}as{_}ylo=1981{&}as{_}yhi={#}3.

[149] Nilsson, I. & Berthold, C. H. Axon classes and internodal growth in the ventral spinal root L7 of adult and developing cats. *Journal of anatomy* **156**, 71–96 (1988).

[150] Horresh, I. *et al.* Multiple molecular interactions determine the clustering of Caspr2 and Kv1 channels in myelinated axons. *The Journal of neuroscience : the official journal of the Society for Neuroscience* **28**, 14213–22 (2008). URL http://www.jneurosci.org/content/28/52/14213.shorthttp://www.pubmedcentral.nih.gov/articlerender.fcgi?artid=2859216{&}tool=pmcentrez{&}rendertype=abstract.

[151] Lovas, G., Szilagyi, N., Majtenyi, K., Palkovits, M. & Komoly, S. Axonal changes in chronic demyelinated cervical spinal cord plaques. *Brain* **123**, 308–317 (2000). URL http://brain.oxfordjournals.org/content/123/2/308.shorthttp://www.brain.oxfordjournals.org/cgi/doi/10.1093/brain/123.2.308.

[152] Makeig, S. *et al.* Evolving signal processing for brain–computer interfaces. *Proceedings of the IEEE* **100**, 1567–1584 (2012).

[153] Ong, H. H. & Wehrli, F. W. Quantifying axon diameter and intra-cellular volume fraction in excised mouse spinal cord with q-space imaging. *NeuroImage* **51**, 1360–6 (2010). URL http://www.sciencedirect.com/science/article/pii/S1053811910003502http://www.pubmedcentral.nih.gov/articlerender.fcgi?artid=2895496{&}tool=pmcentrez{&}rendertype=abstract.

[154] Rydmark, M. & Berthold, C. H. Electron microscopic serial section analysis of nodes of Ranvier in lumbar spinal roots of the cat: a morphometric study of nodal compartments in fibres of different sizes. *Journal of neurocytology* **12**, 537–565 (1983).

[155] Rydmark, M. Nodal axon diameter correlates linearly with internodal axon diameter in spinal roots of the cat. *Neuroscience letters* **24**, 247–250 (1981).

[156] Zhu, F. *et al.* Segment-specific resistivity improves body fluid volume estimates from bioimpedance spectroscopy in hemodialysis patients. *Journal of applied physiology (Bethesda, Md. : 1985)* **100**, 717–24 (2006). URL http://jap.physiology.org/content/100/2/717.shorthttp://www.ncbi.nlm.nih.gov/pubmed/16254072.

[157] Jensen, J. M. & Shi, R. Effects of 4-aminopyridine on stretched mammalian spinal cord: the role of potassium channels in axonal conduction. *Journal of neurophysiology* **90**, 2334–40 (2003). URL http://www.ncbi.nlm.nih.gov/pubmed/12853442.

[158] Sun, W. *et al.* Novel potassium channel blocker, 4-AP-3-MeOH, inhibits fast potassium channels and restores axonal conduction in injured guinea pig spinal cord white matter. *Journal of neurophysiology* **103**, 469–78 (2010). URL http://www.ncbi.nlm.nih.gov/pubmed/19923250.

[159] Anthes, D. L., Theriault, E. & Tator, C. H. Characterization of axonal ultrastructural pathology following experimental spinal cord compression injury. *Brain Research* **702**, 1–16 (1995). URL http://www.sciencedirect.com/science/article/pii/0006899395010286http://linkinghub.elsevier.com/retrieve/pii/0006899395010286.

[160] Arancibia-Carcamo, I. L. & Attwell, D. The node of Ranvier in CNS pathology. *Acta Neuropathologica* **128**, 161–175 (2014). URL http://link.springer.com/10.1007/s00401-014-1305-z.

[161] Iwata, A., Stys, P. & Wolf, J. Traumatic axonal injury induces proteolytic cleavage of the voltage-gated sodium channels modulated by tetrodotoxin and protease inhibitors. *The Journal of ...* (2004). URL http://www.jneurosci.org/content/24/19/4605.short.

[162] Waxman, S. G. Axonal conduction and injury in multiple sclerosis: the role of sodium channels. *Nature reviews. Neuroscience* **7**, 932–41 (2006). URL http://www.nature.com/nrn/journal/v7/n12/abs/nrn2023.htmlhttp://www.ncbi.nlm.nih.gov/pubmed/17115075.

[163] Stirling, D. P. & Stys, P. K. Mechanisms of axonal injury: internodal nanocomplexes and calcium deregulation. *Trends in molecular medicine* **16**, 160–70 (2010). URL http://www.sciencedirect.com/science/article/pii/S1471491410000213http://www.pubmedcentral.nih.gov/articlerender.fcgi?artid=2976657{&}tool=pmcentrez{&}rendertype=abstract.

[164] Nashmi, R. & Fehlings, M. G. Mechanisms of axonal dysfunction after spinal cord injury: with an emphasis on the role of voltage-gated potassium channels. *Brain Research Reviews* **38**, 165–191 (2001). URL http://www.sciencedirect.com/science/article/pii/S0165017301001345http://linkinghub.elsevier.com/retrieve/pii/S0165017301001345.

[165] Susuki, K. Node of Ranvier disruption as a cause of neurological diseases. *ASN neuro* **5**, 209–19 (2013). URL http://www.pubmedcentral.nih.gov/articlerender.fcgi?artid=3736360{&}tool=pmcentrez{&}rendertype=abstract.

[166] Schwarz, J. R., Reid, G. & Bostock, H. Action potentials and membrane currents in the human node of Ranvier. *European Journal of Physiology* **430**, 283–292 (1995). URL http://link.springer.com/10.1007/BF00374660.

[167] Blight, A. R. Effect of 4-aminopyridine on axonal conduction-block in chronic spinal cord injury. *Brain research bulletin* **22**, 47–52 (1989).

[168] Nowak, L. G. & Bullier, J. Axons, but not cell bodies, are activated by electrical stimulation in cortical gray matter. *Experimental Brain Research* **118**, 489–500 (1998). URL http://invibe.net/biblio{_}database{_}dyva/woda/data/att/2cff.file.06326.pdfhttp://link.springer.com/10.1007/s002210050305.

[169] Ranck, J. B. Which elements are excited in electrical stimulation of mammalian central nervous system: A review. *Brain Research* **98**, 417–440 (1975). URL http://www.sciencedirect.com/science/article/pii/0006899375903649http://linkinghub.elsevier.com/retrieve/pii/0006899375903649.

[170] Gasser, H. & Grundfest, H. Axon diameters in relation to the spike dimensions and the conduction velocity in mammalian A fibers. *American Journal of Physiology* **127**, 393–414 (1939). URL http://ajplegacy.physiology.org/content/ajplegacy/127/2/393.full.pdf.

[171] Shi, R. & Whitebone, J. Conduction deficits and membrane disruption of spinal cord axons as a function of magnitude and rate of strain. *Journal of neurophysiology* **95**, 3384–90 (2006). URL http://www.ncbi.nlm.nih.gov/pubmed/16510778.

[172] Boyd, I. A. & Kalu, K. U. Scaling factor relating conduction velocity and diameter for myelinated afferent nerve fibres in the cat hind limb. *Journal of Physiology* **289**, 277–297 (1979). URL http://www.scopus.com/inward/record.url?eid=2-s2.0-0018332826{&}partnerID=tZOtx3y1.

[173] Hoffer, J. A. *et al.* Cat hindlimb motoneurons during locomotion. I. Destination, axonal conduction velocity, and recruitment threshold. *Journal of neurophysiology* **57**, 510–529 (1987).

[174] Espósito, M. S. *et al.* Neuronal differentiation in the adult hippocampus recapitulates embryonic development. *The Journal of neuroscience* **25**, 10074–10086 (2005).

[175] Kerr, J. N. D. & Wickens, J. R. Dopamine D-1/D-5 Receptor Activation Is Required for Long-Term Potentiation in the Rat Neostriatum In Vitro. *Journal of Neurophysiology* **85**, 117–124 (2001). URL http://jn.physiology.org/content/85/1/117.abstract.

[176] Tripathy, S. J., Savitskaya, J., Burton, S. D., Urban, N. N. & Gerkin, R. C. NeuroElectro: a window to the world's neuron electrophysiology data. *Frontiers in neuroinformatics* **8**, 40 (2014). URL http://www.pubmedcentral.nih.gov/articlerender.fcgi?artid=4010726{&}tool=pmcentrez{&}rendertype=abstract.

[177] Ragnarsson, K. T. Functional electrical stimulation after spinal cord injury: current use, therapeutic effects and future directions. *Spinal Cord* **46**, 255–274 (2008). URL http://www.nature.com/doifinder/10.1038/sj.sc.3102091.

[178] Vodovnik, L., Stefanovska, A. & Bajd, T. Effects of stimulation parameters on modification of spinal spasticity. *Medical & Biological Engineering & Computing* **25**, 439–442 (1987). URL http://link.springer.com/10.1007/BF02443365.

[179] Capogrosso, M. *et al.* A Computational Model for Epidural Electrical Stimulation of Spinal Sensorimotor Circuits. *Journal of Neuroscience* **33**, 19326–19340 (2013).

[180] Geddes, D. M., LaPlaca, M. C. & Cargill, R. S. Susceptibility of hippocampal neurons to mechanically induced injury. *Experimental Neurology* **184**, 420–427 (2003).

[181] Shi, R. & Pryor, J. D. Pathological changes of isolated spinal cord axons in response to mechanical stretch. *Neuroscience* **110**, 765–777 (2002).

[182] Castelfranco, A. M. & Hartline, D. K. The evolution of vertebrate and invertebrate myelin: a theoretical computational study. *Journal of Computational Neuroscience* **38**, 521–538 (2015). URL http://link.springer.com/10.1007/s10827-015-0552-x.

[183] More, H. L. *et al.* Scaling of sensorimotor control in terrestrial mammals. *Proceedings of the Royal Society B: Biological Sciences* **277**, 3563–3568 (2010). URL http://rspb.royalsocietypublishing.org/cgi/doi/10.1098/rspb.2010.0898.

[184] Bostock, H., Sears, T. A. & Sherratt, R. M. The spatial distribution of excitability and membrane current in normal and demyelinated mammalian nerve fibres. *The Journal of physiology* **341**, 41–58 (1983).

[185] DeForge, D. *et al.* Effect of 4-aminopyridine on gait in ambulatory spinal cord injuries: a double-blind, placebo-controlled, crossover trial. Tech. Rep. 12 (2004).

[186] Domingo, A. *et al.* A Systematic Review of the Effects of Pharmacological Agents on Walking Function in People with Spinal Cord Injury (2012).

[187] Wolf, J., Stys, P. & Lusardi, T. Traumatic axonal injury induces calcium influx modulated by tetrodotoxin-sensitive sodium channels. *The Journal of ...* (2001). URL http://www.jneurosci.org/content/21/6/1923.short.

[188] Leung, G., Sun, W., Brookes, S., Smith, D. & Shi, R. Potassium channel blocker, 4-aminopyridine-3-methanol, restores axonal conduction in spinal cord of an animal model of multiple sclerosis. *Experimental neurology* **227**, 232–235 (2011).

[189] Smith, K. J., Felts, P. A. & John, G. R. Effects of 4-aminopyridine on demyelinated axons, synapses and muscle tension. *Brain* **123**, 171–184 (2000). URL http://brain.oxfordjournals.org/content/123/1/171.abstract.

[190] Van der Bruggen, M. a. *et al.* Randomized trial of 4-aminopyridine in patients with chronic incomplete spinal cord injury. *Journal of neurology* **248**, 665–671 (2001).

[191] Tseng, K. *et al.* 4-Aminopyridine promotes functional recovery and remyelination in acute peripheral nerve injury. *EMBO Molecular Medicine* **8**, 1409 LP – 1420 (2016). URL http://embomolmed.embopress.org/content/8/12/1409.abstract.

[192] Lujan, J. L. *et al.* Tractography-Activation Models Applied to Subcallosal Cingulate Deep Brain Stimulation. *Brain Stimulation* **6**, 737–739 (2013).

[193] Khakshour, S., Beischlag, T. V., Sparrey, C. & Park, E. J. Probing mechanical properties of Jurkat cells under the effect of ART using oscillating optical tweezers. *PLoS ONE* **10** (2015).

[194] Wang, H., Fu, Y., Zickmund, P., Shi, R. & Cheng, J.-X. Coherent Anti-Stokes Raman Scattering Imaging of Axonal Myelin in Live Spinal Tissues. *Biophysical Journal* **89**, 581–591 (2005). URL http://www.sciencedirect.com/science/article/pii/S0006349505727065.

[195] Lacour, S. P., Tsay, C., Wagner, S., Zhe, Y. & Morrison, B. Stretchable micro-electrode arrays for dynamic neuronal recording of in vitro mechanically injured brain. In *Proceedings of IEEE Sensors*, vol. 2005, 617–620 (2005).

[196] Russell, C. M. *A Nonlinear Finite Element Model of the Rat Cervical Spine*. Ph.D. thesis, THE UNIVERSITY OF BRITISH COLUMBIA (2012).

[197] Hernández-Labrado, G. R., Polo, J. L., López-Dolado, E. & Collazos-Castro, J. E. Spinal cord direct current stimulation: finite element analysis of the electric field and current density. *Medical & biological engineering & computing* **49**, 417–29 (2011).

[198] Ouyang, H. *et al.* Compression induces acute demyelination and potassium channel exposure in spinal cord. *Journal of neurotrauma* **27**, 1109–1120 (2010).

[199] Tang-Schomer, M. D., Johnson, V. E., Baas, P. W., Stewart, W. & Smith, D. H. Partial interruption of axonal transport due to microtubule breakage accounts for the formation of periodic varicosities after traumatic axonal injury. *Experimental neurology* **233**, 364–372 (2012).

[200] Carnevale, N. T. & Hines, M. L. *The NEURON book* (Cambridge University Press, 2006).

[201] Sterratt, D., Graham, B., Gillies, A. & Willshaw, D. *Principles of computational modelling in neuroscience* (Cambridge University Press, 2011).

[202] De Schutter, E., Ekeberg, Ö., Kotaleski, J. H., Achard, P. & Lansner, A. Biophysically detailed modelling of microcircuits and beyond. *TRENDS in Neurosciences* **28**, 562–569 (2005).

[203] Babbs, C. F. & Shi, R. Subtle paranodal injury slows impulse conduction in a mathematical model of myelinated axons. *PLoS One* **8** (2013).

[204] Kohan, E. D., Lashkari, B. S. & Sparrey, C. J. The effects of paranodal myelin damage on action potential depend on axonal structure. *Medical & biological engineering & computing* **56**, 395–411 (2018).

[205] Volman, V. & Ng, L. J. Computer modeling of mild axonal injury: implications for axonal signal transmission. *Neural Computation* **25**, 2646–2681 (2013).

[206] McIntyre, C. C., Richardson, A. G. & Grill, W. M. Modeling the excitability of mammalian nerve fibers: influence of afterpotentials on the recovery cycle. *Journal of neurophysiology* **87**, 995–1006 (2002).

[207] Sundt, D., Gamper, N. & Jaffe, D. B. Spike propagation through the dorsal root ganglia in an unmyelinated sensory neuron: a modeling study. *Journal of neurophysiology* **114**, 3140–3153 (2015).

[208] Pelot, N. A., Behrend, C. E. & Grill, W. M. Modeling the response of small myelinated and unmyelinated axons to kilohertz frequency signals. In *2015 7th International IEEE/EMBS Conference on Neural Engineering (NER)*, 406–409 (IEEE, 2015).

[209] Van Dijk, K. J. *et al.* A novel lead design enables selective deep brain stimulation of neural populations in the subthalamic region. *Journal of neural engineering* **12**, 046003 (2015).

[210] Danner, S. M., Hofstoetter, U. S., Ladenbauer, J., Rattay, F. & Minassian, K. Can the human lumbar posterior columns be stimulated by transcutaneous spinal cord stimulation? a modeling study. *Artificial organs* **35**, 257–262 (2011).

[211] Gunalan, K., Howell, B. & McIntyre, C. C. Quantifying axonal responses in patient-specific models of subthalamic deep brain stimulation. *Neuroimage* **172**, 263–277 (2018).

[212] Howell, B. & McIntyre, C. C. Analyzing the tradeoff between electrical complexity and accuracy in patient-specific computational models of deep brain stimulation. *Journal of neural engineering* **13**, 036023 (2016).

[213] Du, X. *et al.* Local gabaergic signaling within sensory ganglia controls peripheral nociceptive transmission. *The Journal of clinical investigation* **127**, 1741–1756 (2017).

[214] Kent, A. R., Min, X., Hogan, Q. H. & Kramer, J. M. Mechanisms of dorsal root ganglion stimulation in pain suppression: a computational modeling analysis. *Neuromodulation: Technology at the Neural Interface* **21**, 234–246 (2018).

[215] Hines, M. L., Morse, T., Migliore, M., Carnevale, N. T. & Shepherd, G. M. Modeldb: a database to support computational neuroscience. *Journal of computational neuroscience* **17**, 7–11 (2004).

[216] Arlow, R., Foutz, T. & McIntyre, C. Theoretical principles underlying optical stimulation of myelinated axons expressing channelrhodopsin-2. *Neuroscience* **248**, 541–551 (2013).

[217] Sharp, D. J., Scott, G. & Leech, R. Network dysfunction after traumatic brain injury. *Nature Reviews Neurology* **10**, 156 (2014).

[218] Coleman, M. Axon degeneration mechanisms: commonality amid diversity. *Nature reviews. Neuroscience* **6**, 889–898 (2005).

[219] Magdesian, M. H. *et al.* Atomic force microscopy reveals important differences in axonal resistance to injury. *Biophysical Journal* **103**, 405–414 (2012).

[220] Tsai, J., Grutzendler, J., Duff, K. & Gan, W.-B. Fibrillar amyloid deposition leads to local synaptic abnormalities and breakage of neuronal branches. *Nature neuroscience* **7**, 1181–1183 (2004).

[221] Krstic, D. & Knuesel, I. Deciphering the mechanism underlying late-onset alzheimer disease. *Nature Reviews Neurology* **9**, 25 (2013).

[222] Galvin, J. E., Uryu, K., Lee, V. M.-Y. & Trojanowski, J. Q. Axon pathology in parkinson's disease and lewy body dementia hippocampus contains α-, β-, and γ-synuclein. *Proceedings of the National Academy of Sciences* **96**, 13450–13455 (1999).

[223] Maxwell, W. L., Povlishock, J. T. & Graham, D. L. A mechanistic analysis of nondisruptive axonal injury: a review. *Journal of neurotrauma* **14**, 419–440 (1997).

[224] Nikić, I. *et al.* A reversible form of axon damage in experimental autoimmune encephalomyelitis and multiple sclerosis. *Nature medicine* **17**, 495–499 (2011).

[225] Trapp, B. D. *et al.* Axonal Transection in the Lesions of Multiple Sclerosis. *New England Journal of Medicine* **338**, 278–285 (1998). URL http://www.nejm.org/doi/abs/10.1056/NEJM199801293380502.

[226] Maia, P. D. & Kutz, J. N. Identifying critical regions for spike propagation in axon segments. *Journal of Computational Neuroscience* **36**, 141–155 (2014).

[227] Maia, P. D. & Kutz, J. N. Compromised axonal functionality after neurodegeneration, concussion and/or traumatic brain injury (2014).

[228] Baschong, W., Suetterlin, R. & Laeng, R. H. Control of autofluorescence of archival formaldehyde-fixed, paraffin-embedded tissue in confocal laser scanning microscopy (clsm). *Journal of Histochemistry & Cytochemistry* **49**, 1565–1571 (2001).

[229] Romijn, H. J. *et al.* Double immunolabeling of neuropeptides in the human hypothalamus as analyzed by confocal laser scanning fluorescence microscopy. *Journal of Histochemistry & Cytochemistry* **47**, 229–235 (1999).

[230] Schnell, S. A., Staines, W. A. & Wessendorf, M. W. Reduction of lipofuscin-like autofluorescence in fluorescently labeled tissue. *Journal of Histochemistry & Cytochemistry* **47**, 719–730 (1999).

[231] Howell, O. W. *et al.* Activated microglia mediate axoglial disruption that contributes to axonal injury in multiple sclerosis. *Journal of Neuropathology & Experimental Neurology* **69**, 1017–1033 (2010).

[232] Schindelin, J. *et al.* Fiji: an open-source platform for biological-image analysis. *Nature methods* **9**, 676–682 (2012).

[233] Schneider, C. A., Rasband, W. S. & Eliceiri, K. W. Nih image to imagej: 25 years of image analysis. *Nature methods* **9**, 671–675 (2012).

[234] MATLAB. *version 9.8.0.1323502 (R2020a)* (The MathWorks Inc., Natick, Massachusetts, 2020).

[235] Haahr, M. RANDOM.ORG: true random number service (1998–2020). URL https://www.random.org.

[236] Muzio, M. R. & Cascella, M. Histology, axon (2020).

[237] Bernabeu, M. O. *et al.* Computer simulations reveal complex distribution of haemodynamic forces in a mouse retina model of angiogenesis. *Journal of the Royal Society Interface* **11**, 20140543 (2014).

[238] Bernabeu, M. O., Lu, Y., Abu-Qamar, O., Aiello, L. P. & Sun, J. K. Estimation of diabetic retinal microaneurysm perfusion parameters based on computational fluid dynamics modeling of adaptive optics scanning laser ophthalmoscopy. *Frontiers in physiology* **9**, 989 (2018).

[239] Choi, H. I. & Han, C. Y. The medial axis transform. *The handbook of computer aided geometric design. Amsterdam: North-Holland* 451–71 (2002).

[240] Gonzalez, R. & Woods, R. Digital image processing: Pearson prentice hall. *Upper Saddle River, NJ* **1** (2008).

[241] Daneshi Kohan, E., Lashkari, B. S. & Sparrey, C. J. The effects of paranodal myelin damage on action potential depend on axonal structure. *Medical & Biological Engineering & Computing* **56**, 395–411 (2018). URL https://doi.org/10.1007/s11517-017-1691-1.

[242] Daneshi, E. & Sparrey, C. Quantifying the effect of a sectioning method for increasing geometrical resolution on computational cost for axons modeled in neuron. In *Proceedings of 22nd International Conference on Computational Neuroscience, Neuroinformatics and Neurocomputing*, 513–527 (New York, USA, 2020).

[243] Virtanen, P. *et al.* SciPy 1.0: Fundamental Algorithms for Scientific Computing in Python. *Nature Methods* **17**, 261–272 (2020).

[244] Pérez, F. & Granger, B. E. IPython: a system for interactive scientific computing. *Computing in Science and Engineering* **9**, 21–29 (2007). URL https://ipython.org.

[245] d'Agostino, R. B. An omnibus test of normality for moderate and large size samples. *Biometrika* **58**, 341–348 (1971).

[246] D'AGOSTINO, R. & Pearson, E. S. Tests for departure from normality. empirical results for the distributions of b 2 and $\sqrt{(}b)$. *Biometrika* **60**, 613–622 (1973).

[247] Conover, W. J. & Iman, R. L. On multiple-comparisons procedures. *Los Alamos Sci. Lab. Tech. Rep. LA-7677-MS* 1–14 (1979).

[248] Lee, H.-H. *et al.* Along-axon diameter variation and axonal orientation dispersion revealed with 3d electron microscopy: implications for quantifying brain white matter microstructure with histology and diffusion mri. *Brain Structure and Function* **224**, 1469–1488 (2019).

[249] Totoiu, M. O. & Keirstead, H. S. Spinal cord injury is accompanied by chronic progressive demyelination. *Journal of Comparative Neurology* **486**, 373–383 (2005).

[250] Beirowski, B., Nógrádi, A., Babetto, E., Garcia-Alias, G. & Coleman, M. P. Mechanisms of axonal spheroid formation in central nervous system wallerian degeneration. *Journal of Neuropathology & Experimental Neurology* **69**, 455–472 (2010).

[251] Edgar, J. M. *et al.* Early ultrastructural defects of axons and axon–glia junctions in mice lacking expression of cnp1. *Glia* **57**, 1815–1824 (2009).

[252] Marion, C. M., Radomski, K. L., Cramer, N. P., Galdzicki, Z. & Armstrong, R. C. Experimental traumatic brain injury identifies distinct early and late phase axonal conduction deficits of white matter pathophysiology, and reveals intervening recovery. *Journal of Neuroscience* **38**, 8723–8736 (2018).

[253] Howell, O. W. *et al.* Activated Microglia Mediate Axoglial Disruption That Contributes to Axonal Injury in Multiple Sclerosis. *Journal of Neuropathology and Experimental Neurology* **69**, 1017–1033 (2010). URL http://content.wkhealth.com/linkback/openurl?sid=WKPTLP:landingpage{&}an=00005072-201010000-00004.

[254] Nicholls, J. G., Martin, A. R., Wallace, B. G. & Fuchs, P. A. *From neuron to brain*, vol. 271 (Sinauer Associates Sunderland, MA, 2001).

[255] Costa, A. R., Pinto-Costa, R., Sousa, S. C. & Sousa, M. M. The regulation of axon diameter: from axonal circumferential contractility to activity-dependent axon swelling. *Frontiers in molecular neuroscience* **11**, 319 (2018).

[256] Wang, M., Yan, B., Hu, J. & Li, P. Simulation of large neuronal networks with biophysically accurate models on graphics processors. In *The 2011 International Joint Conference on Neural Networks*, 3184–3193 (IEEE, 2011).

[257] Hoang, R. V., Tanna, D., Jayet Bray, L. C., Dascalu, S. M. & Harris Jr, F. C. A novel cpu/gpu simulation environment for large-scale biologically realistic neural modeling. *Frontiers in neuroinformatics* **7**, 19 (2013).

[258] Vacher, H., Mohapatra, D. P. & Trimmer, J. S. Localization and targeting of voltage-dependent ion channels in mammalian central neurons. *Physiological reviews* **88**, 1407–1447 (2008).

[259] Waxman, S. G., Black, J. A., Ransom, B. R. & Stys, P. K. Protection of the axonal cytoskeleton in anoxic optic nerve by decreased extracellular calcium. *Brain research* **614**, 137–145 (1993).

[260] Dymowski, A. R., Owens, J. A., Ponsford, J. L. & Willmott, C. Speed of processing and strategic control of attention after traumatic brain injury. *Journal of clinical and experimental neuropsychology* **37**, 1024–1035 (2015).

[261] Peters, A. & Sethares, C. Aging and the myelinated fibers in prefrontal cortex and corpus callosum of the monkey. *Journal of Comparative Neurology* **442**, 277–291 (2002).

[262] Kohama, S. G., Rosene, D. L. & Sherman, L. S. Age-related changes in human and non-human primate white matter: from myelination disturbances to cognitive decline. *Age* **34**, 1093–1110 (2012).

[263] Stojic, A., Bojcevski, J., Williams, S. K., Diem, R. & Fairless, R. Early nodal and paranodal disruption in autoimmune optic neuritis. *Journal of Neuropathology & Experimental Neurology* **77**, 361–373 (2018).

[264] Howell, O. *et al.* Disruption of neurofascin localization reveals early changes preceding demyelination and remyelination in multiple sclerosis. *Brain* **129**, 3173–3185 (2006).

[265] Fu, Y. *et al.* Paranodal myelin retraction in relapsing experimental autoimmune encephalomyelitis visualized by coherent anti-stokes raman scattering microscopy. *Journal of biomedical optics* **16**, 106006 (2011).

[266] Ortiz, F. C. *et al.* Neuronal activity in vivo enhances functional myelin repair. *JCI insight* **4** (2019).

[267] Teo, W. Mechanisms of central axon and myelin injury using advanced morphological and biochemical characterization (2015).

[268] Edgar, J. M. *et al.* Oligodendroglial modulation of fast axonal transport in a mouse model of hereditary spastic paraplegia. *The Journal of cell biology* **166**, 121–131 (2004).

[269] Xiong, Y., Mahmood, A. & Chopp, M. Animal models of traumatic brain injury. *Nature Reviews Neuroscience* **14**, 128–142 (2013).

[270] POVLISHOCK, J. T., Hayes, R. L., MICHEL, M. E. & McINTOSH, T. K. Workshop on animal models of traumatic brain injury. *Journal of neurotrauma* **11**, 723–732 (1994).

[271] Reid, W. M. *et al.* Strain-related differences after experimental traumatic brain injury in rats. *Journal of neurotrauma* **27**, 1243–1253 (2010).

[272] Tan, A. A., Quigley, A., Smith, D. C. & Hoane, M. R. Strain differences in response to traumatic brain injury in long-evans compared to sprague-dawley rats. *Journal of neurotrauma* **26**, 539–548 (2009).

[273] FOX, G. B., LeVASSEUR, R. A. & FADEN, A. I. Behavioral responses of c57bl/6, fvb/n, and 129/svems mouse strains to traumatic brain injury: implications for gene targeting approaches to neurotrauma. *Journal of neurotrauma* **16**, 377–389 (1999).

[274] Leenen, L., Meek, J. & Nieuwenhuys, R. Unmyelinated fibers in the pyramidal tract of the rat: a new view. *Brain research* **246**, 297–301 (1982).

[275] Biedenbach, M., DeVito, J. & Brown, A. Pyramidal tract of the cat: axon size and morphology. *Experimental brain research* **61**, 303–310 (1986).

[276] Saliani, A. *et al.* Axon and myelin morphology in animal and human spinal cord. *Frontiers in neuroanatomy* **11**, 129 (2017).

[277] Leenen, L., Meek, J., Posthuma, P. & Nieuwenhuys, R. A detailed morphometrical analysis of the pyramidal tract of the rat. *Brain research* **359**, 65–80 (1985).

[278] Brösamle, C. & Schwab, M. E. Ipsilateral, ventral corticospinal tract of the adult rat: ultrastructure, myelination and synaptic connections. *Journal of neurocytology* **29**, 499–507 (2000).

[279] Harding, G. & Towe, A. Fiber analysis of the pyramidal tract of the laboratory rat. *Experimental neurology* **87**, 503–518 (1985).

[280] Van Crevel, H. & Verhaart, W. The rate of secondary degeneration in the central nervous system: I. the pyramidal tract of the cat. *Journal of Anatomy* **97**, 429 (1963).

[281] Firmin, L. *et al.* Axon diameters and conduction velocities in the macaque pyramidal tract. *Journal of neurophysiology* **112**, 1229–1240 (2014).

[282] Terao, S.-i., Sobue, G., Hashizume, Y., Shimada, N. & Mitsuma, T. Age-related changes of the myelinated fibers in the human corticospinal tract: a quantitative analysis. *Acta neuropathologica* **88**, 137–142 (1994).

[283] Verhaart, W. On thick and thin fibers in the pyramidal tract. *Acta Psychiatrica Scandinavica* **22**, 271–281 (1947).

[284] Nout, Y. S. *et al.* Animal models of neurologic disorders: a nonhuman primate model of spinal cord injury. *Neurotherapeutics* **9**, 380–392 (2012).

[285] Lee, D.-H. & Lee, J. K. Animal models of axon regeneration after spinal cord injury. *Neuroscience bulletin* **29**, 436–444 (2013).

[286] Silva, N. A., Sousa, N., Reis, R. L. & Salgado, A. J. From basics to clinical: a comprehensive review on spinal cord injury. *Progress in neurobiology* **114**, 25–57 (2014).

[287] Basic physician facts in Canada. URL https://www.cma.ca/En/Pages/basic-physician-facts.aspx.

[288] Courtine, G. *et al.* Can experiments in nonhuman primates expedite the translation of treatments for spinal cord injury in humans? *Nature medicine* **13**, 561–566 (2007).

[289] Kim, K.-T. *et al.* Differences in morphometric measures of the uninjured porcine spinal cord and dural sac predict histological and behavioral outcomes after traumatic spinal cord injury. *Journal of neurotrauma* **36**, 3005–3017 (2019).

[290] Liewald, D., Miller, R., Logothetis, N., Wagner, H.-J. & Schüz, A. Distribution of axon diameters in cortical white matter: an electron-microscopic study on three human brains and a macaque. *Biological cybernetics* **108**, 541–557 (2014).

[291] ROOF, R. L. & HALL, E. D. Estrogen-related gender difference in survival rate and cortical blood flow after impact-acceleration head injury in rats. *Journal of neurotrauma* **17**, 1155–1169 (2000).

[292] Berry, C. *et al.* The effect of gender on patients with moderate to severe head injuries. *Journal of Trauma and Acute Care Surgery* **67**, 950–953 (2009).

[293] Abrahams, S., Mc Fie, S., Patricios, J., Posthumus, M. & September, A. V. Risk factors for sports concussion: an evidence-based systematic review. *British journal of sports medicine* **48**, 91–97 (2014).

[294] Covassin, T., Swanik, C. B. & Sachs, M. L. Sex differences and the incidence of concussions among collegiate athletes. *Journal of athletic training* **38**, 238 (2003).

[295] Marar, M., McIlvain, N. M., Fields, S. K. & Comstock, R. D. Epidemiology of concussions among united states high school athletes in 20 sports. *The American journal of sports medicine* **40**, 747–755 (2012).

[296] Bazarian, J. J. & Atabaki, S. Predicting postconcussion syndrome after minor traumatic brain injury. *Academic Emergency Medicine* **8**, 788–795 (2001).

[297] Broshek, D. K. *et al.* Sex differences in outcome following sports-related concussion. *Journal of neurosurgery* **102**, 856–863 (2005).

[298] Dollé, J.-P. *et al.* Newfound sex differences in axonal structure underlie differential outcomes from in vitro traumatic axonal injury. *Experimental neurology* **300**, 121–134 (2018).

[299] Stein, D. Progesterone in the treatment of acute traumatic brain injury: a clinical perspective and update. *Neuroscience* **191**, 101–106 (2011).

[300] Farace, E. & Alves, W. M. Do women fare worse: a metaanalysis of gender differences in traumatic brain injury outcome. *Journal of neurosurgery* **93**, 539–545 (2000).

[301] Ma, J., Huang, S., Qin, S., You, C. & Zeng, Y. Progesterone for acute traumatic brain injury. *Cochrane Database of Systematic Reviews* (2016).

[302] Alexander, D. C. *et al.* Orientationally invariant indices of axon diameter and density from diffusion mri. *Neuroimage* **52**, 1374–1389 (2010).

[303] Gur, R. C. *et al.* Sex differences in brain gray and white matter in healthy young adults: correlations with cognitive performance. *Journal of Neuroscience* **19**, 4065–4072 (1999).

[304] Tomar, G. S. *et al.* New biomarkers in brain trauma. *Clinica Chimica Acta* **487**, 325–329 (2018).

[305] Mondello, S. *et al.* αii-spectrin breakdown products (sbdps): diagnosis and outcome in severe traumatic brain injury patients. *Journal of neurotrauma* **27**, 1203–1213 (2010).

[306] Papa, L. *et al.* Biomarkers improve clinical outcome predictors of mortality following non-penetrating severe traumatic brain injury. *Neurocritical care* **22**, 52–64 (2015).

[307] Gardner, R. C. *et al.* Age-related differences in diagnostic accuracy of plasma glial fibrillary acidic protein and tau for identifying acute intracranial trauma on computed tomography: a track-tbi study. *Journal of neurotrauma* **35**, 2341–2350 (2018).

[308] Yang, Z. *et al.* Serum-based phospho-neurofilament-heavy protein as theranostic biomarker in three models of traumatic brain injury: an operation brain trauma therapy study. *Journal of neurotrauma* **36**, 348–359 (2019).

[309] Martínez-Morillo, E. *et al.* Neurofilament medium polypeptide (nfm) protein concentration is increased in csf and serum samples from patients with brain injury. *Clinical Chemistry and Laboratory Medicine (CCLM)* **53**, 1575–1584 (2015).

[310] Halford, J. *et al.* New astroglial injury-defined biomarkers for neurotrauma assessment. *Journal of Cerebral Blood Flow & Metabolism* **37**, 3278–3299 (2017).

[311] Spira, M. E. & Hai, A. Multi-electrode array technologies for neuroscience and cardiology. *Nature nanotechnology* **8**, 83 (2013).

[312] Normann, R. A., Warren, D. J., Ammermuller, J., Fernandez, E. & Guillory, S. High-resolution spatio-temporal mapping of visual pathways using multi-electrode arrays. *Vision research* **41**, 1261–1275 (2001).

[313] Miller, S. J. *et al.* Molecularly defined cortical astroglia subpopulation modulates neurons via secretion of norrin. *Nature neuroscience* **22**, 741–752 (2019).

[314] Borton, D. *et al.* Corticospinal neuroprostheses to restore locomotion after spinal cord injury. *Neuroscience research* **78**, 21–29 (2014).

[315] Höke, A. Mechanisms of disease: what factors limit the success of peripheral nerve regeneration in humans? *Nature clinical practice Neurology* **2**, 448–454 (2006).

[316] Margulies, S. & Hicks, R. Combination therapies for traumatic brain injury: prospective considerations. *Journal of neurotrauma* **26**, 925–939 (2009).

[317] Dekmak, A. *et al.* Stem cells and combination therapy for the treatment of traumatic brain injury. *Behavioural brain research* **340**, 49–62 (2018).

[318] Zhang, Y. *et al.* Rapid single-step induction of functional neurons from human pluripotent stem cells. *Neuron* **78**, 785–798 (2013).

[319] Tang-Schomer, M. D., Patel, A. R., Baas, P. W. & Smith, D. H. Mechanical breaking of microtubules in axons during dynamic stretch injury underlies delayed elasticity, microtubule disassembly, and axon degeneration. *FASEB journal : official publication of the Federation of American Societies for Experimental Biology* **24**, 1401–1410 (2010).

[320] Courson, J. A. *et al.* Serial block-face scanning electron microscopy reveals neuronal-epithelial cell fusion in the mouse cornea. *Plos one* **14**, e0224434 (2019).

[321] Abbott, J. *et al.* Cmos nanoelectrode array for all-electrical intracellular electrophysiological imaging. *Nature nanotechnology* **12**, 460–466 (2017).

[322] Berdondini, L. *et al.* Active pixel sensor array for high spatio-temporal resolution electrophysiological recordings from single cell to large scale neuronal networks. *Lab on a Chip* **9**, 2644–2651 (2009).

[323] Wang, B. *et al.* Firing frequency maxima of fast-spiking neurons in human, monkey, and mouse neocortex. *Frontiers in cellular neuroscience* **10**, 239 (2016).

[324] O'Donnell, L. J. & Westin, C.-F. An introduction to diffusion tensor image analysis. *Neurosurgery Clinics* **22**, 185–196 (2011).